TÉCNICO LISBOA

A conceptual design and evaluation framework for ADCS for CubeSats

Beatriz Camelo Ribeiro Ferreira Alves

Thesis to obtain the Master of Science Degree in

Aerospace Engineering

Supervisors: Prof. Afzal Suleman
Prof. Paulo Jorge Coelho Ramalho Oliveira

Examination Committee

Chairperson: Prof. Filipe Szolnoky Ramos Pinto Cunha
Supervisor: Prof. Afzal Suleman
Member of the Committee: Aymeric Kron

November 2021

To my mom, dad and sister...

Acknowledgments

I would like to start by thanking my supervisors, Professor Suleman, for the wonderful opportunity to work on my thesis in the Centre for Aerospace Research of University of Victoria and for all his support during the entire work period and Professor Paulo Oliveira for his insightful thoughts and contributions.

To all my friends Diogo, Mariana Tavares, Mariana Santos, Hugo Costa, Hugo Faustino, Pedro and Daniele who I had the pleasure to navigate this adventure with and to the amazing ORCASat team who I shared everyday with.

I would like to thank my family and friends back home, who I missed everyday and all the professors who taught me so much during the past five years.

Lastly, I am grateful for all the wonderful people I had the pleasure to meet in Canada and for all you have taught me. Thank you for making these memories even more special.

Resumo

Durante o desenvolvimento de CubeSats, o sistema de determinação e controlo de atitude (ADCS) tem tipicamente um custo elevado, sendo normalmente baseado em soluções comercialmente disponíveis (COTS). Uma ferramenta de design capaz de simular diferentes arquiteturas de ADCS comuns permite aos designers testarem diferentes soluções possíveis para o ADCS, resultando em decisões mais informadas. Além disso, tal ferramenta elimina a necessidade de software comercial criado especificamente para cada solução particular.

Com este objetivo, uma ferramenta de simulação foi desenvolvida em Matlab/Simulink. A ferramenta modela um ambiente espacial realista e as características físicas do CubeSat, permite testar uma ampla gama de métodos ADCS passivos e ativos e inclui uma gama de algoritmos para estimativa e controlo de atitude.

Três opções diferentes de estabilização passiva estão disponíveis atualmente: barras de gradiente de gravidade, painéis de estabilização aerodinâmica, ímans permanentes e hastes de histerese. Além disso, o utilizador pode simular sensores solares, magnetómetros, giroscópios, sensores terrestres e estelares e atuadores como magnetorquers, e diversas configurações de volantes de reação e de momento e giroscópios de controle de momento. O utilizador também pode escolher entre vários algoritmos convencionais de determinação e controlo de atitude.

A ferramenta foi usada para avaliar o ADCS do ORCASAT, um projeto da Universidade de Victoria CubeSat financiado pela Agência Espacial Canadiana. Arquiteturas ADCS alternativas foram testadas e comparadas em termos de massa, volume, potência, erro de apontamento e estimativa.

Palavras-chave: ADCS, CubeSat, estimação de atitude, controlo de atitude

Abstract

The Attitude Determination and Control System (ADCS) is one of the most expensive CubeSat sub-systems and it is usually based on commercial of the shelf options. A design framework and simulation tool has been developed to evaluate the performance of several common ADCS architectures for Cube-Sats thus allowing designers and developers to select the most suitable solution in terms of architecture and components. The proposed design and simulation tool also eliminates the need for expensive and commercially protected software specifically created for each individual ADCS architecture option. The Matlab/Simulink design and simulation tool models a realistic orbital space environment and the Cube-Sat physical constraints in terms of volume and weight. It also enables the evaluation of a wide range of both passive and active ADCS systems and associated computational algorithms for attitude estimation and control.

Three different passive attitude stabilization options are currently available: deployable gravity gradient booms and aerodynamic stabilizing panels, permanent magnets and hysteresis rods. Moreover, the user can experiment with both fine and coarse sun sensors, magnetometers, gyros, Earth sensors and star trackers, and actuators such as magnetorquers, reaction and momentum wheels and single gimbal control momentum gyros. Several most common cluster architectures of momentum devices are available to the user. The user can also choose between conventional static determination, recursive estimation and control algorithms.

The tool was used to evaluate the ADCS for the ORCASAT, a University of Victoria CubeSat project funded by the Canadian Space Agency. Currently, ORCASAT has a commercial off-the-shelf ADCS developed by CubeSpace. Alternative ADCS architectures have been tested and compared in terms of weight, volume, power required, pointing and estimation error.

Keywords: CubeSat, ADCS, attitude determination, attitude control

x

Contents

List of Tables

List of Figures

Nomenclature

Greek symbols

α Angle of attack.

γ Aperture angle.

$\boldsymbol{\tau}$ Torque.

$\boldsymbol{\omega}$ Angular velocity.

ϕ, θ, ψ Roll, Pitch and Yaw angles.

β Angle between the body axes and the Earth horizon.

λ Eigenvalue.

δ Gimbal Angle.

Roman symbols

$\mathbf{r}$ Orbital radius vector.

$\mathbf{q}$ Quaternion.

G Universal Gravitaationl Constant.

m Mass.

$\mathbf{J}$ Inertia Tensor.

$\mathbf{h}$ Angular Momentum vector.

$\mathbf{f}$ Force.

$\mathbf{v}$ Velocity vector.

$\mathbf{c^P}$ Center of pressure.

$\mathbf{m}$ Magnetic dipole.

p Solar radiation pressure.

$\mathbf{I}$ Identity matrix.

$\mathbf{d_i}$ Distance between the center of mass of component i and the center of mass of the spacecraft.

V Volume.

μ_0 Magnetic permeability of the vacuum.

$\mathbf{H}$ Magnetic field strength.

l Length.

w Width.

R_E Equatorial radius of the Earth.

h Altitude.

P Power.

K_i Torque constant.

K_b Back emf constant.

L Inductance.

R Resistance.

i Current.

B_m Viscous friction coefficient.

c Coulomb friction coefficient.

Subscripts

O   In the orbit fram.

B   In the body frame.

I   In the inertial frame.

Superscripts

T   Transpose.

-1   Inverse.

*   Conjugate.

List of Acronyms

BLDC Brushless Direct Current

CCD Charge-Coupled Device

CM Center of Mass

CMG Control Moment Gyro

CMOS Complementary Metal-Oxide Semiconductor

COTS Commercial Off-the-Shelf

DC Direct Current

DCM Direction Cosine Matrix

ECI Earth Centered Inertial

EKF Extended Kalman Filter

GPS Global Positioning System

HIL Hardware-In-the-Loop

LQR Linear Quadratic Regulator

LVLH Local-Vertical/Local-Horizon Frame

OBC On Board Computer

ORCASat Optical and Radio CAlibration Satellite

PMAC Passive Magnetic Attitude Control

SGCMG Single Gimbal Control Momentum Gyro

SRP Solar Radiation Pressure

UVIC University of Victoria

Chapter 1

Introduction

1.1 The CubeSat Project

A CubeSat is a small square-shaped satellite initially introduced in 1999 [1]. The main goal of the CubeSat project was to provide a standard design for pico and nanosatellites so as to reduce both launch and construction cost as well as development time and increase accessibility to space [2]. Originally defined as a $10cm$x$10cm$x$10cm$ cube with a mass of up to $1.33kg$ [1], also known as a single unit (1U), modern CubeSats may vary in size by assemblage of multiple units. Some popular configurations are 0.5U, 1U, 1.5U, 2U, 3U and 6U [3].

These characteristics make CubeSats an appealing option, not only to private companies, but also to universities and high schools. At the time of writing, more than 1500 CubeSats have been launched and the number of CubeSats launched per year is expected to increase in the next four years [4].
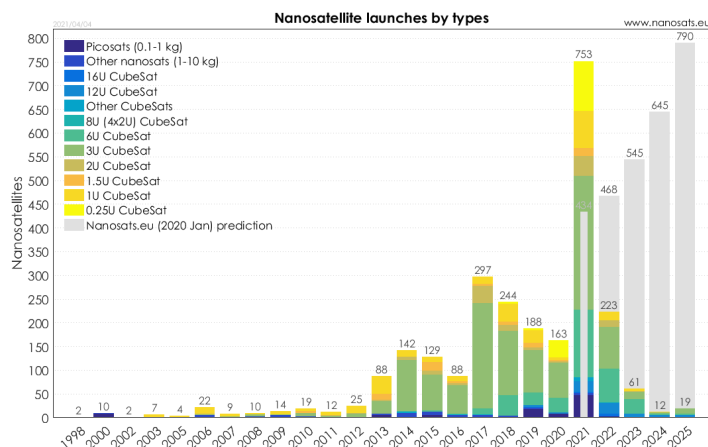
Figure 1.1: Number of nanosatellites launched by year per institution type and forecast until 2025 [4]

1.2 The ORCASat

The Optical and Radio CAlibration Satellite (ORCASat) is a CubeSat developed at University of Victoria (UVIC) as part of the Canadian Space Agency's Canadian CubeSat Project. This satellite results of the collaboration between UVIC and several other organizations, namely, University of British Columbia (UBC) and University of Lisbon [5].

The goal of the ORCASat mission is to serve as a reference light source to calibrate astronomical observatories and its mission requires nadir pointing with a maximum error of 10° and a maximum estimation error of 2°. The spacecraft is equipped with a Commercial Off-the-Shelf (COTS) attitude and determination subsystem by CubeSpace which consumed a significant portion of the satellite's budget.

1.3 Motivation

During the design of the attitude determination and control system (ADCS) the ORCASAT team struggled with the validation of the chosen ADCS solution. With the increasing innovation in the ADCS leads to the necessity of a tool capable of realistically simulate the behavior of the satellite in orbit when equipped with different subsystem solutions. Even though simulations are sometimes provided by manufactures or, like in the ORCASat case, created by the CubeSat teams, these are frequently designed so as to validate only one particular architecture and, in case of commercial simulators, may represent a significant added cost.

To the extent of the knowledge of the author, at the time of writing, there is a lack of publicly available tools for simulation of CubeSat ADCS, with only two tools available: the Smart Nanosatellite Attitude Propagator (SNAP) and Aerospace Blockset CubeSat Simulation library. Despite being a simple efficient tool, the SNAP, only allows the user to simulate magnetic passive attitude stabilization and control. The Aerospace Blockset CubeSat Simulation library, whose blocks where partially used in this work, provides realistic environment models as well as useful attitude transformation blocks, but does not provide detailed "non-ideal" sensor and actuator models. Moreover, these tools do not provide power consumption/availability analysis.

The design of a CubeSat ADCS simulator, able to simulate different realistic ADCS architectures, both passive and active, would enable satellite teams to experiment with different possible solutions before committing to a specific ADCS architecture. More innovative solutions can also be tested with "non-ideal" models without requiring teams big time and monetary investments.

Furthermore, such tool can be also of value in educational settings as it provides a way for students to experiment with different ADCS architectures and visualize their results.

1.4 Literature Review

In an initial phase, a survey was conducted to better access both the commercially available attitude sensor and actuators currently available in the market as well as the commonly employed architectures

and requirements of educational CubeSats. The results of this research concerned 60 educational CubeSats as well as more than 60 commercially available sensors and actuators. More detailed information can be found on appendix A, however, some important results are summarized in this chapter.

The most commonly available COTS sensors are sun sensors and magnetometers with most big companies offering multiple options. These are also some of the lightest and cheapest sensors in the market with options available with mass lower than $5g$ for sun sensors and $10g$ for magnetometers. These are also some of the cheapest sensors available with prices of flight proven sensors starting at a few thousand dollars. Star trackers and horizon sensors (also known as nadir sensors or Earth sensors) are becoming more popular with most main companies offering at least one option of each of these sensors.

When it comes to actuators, both magnetorquers and flywheels (such as reaction and momentum wheels) still dominate the market with most industry providers offering multiple options of each. Control moment gyros are still uncommon with the only solution commercially available being the Honeybee Robotics' Microsat Control Moment Gyroscope by Honeybee Robotics [6], however, this solution is starting to appear more as in-the-house-made solution, still representing a new cutting edge technology for CubeSats.
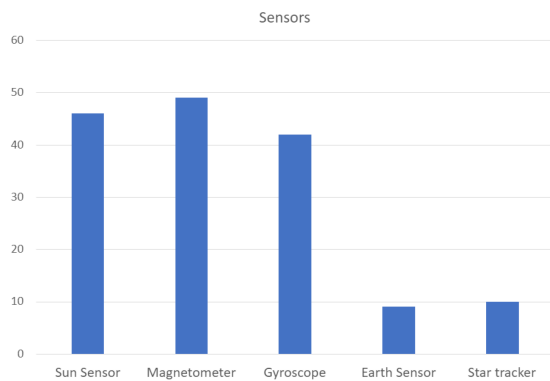
Figure 1.2: Academic Cubesats on board attitude sensors
Figure 1.3: Academic Cubesats on board attitude actuators
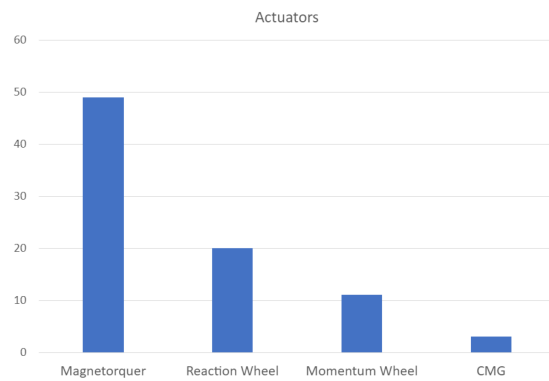
Figure 1.2 shows results from the data base regarding the most common architectures employed by CubeSats. Despite passive attitude solutions still being common, CubeSats are increasingly opting for more complex ADCS systems.
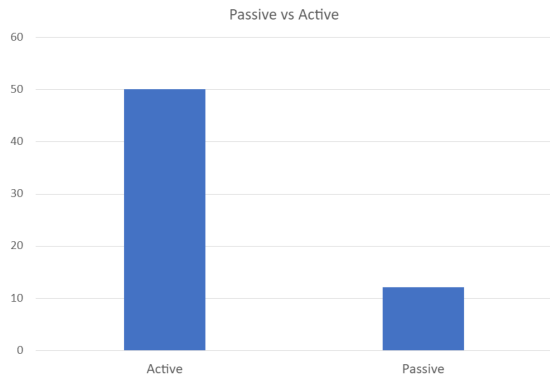
Figure 1.4: Academic Cubesats ADCS passive stabilization methods
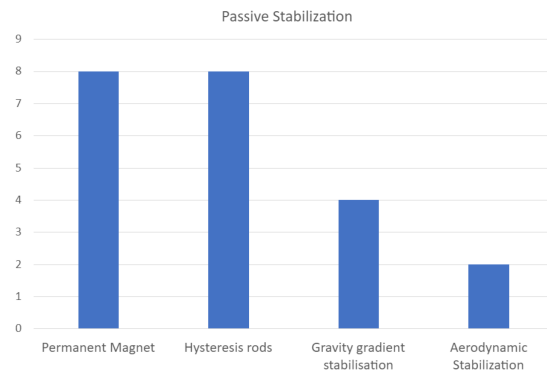
Figure 1.5: Academic Cubesats on board passive ADCS methods

Despite the most common sensors (Figure 1.4) and actuators (Figure 1.5) aligning with the most commonly available options in the market, some CubeSat teams opt for less conventional architectures that push the boundaries of the state of the art. Some missions that stand out for the innovative character of their ADCS solutions are Chasqui-I [7] with a hybrid passive and active magnetic control solution and Swampsat I [8] and II [9] for their development of a CMG that occupies less than 0.5U.

1.5   Objectives

This thesis has two main goals:

- The creation of a tool capable of simulating different Cubesat ADCS architectures;

- The study of the current ORCASat ADCS solution.

In order to achieve the first objective, the simulation tool designed for the ORCASat is going to be used as a base. This work aims to improve and complete the existing tool by the addition of:

- further perturbation models;

- methods of passive attitude stabilization;

- alternative sensors' models;

- multiple momentum exchange devices with diverse configurations;

- alternative commonly used estimation algorithms;

- a control algorithm for momentum exchange devices.

The study of ORCASat's ADCS encompassed the following objectives:

- study the performance of the spacecraft in event of sensor/actuator failure;

- study the performance of possible alternative architectures.

1.6 Thesis Outline

This thesis is divided in the following chapters:

Chapter 2 summarizes the necessary theoretical background regarding the frames of reference and attitude parametrizations used through out this work and introduces the physics behind the spacecrafts' motion, namely, orbital mechanics, concerned with translation of the spacecraft and attitude kinematics and dynamics regarding its rotation. The main perturbation forces and torques acting on the spacecraft are also presented in this chapter.

Chapter 3 presents the different commonly available hardware solutions for CubeSats. Advantages, disadvantages and the basic working principle of frequently used sensors, actuators and passive devices are introduced.

Chapter 4 presents the simulation tool developed in this thesis. Firstly, a general overview of the tool is presented, followed by a detailed explanation of each of the subsystems that constitute it.

Chapter 5 presents the simulations conducted to analyze ORCASat's ADCS solution and consequent results. The impact of initial conditions and the failure of a sensor or actuator on the performance of the ADCS is studied. Finally, alternative architectures are purposed and compared.

Chapter 6 summarizes the thesis conclusions and suggests further development of this work.

Chapter 2

Theoretical Background

This chapter introduces some basic concepts related to attitude determination and control. In 2.1, the different reference frames utilized in this work are presented, whereas, 2.2 presents different methods of attitude parameterization.

2.1   Reference Frames

Reference frames consist of coordinate systems, generally specified by the orientation of a set of axes and the location of its origin. The attitude of a body can be described as the orientation of a reference frame with respect to another [10]. The main reference frames used in this work will be described in this section.

2.1.1   Earth Centered Inertial Frame

An inertial reference frame is a reference frame that is not subjected to any acceleration, that is, a frame with constant (or null) velocity and without rotation. In inertial reference frames, the Newton's laws of motion are valid [10]. Despite what the name may suggest, due to the motion of the Earth around the sun, the Earth Centered Inertial (ECI) reference frame can not be considered a genuine inertial frame. Nevertheless, for attitude purposes the acceleration of the ECI frame can be neglected, and this will be treated as approximately inertial.

The ECI reference frame is constituted by the set of axes $\{\hat{\mathbf{i}}_1, \hat{\mathbf{i}}_2, \hat{\mathbf{i}}_3\}$, with $\hat{\mathbf{i}}_3$, pointing towards the Earth's geographic North pole, $\hat{\mathbf{i}}_1$, directed towards the vernal equinox (the intersection of the ecliptic and equatorial plane in the direction of the Sun's position relative to the Earth on spring equinox). The last axis $\hat{\mathbf{i}}_2$ completes the right-hand triad. Since the direction of both the North Pole and the *vernal equinox* are not static in time, this work defines these axes as their mean orientation at the current standard epoch, the J2000. The ECI frame's origin coincides with the Earth's Center of Mass (CM).

6

2.1.2 Local-Vertical/Local-Horizon Frame

Also known as the orbital frame, the Local-Vertical/Local-Horizon Frame (LVLH) frame is of special importance for nadir pointing missions. This is a non-inertial reference frame, centered on the satellite's center of mass and defined by the orthogonal triad $\{\hat{o}_1, \hat{o}_2, \hat{o}_3\}$. The axis $\hat{o}_3$ is aligned with the nadir direction (directed towards the center of mass of the Earth), while the axis $\hat{o}_2$ is oriented along the orbit normal in the direction opposite to orbital angular momentum vector. $\hat{o}_1$ completes the right hand triad. By definition, the LVLH axes can be written in the ECI frame as:

$$\hat{o}_{3I} = -\frac{\mathbf{r_I}}{r_I} \tag{2.1}$$

$$\hat{o}_{2I} = -\frac{\mathbf{r_I} \times \mathbf{v_I}}{\|\mathbf{r_I} \times \mathbf{v_I}\|} \tag{2.2}$$

$$\hat{o}_{1I} = \hat{o}_{2I} \times \hat{o}_{3I} \tag{2.3}$$

where $\mathbf{r_I}$ and $\mathbf{v_I}$ represent, respectively, the position and the velocity of the spacecraft in the ECI frame.

2.1.3 Body Frame

The body frame is defined by a set of cartesian axes and a origin set on a specified point of the spacecraft. The choice of origin and axes changes from mission to mission, however, the origin is typically chosen to coincide with the center of mass of the spacecraft and its axis $\{\hat{b}_1, \hat{b}_2, \hat{b}_3\}$ are normally chosen so as to align with the principal axis of inertia of the body [10]. For the ORCASat, the body frame was chosen so that, in nominal mode, it's payload is pointing towards nadir, that is, that for null pointing error the body frame is aligned with the orbit frame.

2.2 Attitude Parameters

The attitude of a body can be represented by several different parameters. In this section, the main representation methods utilized in this work are presented, alongside with its advantages and disadvantages.

2.2.1 Direction Cosine Matrix

Given two different reference frames $\mathbf{F} = \{\hat{f}_1, \hat{f}_2, \hat{f}_3\}$ and $\mathbf{G} = \{\hat{g}_1, \hat{g}_2, \hat{g}_3\}$, there is always a rotation matrix $\mathbf{A_{GF}}$, such that:

$$\mathbf{v_g} = \mathbf{A_{GF}} \mathbf{v_f} \tag{2.4}$$

where $\mathbf{v_g}$ and $\mathbf{v_f}$ are representations of the same vector in reference frames $\mathbf{G}$ and $\mathbf{F}$, respectively. The rotation matrix $\mathbf{A_{GF}}$, known as the attitude matrix or Direction Cosine Matrix (DCM), transforms the

coordinate reference frame $\mathbf{F}$ to $\mathbf{G}$ and is defined as:

$$\mathbf{A_{GF}} = \begin{bmatrix} \hat{\mathbf{g}}_1.\hat{\mathbf{f}}_1 & \hat{\mathbf{g}}_1.\hat{\mathbf{f}}_2 & \hat{\mathbf{g}}_1.\hat{\mathbf{f}}_3 \\ \hat{\mathbf{g}}_2.\hat{\mathbf{f}}_1 & \hat{\mathbf{g}}_2.\hat{\mathbf{f}}_2 & \hat{\mathbf{g}}_2.\hat{\mathbf{f}}_3 \\ \hat{\mathbf{g}}_3.\hat{\mathbf{f}}_1 & \hat{\mathbf{g}}_3.\hat{\mathbf{f}}_2 & \hat{\mathbf{g}}_3.\hat{\mathbf{f}}_3 \end{bmatrix} \tag{2.5}$$

The DCM $\mathbf{A_{GF}}$, is a 3×3 orthogonal matrix with positive and unitary determinant, that is

$$\mathbf{A_{GF}}^T = \mathbf{A_{GF}}^{-1} \tag{2.6}$$

$$\det(\mathbf{A_{GF}}) = 1 \tag{2.7}$$

As a consequence, the operation 2.4 preserves the length of vectors and angles, independently of the reference frames. Another important property of the DCM is that, if $n \in \mathbb{N}$ sequential rotations are performed, each one individually represented by the matrices $\mathbf{A_{21}}, \mathbf{A_{32}}, ... \mathbf{A_{n(n-1)}}$, then:

$$\mathbf{A_{n1}} = \mathbf{A_{n(n-1)}}...\mathbf{A_{32}}\mathbf{A_{21}} \tag{2.8}$$

In addition to the stated properties, the DCM matrix uniquely defines the attitude while also avoiding singularities and computationally heavy trigonometric functions. The main disadvantage of this representation is the use of nine parameters to define the rotation. The redundant parameters make this system less effective in terms of required memory.

2.2.2 Euler Angles

An angular displacement can always be described as a sequence of rotations, more specifically, of three principle rotations. Since matrix multiplication is not commutative, the order in which the rotations are performed affects the the final result, so, when describing the rotation in such a way, it is necessary to specify, not only, the rotation angles, but also, the order of rotation.

In this work, it will be considered the 3-2-1 sequence, due to it's common utilization. Several notations are used to designate the Euler angles. This work uses the convention which associates the Euler angles with the spacecraft axis [10]. Therefore, roll (ϕ) will be associated with the axis e_1, pitch (θ) with e_2 and yaw (ψ) with e_3:

$$\mathbf{A_{321}} = A(e_1, \phi)A(e_2, \theta)A(e_3, \psi) = \begin{bmatrix} c\theta c\psi & c\theta s\psi & -s\theta \\ -c\phi s\psi + s\phi s\theta c\psi & c\phi c\psi + s\phi s\theta s\psi & s\phi c\theta \\ s\phi s\psi + c\phi s\theta c\psi & -s\phi c\psi + c\phi s\theta s\psi & c\phi c\theta \end{bmatrix} \tag{2.9}$$

where c and s represent the trigonometric functions cosine and sine, respectivelly.

Despite being of simple physical interpretation and not involving redundant parameters, the Euler angle representation involves computationally costly trigonometric functions and has no simple representation for sequential rotations. Moreover, singularities may arise. A particular case is gimbal lock,

8

which occurs when $\theta = \pm 90^o$. For this reason, the Euler angle representation should only be used in situations when this condition is sure not to be achieved.

2.2.3 Quaternions

Quaternions were first introduced by Hamilton in the nineteenth century and can be used to represent rotations. Quaternions can be represented as a 4×1 matrix constituted by a vectorial part, $\mathbf{q_{1:3}}$, and a scalar part, q_4 [11].

$$\mathbf{q} = \begin{bmatrix} \mathbf{q_{1:3}} \\ q_4 \end{bmatrix} = \begin{bmatrix} q_1 \\ q_2 \\ q_3 \\ q_4 \end{bmatrix} \tag{2.10}$$

For attitude purposes, the unit quaternion is used. That is:

$$\|\mathbf{q}\| = \mathbf{q}^T \mathbf{q} = \sqrt{q_1^2 + q_2^2 + q_3^2 + q_4^2} = 1 \tag{2.11}$$

Quaternion Algebra

Quaternions follow a specific algebra with some properties important for this work. The complex conjugate of a quaternion is defined as:

$$\mathbf{q}^* = \mathbf{q} = \begin{bmatrix} -\mathbf{q_{1:3}} \\ q_4 \end{bmatrix} \tag{2.12}$$

And the inverse can be defined as:

$$\mathbf{q^{-1}} = \mathbf{q} = \frac{\mathbf{q}^*}{q} \tag{2.13}$$

Two quaternion product operations can be defined. Consider two quaternions $\mathbf{q}$ and $\mathbf{p}$, the product between the two can be written as:

$$\mathbf{q} \odot \mathbf{p} = \begin{bmatrix} p_4 \mathbf{q} + q_4 \mathbf{p} + \mathbf{q} \times \mathbf{p} \\ q_4 p_4 - \mathbf{q_{1:3}} \mathbf{p_{1:3}} \end{bmatrix} \tag{2.14}$$

or as:

$$\mathbf{q} \otimes \mathbf{p} = \begin{bmatrix} p_4 \mathbf{q} + q_4 \mathbf{p} - \mathbf{q} \times \mathbf{p} \\ q_4 p_4 - \mathbf{q_{1:3}} \mathbf{p_{1:3}} \end{bmatrix} \tag{2.15}$$

It can easily be seen that both product definitions are associative and distributive but not commutative. In fact, it can be easily shown that:

$$\mathbf{q} \odot \mathbf{p} = \mathbf{p} \otimes \mathbf{q} \tag{2.16}$$

9

Quaternion products can also be expressed in a matrix form:

$$[\mathbf{q}\odot] = \begin{bmatrix} \Xi(\mathbf{q}) & \mathbf{q} \end{bmatrix} = \begin{bmatrix} q_4 I_3 + [\mathbf{q_{1:3}}\times] & \mathbf{q_{1:3}} \\ -\mathbf{q_{1:3}}^T & q_4 \end{bmatrix} \tag{2.17}$$

$$[\mathbf{q}\otimes] = \begin{bmatrix} \Psi(\mathbf{q}) & \mathbf{q} \end{bmatrix} = \begin{bmatrix} q_4 I_3 - [\mathbf{q_{1:3}}\times] & \mathbf{q_{1:3}} \\ -\mathbf{q_{1:3}}^T & q_4 \end{bmatrix} \tag{2.18}$$

where:

$$\Xi(\mathbf{q}) = \begin{bmatrix} q_4 & -q_3 & q_2 \\ q_3 & q_4 & -q_1 \\ -q_2 & q_1 & q_4 \\ -q_1 & -q_2 & -q_3 \end{bmatrix} \tag{2.19}$$

$$\Psi(\mathbf{q}) = \begin{bmatrix} q_4 & q_3 & -q_2 \\ -q_3 & q_4 & q_1 \\ q_2 & -q_1 & q_4 \\ -q_1 & -q_2 & -q_3 \end{bmatrix} \tag{2.20}$$

The product of a quaternion with its conjugate yields:

$$\mathbf{q} \odot \mathbf{q}^* = \mathbf{q}^* \odot \mathbf{q} = \mathbf{q} \otimes \mathbf{q}^* = \mathbf{q}^* \otimes \mathbf{q} = \|\mathbf{q}\|^2 \mathbf{I_q} \tag{2.21}$$

$\mathbf{I_q}$ is the identity quaternion given by:

$$\mathbf{I_q} = \begin{bmatrix} \mathbf{0_{1:3}} \\ 1 \end{bmatrix} \tag{2.22}$$

On the downside, this representation method does not possess an intuitive physical interpretation, nor is it unique. The quaternion representation is not subject to singularities while using only one redundant parameter. Furthermore, the normalization constraint is easily enforced by (2.11) and the successive rotations follow a practical rule. Given two successive rotations represented by the quaternions p and q, the final total rotation can be represented by a quaternion q such that $w = q \otimes p$. Finally, quaternions can also be easily converted into DCM matrix parameters (and vice-versa).

Quaternion to DCM Transformation

The DCM matrix can be described as a function of the attitude quaternion as:

$$\mathbf{A_q} = \begin{bmatrix} q_1^2 - q_2^2 - q_3^2 + q_4^2 & 2(q_1 q_2 + q_3 q_4) & 2(q_1 q_3 - q_2 q_4) \\ 2(q_1 q_2 - q_3 q_4) & -q_1^2 + q_2^2 - q_3^2 + q_4^2 i & 2(q_3 q_2 + q_1 q_4) \\ 2(q_1 q_3 + q_2 q_4) & 2(q_3 q_2 - q_1 q_4) & -q_1^2 - q_2^2 + q_3^2 + q_4^2 \end{bmatrix} \tag{2.23}$$

2.3 Orbital Mechanics

The motion of two celestial bodies 1 and 2 around their mutual center of mass in an inertial reference frame as:

$$\ddot{\mathbf{r}} = -\frac{G(m_1 + m_2)}{r^3}\mathbf{r} \qquad (2.24)$$

where G is the universal gravitational constant ($G = 6.67408 \times 10^{-11} m^3 kg^{-1} s^{-2}$), m_1 and m_2 are the masses of body 1 and 2, respectivelly and $\mathbf{r}$ is the position vector of body 2 relative to body 1. For the case where $m_1 >> m_2$, such as the case of a satellite orbiting around Earth, the center of mass of the system "satellite+Earth" approximately coincides with the center of mass of the planet and (2.24) can be further simplified:

$$\ddot{\mathbf{r}} \approx -\frac{Gm_1}{r^3}\mathbf{r} = -\frac{\mu}{r^3}\mathbf{r} \qquad (2.25)$$

This simplification is known as the restricted two body problem and for the specific case where the Earth is the main body, $\mu = 3.986004418 \times 10^{14} m^3 s^{-2}$.

It is important to notice, however, that Newton's equation of universal gravitation (2.24) approximates the two bodies to two point masses. This model does not account for the influence of the non-symmetric mass distribution of the Earth (which is not a perfect sphere), perturbations due to other celestial bodies as well as non-gravitational forces and torques acting on the spacecraft. The effect of these perturbations will be further discussed in section 2.6.

For an initial condition where six scalar parameters are known, (2.24) can be fully integrated over an indefinite time period. Typical parametrizations consist of the initial position and velocity vectors (each being composed of three scalar parameters) or the Kepler classical parameters: semi-major axis, a, eccentricity e, inclination i, longitude of the ascending node Ω, argument of perigee ω and true anomaly θ. Alternative versions of the Keplerian parametrization are also commonly used, for instance, the true anomaly θ, is frequently substituted by the mean anomaly n.

2.4 Attitude Kinematics

This section presents the attitude kinematics related with the rotation matrix and quaternion representation as this will be relevant to the study of the attitude of the spacecraft over time. Given two different reference frames $\mathbf{F}$ and $\mathbf{G}$, the angular rate of $\mathbf{G}$ with respect to $\mathbf{F}$ is represented by $\boldsymbol{\omega}^{GF}$, then

$$\dot{\mathbf{A}}_{\mathbf{GF}} = -\boldsymbol{\omega}_G^{GF}(t) \times \mathbf{A}_{\mathbf{GF}} = -\begin{bmatrix} 0 & -\omega_3 & \omega_2 \\ \omega_3 & 0 & -\omega_1 \\ -\omega_2 & \omega_1 & 0 \end{bmatrix} \mathbf{A}_{\mathbf{GF}} \qquad (2.26)$$

is the kinematic differential equation that maps the relative orientation of frame $\mathbf{G}$ with respect to frame $\mathbf{F}$ over time, with $\boldsymbol{\omega}_G^{GF} = [\omega_1, \omega_2, \omega_3]^T$ being the representation of $\boldsymbol{\omega}^{GF}$ in coordinates of the $\mathbf{G}$ frame.

11

In quaternion representation the equivalent differential equation is given by [10]:

$$\dot{\mathbf{q}} = \frac{1}{2}\mathbf{q} \odot \boldsymbol{\omega} = \frac{1}{2}\Xi(\mathbf{q})\boldsymbol{\omega} = \frac{1}{2}\boldsymbol{\omega} \otimes \mathbf{q} = \frac{1}{2}\Omega(\boldsymbol{\omega})\mathbf{q} \tag{2.27}$$

where

$$\Omega(\boldsymbol{\omega}) = \begin{bmatrix} 0 & \omega_3 & -\omega_2 & \omega_1 \\ -\omega_3 & 0 & \omega_1 & \omega_2 \\ \omega_2 & -\omega_1 & 0 & \omega_3 \\ -\omega_1 & -\omega_2 & -\omega_3 & 0 \end{bmatrix} \tag{2.28}$$

and $\Xi(\mathbf{q})$ is defined in section 2.2.3.

Finally, the attitude kinematics is of intuitive physical interpretation when represented in vector notation. Given a vector $\mathbf{v}$ with $\mathbf{v_g}$ and $\mathbf{v_f}$ representations in reference frames $\mathbf{G}$ and $\mathbf{F}$, respectively, it can be shown from equations 2.4 and 2.26 that the kinematic differential equation can be described as

$$\dot{\mathbf{v}}_\mathbf{g} = \mathbf{A_{GF}}\dot{\mathbf{v}}_\mathbf{F} - \omega_G^{GF} \times \mathbf{v_g} \tag{2.29}$$

Some important properties of the relative angular rates have intuitive physical interpretation, mainly:

$$\boldsymbol{\omega}^{GF} = -\boldsymbol{\omega}^{FG} \tag{2.30}$$

That is, the angular rate of $\mathbf{G}$ with respect to $\mathbf{F}$ is symmetric of the rate of $\mathbf{F}$ with respect to $\mathbf{G}$, when expressed in the same reference frame [10]. And:

$$\boldsymbol{\omega}^{GF} = \boldsymbol{\omega}^{GH} + \boldsymbol{\omega}^{HF} \tag{2.31}$$

which states that given another reference frame $\mathbf{H}$, the angular rate of $\mathbf{G}$ with respect to $\mathbf{F}$ is equal to the sum of the angular rate of $\mathbf{G}$ with respect to $\mathbf{H}$ and the angular rate of $\mathbf{H}$ with respect to $\mathbf{F}$.

Finally, by differentiating (2.29), the second order derivative (acceleration) of the vector $\mathbf{v}$ as represented in the two reference frames, can be related as:

$$\ddot{\mathbf{v}}_\mathbf{g} = \mathbf{A_{GF}}\ddot{\mathbf{v}}_\mathbf{F} - \omega_G^{GF} \times (\omega_G^{GF} \times \dot{\mathbf{v}}_\mathbf{g}) - 2\omega_G^{GF} \times \dot{\mathbf{v}}_\mathbf{g} - \dot{\omega}_\mathbf{G}^{\mathbf{GF}} \times \mathbf{v_g} \tag{2.32}$$

In the specific case where $\mathbf{v}$ represents a position, $\mathbf{A_{GF}}\ddot{\mathbf{v}}_\mathbf{F}$ represents the relative acceleration between the reference frames, $-\omega_G^{GF} \times (\omega_G^{GF} \times \dot{\mathbf{v}}_\mathbf{g})$ represents the centriptal acceleration, $-2\omega_G^{GF} \times \dot{\mathbf{v}}_\mathbf{g}$ relates to the Coriolis acceleration and $-\dot{\omega}_\mathbf{G}^{\mathbf{GF}} \times \mathbf{v_g}$ to Euler's acceleration.

2.5 Attitude Dynamics

Attitude dynamics is the study of the relationship between angular motion and the torques that influence it. For the present analysis, the satellite will be treated as a rigid body. Euler's second law of

motion states that the rate of change of a body's angular momentum about a fixed point in an inertial reference frame, is equal to the sum of the external torques acting on it. Taking the center of mass of the body as the reference point and the ECI frame as the inertial reference frame:

$$\dot{\mathbf{h}}_{\mathbf{I}}^c = \boldsymbol{\tau}_{\mathbf{extI}} \tag{2.33}$$

Under the rigid body assumption,

$$\mathbf{h}_I^c = \mathbf{J}_I^c \boldsymbol{\omega}_I^{BI} \tag{2.34}$$

where **J** represents the inertia tensor of the spacecraft.

J is a symmetric matrix, dependent on the mass and shape of the satellite. **J** is defined as:

$$\mathbf{J_b} = \begin{bmatrix} \int_B (y_p^2 + z_p^2)\, dm & \int_B -(x_p y_p)\, dm & \int_B -(x_p z_p)\, dm \\ \int_B -(x_p y_p)\, dm & \int_B (x_p^2 + z_p^2)\, dm & \int_B -(z_p y_p)\, dm \\ \int_B -(x_p z_p)\, dm & \int_B -(z_p y_p)\, dm & \int_B (y_p^2 + x_p^2)\, dm \end{bmatrix} \tag{2.35}$$

where P represents a generic body point with infinitesimal mass dm and coordinates $\{x_p, y_p, z_p\}$ in the reference frame. The diagonal elements of the inertia tensor are denominated principal moments of inertia, whereas the off-diagonal terms are called products of inertia. Since the coordinates of P will differ for different frames of reference, J will also differ.

Combining equations (2.33) and (2.29), the fundamental equation of angular motion expressed in body frame coordinates becomes

$$\dot{\mathbf{h}} = \boldsymbol{\tau}_{ext} - \boldsymbol{\omega} \times \mathbf{h} \tag{2.36}$$

where ω represents the angular velocity of the body frame with respect to the inertial frame in body frame coordinates, that is ω_B^{BI}. The subscript B indicating the body reference frame has been omitted for simplicity of notation. Alternatively, from (2.34)

$$\mathbf{J}\dot{\boldsymbol{\omega}} = \boldsymbol{\tau}_{\mathbf{ext}} - \boldsymbol{\omega} \times \mathbf{J}\boldsymbol{\omega} \tag{2.37}$$

where J is defined in the body frame. The main advantage of (2.37) over (2.34) is that, even though J is usually time varying, it's representation in the body frame is constant. In the following subsections, this equation is going to be particularized for the cases where momentum exchange devices are present.

2.5.1 Attitude Dynamics with Momentum Devices

When momentum exchange devices are present, such as reaction/momentum wheels [12, 13] or Single Gimbal Control Momentum Gyros (SGCMGs) [14–18]:, the total angular momentum of the system "spacecraft+momentum devices" about its center of mass is given by:

$$\mathbf{h} = \mathbf{J}\boldsymbol{\omega} + \mathbf{h}^{med} \tag{2.38}$$

where $\mathbf{h}^{med}$ represents the angular momentum of momentum exchange device and J represents the moment of inertia of the system "spacecraft+momentum exchange device". Substituting in (2.37), the equation of angular moment in the body frame, becomes:

$$\mathbf{J}\dot{\boldsymbol{\omega}} = -\boldsymbol{\omega} \times (\mathbf{J}\boldsymbol{\omega} + \mathbf{h^{med}}) - \boldsymbol{\tau} - \dot{\mathbf{h}}^{\mathbf{med}} \qquad (2.39)$$

With $\boldsymbol{\tau}$ comprising both perturbation and other control torques.

2.6 Perturbations

The spacecraft is subjected to several external disturbances. The four most significant perturbations that the satellite is subjected to are caused by the gravitational attraction of a non-spherical Earth and of other celestial bodies other than the central body, the aerodynamic drag and Solar Radiation Pressure (SRP). Since the two first correspond to conservative disturbances, they can be expressed as gradients of potential functions. The last two, however, are dissipative persturbations and other models will be necessary to describe them.

2.6.1 Nonspherical Mass Distribution of the Earth

The planet Earth is not a perfectly uniform sphere. In fact, due to the presence of an equatorial bulge and the flatness of the poles, the configuration of the Earth is closer to the one of a oblate sphere. Other less significant nonuniformities occur due to frequent minor geographic anomalies (i.e. mountains, continents, oceans etc.). Since gravity is directly correlated with mass, these have an impact on the gravitational force acting on the spacecraft. A common approach to model this phenomenon approaches the gravitational force, and consequently, acceleration by an infinite number of harmonics. This model can be obtained by the gravitational potential function [10]:

$$\mathbf{U}(r) = \frac{\mu}{r} \left\{ 1 + \sum_{n=1}^{\infty} (\frac{R_E}{r})^n \sum_{m=0}^{n} P_{nm}(\sin \lambda)[C_{nm} \cos(m\phi) + S_{nm} \sin(m\phi)] \right\} \qquad (2.40)$$

where μ is the gravitational constant of the Earth, r, λ, ϕ are coordinates radius, geocentric latitude and longitude, respectively. R_E is the mean equatorial radius and P_n are the Legendre polynomials. C_{nm}, S_{nm} are geopotential coefficients that decrease as the indexes n and m increase.

The gravitational field is conservative and, therefore, can be written as a gradient of this potential function:

$$\ddot{\mathbf{r}} = -\nabla \mathbf{U} \qquad (2.41)$$

The higher order harmonics (higher n and m) don't alter the total energy of the orbit, due to its conservative nature. However, can cause perturbations of the orbital elements. The most significant perturbation is related to the C_{20} coefficient, also designated J_2 coefficient ($J_n = -C_{n0}$) associated with the oblatedness of the Earth. This leads to the periodic variation of the longitude of the ascending node and the argument of periapsis.

2.6.2 Aerodynamic Perturbations

Drag is a perturbation force caused by the friction of between the satellite and the air molecules that constitute the atmosphere. This force is opposite to the velocity of the satellite relative to the atmospheric flow and, therefore, has a decelerating action.

The drag force is not conservative as it decreases the energy of the system and, therefore, can not be modeled as such. However, some assumptions can be made: the total momentum of the molecules that contact with the surface is lost, the thermal motion of the atmospheric particles is negligible when compared with the velocity of the spacecraft, molecules leaving the surface have a negligible impact on the satellite, the speed of the center of mass of the spacecraft is significantly greater than the relative motion between surfaces and the spacecraft can be modeled as a set of N flat plates (good approximation for several CubeSats) [19, 20]. Under these conditions, the drag force experienced by the spacecraft is given in the body reference frame by:

$$\mathbf{f_B^d} = \sum_{i=1}^{n} \mathbf{f_B^{di}} \tag{2.42}$$

where $\mathbf{f_B^{di}}$ is the drag force applied to panel i, given by:

$$\mathbf{f_B^{di}} = -\frac{1}{2}\rho v_{rel}^2 C_D A_p \hat{\mathbf{v}}_{\mathbf{relB}} \tag{2.43}$$

where ρ is the atmospheric density, C_D is a dimensionless drag coefficient (typically between 1.8 and 2.4) [21], $\mathbf{v_{relB}}$ is the velocity of the spacecraft relative to the air molecules in the atmosphere and A_p is the total projected area of the satellite in direction of motion:

$$A_p = \int_A H(\cos(\alpha))\cos(\alpha)dA \tag{2.44}$$

where $H()$ is the Heaviside function and α is the angle of attack, defined by:

$$\alpha = \arccos(-\hat{\mathbf{v}}_{\mathbf{rel}} \cdot \hat{\mathbf{n}}^{\mathbf{i}}) \tag{2.45}$$

where $\hat{\mathbf{n}}^{\mathbf{i}}$ is the unit inward normal of the face i.

Under the assumption that the atmosphere co-rotates with the Earth:

$$\mathbf{v_{relB}} = \mathbf{v_{satellite}} - \mathbf{v_{atmosphere}} = \mathbf{A_{BI}v_{relI}} \tag{2.46}$$

$$\mathbf{v_{relI}} = \mathbf{v_I} - \boldsymbol{\omega_E} \times \mathbf{r_I} \tag{2.47}$$

where ω_E is the Earth's velocity vector in the ECI frame:

$$\boldsymbol{\omega_E} = \omega_E \hat{\mathbf{i}}_{\mathbf{3}} \tag{2.48}$$

The aerodynamic perturbation is also associated with a perturbation torque τ_B^d. The total torque acting

on the spacecraft is given by:

$$\tau_B^d = \sum_{i=1}^{n} \tau_B^{di} \qquad (2.49)$$

where τ^{di} is given by the cross product between the center of pressure $\mathbf{c_B^{pi}}$ and the drag force $\mathbf{f^{di}}$ of each panel:

$$\tau_B^{di} = [\mathbf{c_B^{pi}} \times] \mathbf{f_B^{di}} \qquad (2.50)$$

2.6.3 Solar Radiation Pressure

Whenever the satellite is not in eclipse another dissipative perturbation arises. The solar radiation perturbation is caused by the exchange of momentum between the spacecraft and the photons that intercept it's surface. This momentum exchange depends on the illuminated area and can be expressed as:

$$\mathbf{f_B^s} = -pA_p\hat{\mathbf{s}}_{\mathbf{B}} \qquad (2.51)$$

where $\mathbf{f_B^s}$ is the force actuating in the satellite, in body frame coordinates, due to the solar pressure p. $\hat{\mathbf{s}}$ is the Sun line-of-sight vector, that is, a unit vector pointing form the satellite in the direction of the Sun and A_p is the illuminated area given by (2.44) with α defined as the angle between the unit inward normal of the face i, $\hat{\mathbf{n}}^{\mathbf{i}}$ and the Sun line-of-sight vector:

$$\alpha = \arccos(-\hat{\mathbf{s}}_{\mathbf{B}} \cdot \hat{\mathbf{n}}_{\mathbf{B}}^{\mathbf{i}}) \qquad (2.52)$$

Some assumptions were made in (2.52): the solar pressure is assumed constant along the entire orbit, the absorption of the momentum of the photons is considered total, thermal radiation emitted by both the spacecraft and other celestial bodies is neglected, self-shadowing of the satellite is not taken into consideration and the relative velocity of a spinning vehicle is considered negligible compared to the speed of light.

The solar radiation pressure is also associated with a torque disturbance given by the cross product between the center of pressure $\mathbf{c_B^p}$ defined in the body reference frame:

$$\mathbf{c^P} = \frac{1}{A} \int_A H(\cos(\alpha))\cos(\alpha)\mathbf{r_{cp}}dA \qquad (2.53)$$

With α defined by (2.52) and the solar radiation pressure perturbation force defined in (2.51):

$$\tau_B^s = [\mathbf{c_B^p} \times] \mathbf{f_B^s} \qquad (2.54)$$

where τ_B^s represents the solar radiation disturbance torque in the body reference frame.

2.6.4 Gravitational Torque

Since the gravitational field acting on the spacecraft is not uniform, as it depends on its action on each infinitesimal particle that constitutes the spacecraft and the position of said particle, a disturbance

torque arises about the center of mass of the satellite. In the body reference frame, the gravity gradient torque is given by:

$$\boldsymbol{\tau}_B^g = 3(\frac{\mu}{r^2})[(\hat{\mathbf{o}}_3)_\mathbf{B}\times]\mathbf{J}_\mathbf{B}(\hat{\mathbf{o}}_3)_\mathbf{B} \tag{2.55}$$

This model only accounts for the first order of the gravitational potential function and is based in some assumptions: the Earth is considered as the only source of gravitational influence and the satellite is considered to be small compared to its distance from the mass center of the planet.

2.6.5 Magnetic Torque

The geomagnetic field is conservative and, therefore, can be written as a gradient of a potential function:

$$\mathbf{B} = -\nabla\mathbf{V} \tag{2.56}$$

Similarly to the gravitational field potential function, V is a potential function with infinite harmonics[10]:

$$\mathbf{V}(r,\phi,\psi) = R_E\Big\{ \sum_{n=2}^{\infty} \sum_{m=0}^{n} (\frac{R_E}{r})^{n+1} P_{nm}(\cos\phi)[g_{nm}\cos(m\psi) + h_{nm}\sin(m\psi)]\Big\} \tag{2.57}$$

where P_{nm} is the Legendre function and g_{nm} and h_{nm} are Gauss coefficients.

Due to it's internal circuits, current loops, electronic devices and scientific instruments, the spacecraft is imbued of a parasitic magnetic dipole whose interaction with the geomagnetic field generates a perturbation torque:

$$\boldsymbol{\tau} = \mathbf{m} \times \mathbf{B} \tag{2.58}$$

where $\mathbf{m}$ is the total parasitic magnetic dipole of the spacecraft.

2.6.6 Third-body Perturbations

In reality, the spacecraft interacts with various gravitational fields other than the one from the Earth. Since these celestial bodies are significantly further away from the spacecraft than planet Earth, the effect of their gravitational fields on the satellite are less important then the contribution of Earth's gravitational field. Hence, these interactions can be treated as perturbations known as "third-body" perturbations.

The influence of n other celestial bodies of mass m_i and position $\mathbf{r_i}$ on a spacecraft with mass m_s at position $\mathbf{r_s}$ orbiting around planet Earth with mass m_E and position $\mathbf{r_E}$ is given by:

$$\ddot{\mathbf{r}}_\mathbf{s} = -\frac{Gm_E}{\|\mathbf{r}_E - \mathbf{r}_s\|^3}(\mathbf{r}_s - \mathbf{r}_E) - \sum_{i=1}^{N} \frac{Gm_i}{\|\mathbf{r}_s - \mathbf{r}_i\|^3}(\mathbf{r}_s - \mathbf{r}_i) \tag{2.59}$$

These n celestial bodies also interact with the planet Earth as:

$$\ddot{\mathbf{r}}_\mathbf{E} = -\frac{Gm_s}{\|\mathbf{r}_E - \mathbf{r}_s\|^3}(\mathbf{r}_E - \mathbf{r}_s) - \sum_{i=1}^{N} \frac{Gm_i}{\|\mathbf{r}_E - \mathbf{r}_i\|^3}(\mathbf{r}_E - \mathbf{r}_i) \tag{2.60}$$

17

The position of a spacecraft orbiting around Earth is typically described as it's position relative to the center of mass of the planet $\mathbf{r} = \mathbf{r_s} - \mathbf{r_E}$. Substituting in (2.59):

$$\ddot{\mathbf{r}} = -\frac{\mu}{r^3}\mathbf{r} - \sum_{i=1}^{N} \mu_i \left(\frac{\mathbf{r}_E - \mathbf{r}_i + \mathbf{r}}{\|\mathbf{r}_E - \mathbf{r}_i + \mathbf{r}\|^3} - \frac{\mathbf{r}_E - \mathbf{r}_i}{\|\mathbf{r}_E - \mathbf{r}_i\|^3} \right) \tag{2.61}$$

where, $\mu = G(m_s + m_E)$ and $\mu_i = Gm_i$.

For satellites orbiting around the Earth, the main perturbations are due to the Sun and the Moon [10]. This model follows some assumptions: the Earth, spacecraft and remaining celestial bodies are assumed to be mass points, therefore, only the first order terms of their gravitational fields are accounted for.

Chapter 3

Sensors and Actuators

This chapter summarizes some of the most common actuators and sensors found in CubeSats as well as typical passive attitude devices and structures commonly utilized. In section 3.1 some of the most common methods and devices of passive attitude control are presented. Sections 3.2 and 3.3 are concerned about sensors and actuator devices. The models used to simulate the hardware available in the simulation tool are further analyzed in chapter 4.1.

3.1 Passive Attitude Control/Stabilization

Passive attitude stabilization and control methods rely on geometric and magnetic properties of the satellite in order to obtain attitude control. Passive methods do not require power consumption or processing and are typically simpler than active methods, which makes them an attractive choice for small satellites. Despite their typically lower performance, the low resource needs of this type of attitude control still make it a common choice for Cubesats. Some commonly used techniques are going to be discussed in the next subsections.

3.1.1 Gravity Gradient Stabilization

Since the gravitational force experienced by a point mass decreases with the increase of the squared distance, r^2, the spacecraft will not experience the same gravity pull in all its parts. This non-uniformity can be taken advantage off in order stabilize the spacecraft's axis of least inertia (maximum kinetic energy state) in the nadir direction.

To achieve this result, gravity gradient stabilization explores the relative equilibrium states in which the rotation of the spacecraft relative to the orbital frame is constant ($\omega^{BO} = 0$). It can be shown that in order to attain this equilibrium, the satellite must have all principle inertia axes aligned with the orbital frame [22].

There is no limitation regarding each inertia axis is pointing towards each orbital frame axis to achieve this equilibrium, however, not all configurations will be stable. [10, 12].

The stability region $J_y \geq J_x \geq J_z$ is typically selected as the design point [10, 12].

For this effect, elongated spacecrafts with a prominent axis of least inertia are preferred. For nadir pointing CubeSats, whose structure is standardized, gravity gradient booms are typically used to "artificially" create a preferable direction of alignment, that is, a well defined axis of least inertia.

3.1.2 Passive Magnetic Attitude Control

Passive Magnetic Attitude Control (PMAC) makes use of the Earth's magnetic field. It consist of a permanent magnet, typically, paired with hysteresis rods which supply restoring and dampening torque, respectively, to the spacecraft. The PMAC is a robust, simple, low size/mass, no-power required attitude control system, which makes it an attractive for CubeSats, whose mass, volume and power budget are reduced. This system is, however, generally limited to an accuracy of 10° around the magnetic field instantaneous direction [23]. PMAC is specially common among missions where magnetic-pointing is necessary.

Permanent Magnet

The permanent magnet are devices made from magnetic material whose magnetic dipole moment produces a torque when interacting with the geomagnetic field. These are passive attitude control devices as they do not require any power, since the material is naturally magnetic, contrary to induced magnets, such as magnetic torquers. The torque provided by a magnetic dipole moment when interacting with a magnetic field is:

$$\mathbf{T} = \mathbf{m} \times \mathbf{B} \tag{3.1}$$

where $\mathbf{m}$ is the permanent magnet's magnetic moment vector and $\mathbf{B}$ is the geomagnetic flux density vector. Contrary to magnetic torquers', permanent magnet's magnetic moment vector is constant.

Hysteresis Rod

In delayed response to magnetic field changes, a hysteresis rod alters its polarity converting the rotational energy into heat and, therefore, providing a dampening torque to the spacecraft [24]. The hysteresis rod's internal induced magnetic flux density is expressed as a function of an external magnetic field strength by its hysteresis loop. The area of the loop is associated with the rotational dampening per cycle per unit volume of the hysteresis rod and its characteristics depend on the material and shape of the hysteresis rod [23, 25]. The magnetic dipole moment provided by a hysteresis rod is a function of it's internal induced magnetic flux density and its volume.

20

3.1.3 Aerodynamic Stabilization
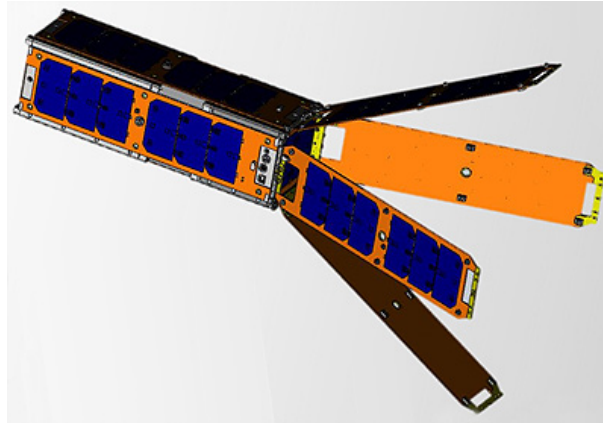
Figure 3.1: USS Langley CubeSat with Pumpkin Colony-I bus [8]

Despite frequently being considered an inconvenience, the aerodynamic torque, explained with further detail in section 2.6, can be taken advantage of to achieve attitude stabilization. For CubeSats, fin or panel like structures are typically used for this purpose, normally deployed in a axially symmetric "shuttlecock" configuration [26], like the one seen in figure 3.1. This configuration achieves stabilization of rotation around axes orthogonal to the symmetry one through gyroscopic stiffness. The premise behind this method of stabilization is the placement of the center of pressure of the spacecraft behind its center of mass so that the drag induced torque acts in as restorative torque [26].

Consider, without loss of generality, a "shuttlecock" configuration around the $\hat{b}_1$ axis. For a positive pitch angle ("nose up") the aerodynamic fins tilt downwards. The area of the aerodynamic fin projected orthogonal to the flow decreases, reducing its drag. Furthermore, this tilt also decreases the vertical moment arm to the center of mass, and therefore, the aerodynamic torque produced by the upper panel. The opposite occurs to the lower fin, whose aerodynamic torque will increase. Therefore, a restorative torque is produced around the center of the mass of the spacecraft, causing the "nose" of the spacecraft to go down to its nominal position. A similar situation occurs for rotations around the yaw axis [27].

This configuration has been adopted by CubeSats such as QbX [26, 28], GalacticSky-1 [29] and Qarman [30]. And a commercial option is offered by Pumpkin Space Systems [26, 31]. This structure is also commonly adopted as a way to deploy solar arrays [27].

3.2   Sensors

The most commonly attitude sensors are presented in the following table along with their main advantages and disadvantages. The sensors developed to complement the ADCS design tool are going to be further described.

Table 3.1: Reference Sensors [10]

Sensor	Measurement	Advantages	Disadvantages
Gyroscope	Body rates	No additional processing needed Low volume Low mass Low cost Low power budget [32]	Reduced lifetime
Sun Sensor	Sun direction	Most commonly used Simple Reliable Specially important for sun pointing modes	Multiple needed Unusable during eclipse
Magnetometer	Instantaneous magnetic field	Low mass Reliable Low power Commonly used High temperature range	Low accuracy
Star tracker	Star Direction	High accuracy	Expensive Heavy Higher power requirements
Horizon sensor	Nadir Direction	High accuracy	Expensive Complex

Earth Sensors

Earth Sensors, also known as nadir or horizon sensors, are not as common as magnetometers and sun sensors, however, the appearance of the first COTS solutions, as well as it's appearance in some more recent satellites, has shown by a survey conducted in the beginning of this work indicates that this sensors are becoming more prominent solutions for CubeSats. Earth sensors are specially useful for nadir-pointing missions, as they supply either the nadir vector direction or the pitch and yaw angles between body and orbit frame.

There are different types of Earth Sensors, such as static Earth sensors and scanning Earth sensors [32], however, the conducted survey showed that more then $\frac{2}{3}$ of the CubeSats equipped with Earth sensors, chose the COTS available solution CubeSense by CubeSpace [33]. This specific sensor is a Complementary Metal-Oxide Semiconductor (CMOS) camera which will detect the Earth disk horizon in

it's field of view and output the nadir direction in the sensor reference frame. This is extremely useful, since, by the definition of orbital frame, the direction of nadir corresponds to the axis $\hat{o}_3$, whose direction in the ECI frame is known and given by equation (2.1).

Star Tracker

A star tracker is a digital camera whose focal plane may be composed either of a Charge-Coupled Device (CCD) or CMOS pixels. Most state of the art star trackers are able to track multiple stars at the same time and, autonomously match the stars in their field of view with an internal catalog, by evaluating star light intensity and relative positions [10]. Typically, only one star-tracker is needed, since these are generally able to provide attitude information relative to three axis [10, 34, 35].

Even though for bigger scale star sensors, accuracy of the order of magnitude of the arcsec are achieved, this performance necessarily degrades as the size of the sensor is reduced, due to the less refined optics. Most state off the art star trackers are able to provide three-axis attitude (and occasionally body rates), usually in the form of a quaternion [32].

3.3 Actuators

In this section, a review of CubeSat actuators is done. Two main actuators, momentum/reaction wheels and control momentum gyros, are explained in more detail. Other spacecraft actuators are also mentioned with less detail.

3.3.1 Magnetorquer

Magnetorquers consist of coils or rods (electromagnets), whose magnetic dipole can be controlled, by means of the alteration of a current. Magnetorquers interact with the geomagnetic field and produce an acting torque in a similar way to permanent magnets (equation (3.1)).

Since the magnetic control torque can only be applied in a plane orthogonal to the instantaneous magnetic field, the satellite is always instantaneously under-actuated when magnetorquers are the only source of control torque [10]. This is the main disadvantage of the active magnetic control system. However, this systems simplicity and low cost makes it a common choice for either primary or secondary attitude control.

3.3.2 Reaction/Momentum Wheels

Flywheels actuation is based on the principle of the conservation of inertia. They act on the satellite attitude not by providing an external torque but by, through spinning, changing it internally and, therefore, forcing the satellite to rotate in the opposite direction in order to conserve the total angular momentum of the "Spacecraft+Flywheels" system [10, 36].

Several flywheels can be used both as reaction wheels or momentum wheels. In momentum wheel mode, the wheel is usually spun up to the maximum speed so as to provide gyroscopic stiffness to the

satellite, by increasing the total angular momentum. This phenomenon, makes the satellite less sensitive to external torques in the direction orthogonal to the spin axis.

When operating as a reaction wheel, the flywheel will possess null nominal angular momentum. This means that the nominal spin speed of the wheel will be zero, except when a torque control command is emitted. The momentum wheel mode is mostly used to contrast the environmental disturbance torques, whereas in the second it is mostly used to perform an attitude maneuver.

3.3.3 Control Moment Gyros

Control Moment Gyros (CMGs) can be divided in dual-gimbal and single-gimbal control moment gyros, according to the number of gimbal axis present. Due to its complexity, dual-gimbal control moment gyros are less commonly used in spacecraft attitude control [10, 22]. Single-gimbal control moment gyros are still not a common solution for CubeSats, nevertheless, a commercial solution by Honeywell [6] is currently available in the market. Moreover, the initial survey conducted in the beginning of this work identified the use of in house developed control moment gyros in recent missions such as SwampSat 1 (1U) [8] and 2 (3U) [9] and KAUSAT-5 [37].

Single-gimbal control moment gyros can be devided in variable speed control moment gyros (VS-GMG), where the spinning disk operates similarly to a reaction wheel, with variable speed and simple single-gimbal control moment gyros, where the spinning disk is spun up to a nominal operating speed (similarly to what happens in a momentum wheel) [14]. The solution presented by Honeywell is inserted in this last category, so this is the type of control momentum gyros that our study will concern about [6] .

Single-gimbal control moment gyros are based on the principle that a rotor spinning at constant speed can be gimbaled to produce an actuating torque. The output torque is not commanded by changing the spin rate of the wheel and, therefore, the magnitude of the angular momentum in the spin direction, like in a reaction wheel, but rather by gimbaling the spin axis and changing the direction of a momentum vector of angular magnitude [14–17].

The main disadvantages of CMG are its complexity and higher mass and size, as well as the existence of singularity states in which the actuator fails to provide the required torque. Nevertheless, since the output torque is proportional to the rate of change of the direction of the angular momentum, the gyroscopic torque is considerably larger than the input gimbal torque, which makes the CMG a power efficient solution compared to reaction wheels. Control moment gyros are also associated with better pointing accuracy [16, 18], agility and maneuverability [38].

Even though CMG can be used in single units, typical configurations of up to four CMG are common. The commercial available solution by Honeywell can be found in single configurations or in clusters of four SGCMG [6].

Chapter 4

Simulation Environment

This chapter presents the simulation tool developed. In section 4.1 makes a general overview of the tool. Sections 4.2 to 4.8 explain with deeper detail each of the blocks that constitute the simulation tool.

4.1 General Overview

The simulink simulation tool is divided in two main areas: an upper area that comprises all the environment, spacecraft, sensor and actuator models, as well as a model of the on board computer and estimation and control algorithms and a lower area devoted to graphical analysis and data output.
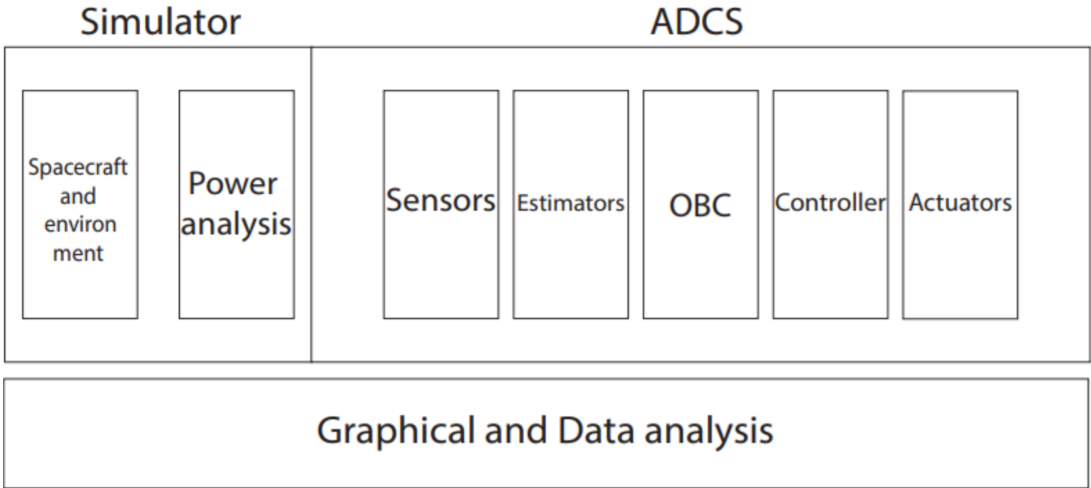
Figure 4.1: Simulink ADCS Simulator tool

The upper area is divided into a simulator area, which simulates the interaction of the spacecraft with the space environment and the ADCS area, which simulates the attitude subsystem on board the CubeSat. Each of these areas is divided into blocks (figure 4.1) which are explained in sections 4.2 to 4.8. Each section does an overview of functions performed by each block, explaining in depth relevant models. The interaction between each block is shown in figure 4.2.
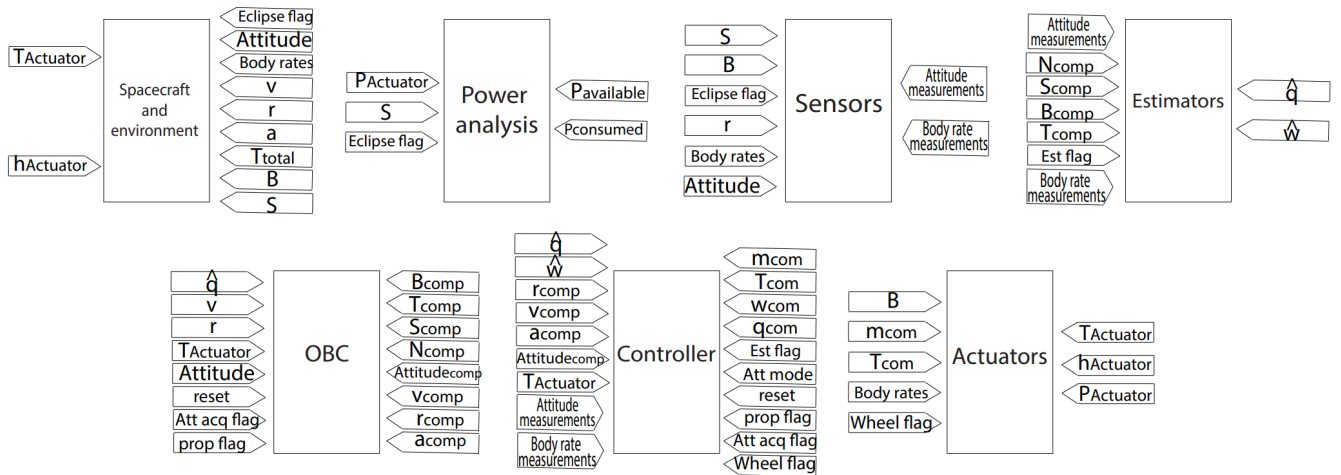
Figure 4.2: Interaction between blocks

4.2 Spacecraft Mechanics Simulator Block

This block simulates the space environment experienced in orbit, namely, the geomagnetic field, the gravitational field and sun position. This block also reproduces the translation and rotation motion of the satellite through the orbital and attitude mechanics equations as well as the perturbations presented in chapter 2. Finally, this block contains models of the passive attitude stabilization structures and devices whose models are presented in section 4.2.1.

4.2.1 Passive Attitude Stabilization

Gravity Gradient Boom

Since CubeSats have standard bus structures, a common technique used to ensure the gravity gradient stability condition involves the deployment of one or more gravity gradient booms (figure 4.3).
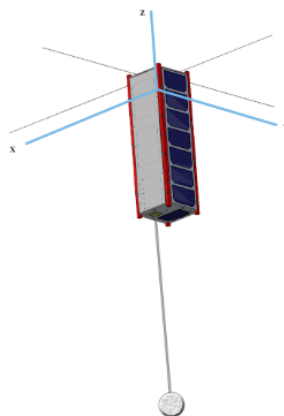
Figure 4.3: 3U CubeSat with gravity gradient boom [39]

Gravity gradient booms are small masses attached to a long thin rod (figure 4.3), along the axis that is desired to be aligned with the nadir direction.

The small tip masses are modeled as solid spheres. In the tip reference frame, $\mathbf{T} = \{\hat{\mathbf{t}}_1, \hat{\mathbf{t}}_2, \hat{\mathbf{t}}_3\}$, centered in the CM of the mass tip, with axis parallel to the rod's coordinate system the tensor of inertia of the mass tip is:

$$\mathbf{J_T^{tip}} = \begin{bmatrix} \frac{2}{5}m_{tip}r^2 & 0 & 0 \\ 0 & \frac{2}{5}m_{tip}r^2 & 0 \\ 0 & 0 & \frac{2}{5}m_{tip}r^2 \end{bmatrix} \tag{4.1}$$

where m_{tip} is the mass of the tip weight and r is its radius.

Whereas the rods are modeled as a thin, slender rod with mass of m_{rod} and length of l. Its coordinate system, $\mathbf{R} = \{\hat{\mathbf{r}}_1, \hat{\mathbf{r}}_2, \hat{\mathbf{r}}_3\}$ is centered in its center of mass, with axis $\hat{\mathbf{r}}_3$ aligned with the symmetry axis of the rod. In this reference frame, the inertia tensor of the rod is:

$$\mathbf{J_R^{rod}} = \begin{bmatrix} \frac{1}{12}m_{rod}l^2 & 0 & 0 \\ 0 & \frac{1}{12}m_{rod}l^2 & 0 \\ 0 & 0 & 0 \end{bmatrix} \tag{4.2}$$

To obtain the inertia tensor of the mass and tip in the body frame it is first necessary to express it reference frames centered in their respective centers of mass, but with axes parallel to the body axes, $\mathbf{T}'$ and $\mathbf{R}'$,respectively. This is obtained by applying the inertia rotation transformation [40]:

$$\mathbf{J_{R'}^{rod}} = \mathbf{A_{BR}}\mathbf{J_R^{rod}}\mathbf{A_{BR}^T} \tag{4.3}$$

where $\mathbf{A_{BR}}$ is the rotation matrix that transforms the rod reference frame in a reference frame with axis parallel to the body frames. Note that for gravity gradient booms aligned with $\hat{\mathbf{b}}_3$, $\mathbf{J_{R'}^{rod}} = \mathbf{J_R^{rod}}$ and that, due to its symmetry, the inertia tensor of the mass tip doesn't change.

Secondly, the parallel axis theorem is applied to the inertia tensor obtained in (4.3) to obtain the inertia tensor of each component in the body frame (centered in the center of mass of the spacecraft) [40–42]:

$$\mathbf{J_B^{rod}} = \mathbf{J_{R'}^{rod}} + m_{rod}(d_{rod}^2\mathbf{I_{4\times4}} - \mathbf{d_{rod}}\mathbf{d_{rod}^T}) \tag{4.4}$$

$$\mathbf{J_B^{tip}} = \mathbf{J_{T'}^{tip}} + m_{rod}(d_{tip}^2\mathbf{I_{4\times4}} - \mathbf{d_{tip}}\mathbf{d_{tip}^T}) \tag{4.5}$$

where $\mathbf{d_{tip}}$ and $\mathbf{d_{rod}}$ are the displacement of the center of mass of the spacecraft from the center of mass of the tip mass and rod, respectively. The deployment of gravity gradient booms will cause the position of the center of mass of the system spacecraft ("hub+gravity gradient booms") to change. By definition, the center of mass of a system of n bodies is given by:

$$\mathbf{d_{CM}} = \frac{\int \rho(\mathbf{d})\mathbf{d}dV}{\int \rho(\mathbf{d})dV} \approx \frac{\sum_{i=1}^{N} m_i d_i}{\sum_{i=1}^{N} m_i} \tag{4.6}$$

The total moment of inertia in the body frame is given by: [43]

$$\mathbf{J_B} = \mathbf{J_B^{hub}} + \sum_{i=1}^{N} \mathbf{J_B^{tipi}} + \sum_{i=1}^{N} \mathbf{J_B^{rodi}} \tag{4.7}$$

where $\mathbf{J_B^{hub}}$, $\mathbf{J_B^{tipi}}$ and $\mathbf{J_B^{rodi}}$ are the inertia tensors of the hub, mass tip i and rod i, respectively in the body frame of a spacecraft with n booms.

Both $\mathbf{J_B}$ and the center of mass will change during the deployment process. In reality, the hub of the spacecraft is much heavier than the mass tips and the rods, hence the total center of mass of the system will be very close to the center of mass of the hub.

The gravity gradient boom deployment is modeled as uniform, that is:

$$\mathbf{d_{tipi}} = \mathbf{d_{tipi0}} + \mathbf{d_{tipi}'}t \tag{4.8}$$

$$\mathbf{d_{rodi}} = \mathbf{d_{rodi0}} + \mathbf{d_{rodi}'}t \tag{4.9}$$

where $\mathbf{d_{tipi0}}$ and $\mathbf{d_{rodi0}}$ are the initial positions of the center of mass of the tip mass i and thin rod i, respectively, in the stowed configuration. $\mathbf{d_{tipi}'}$ and $\mathbf{d_{rodi}'}$ are the constant rate of change in the position of the centers of mass of of the tip mass i and thin rod i, respectively.

The Simulink tool allows the user to insert up to two gravity gradient booms, since the initial survey conducted showed that the two most common gravity gradient stabilization techniques applied by Cube-Sats is the deployment of either a single or a pair of symmetric gravity gradient booms along the axis that is intended to point to nadir.

The contribution of gravity gradient boom to the spacecrafts aerodynamic and solar radiation perturbation assumed to be negligible.

Permanent Magnet

Permanent magnets are devices used in passive magnetic attitude control architectures. These provide a control torque (figure 4.4) caused by the interaction of a magnetic dipole moment with a magnetic field of the Earth [10]:

$$\mathbf{T} = \mathbf{m} \times \mathbf{B} \tag{4.10}$$

where $\mathbf{m}$ is the permanent magnet's magnetic moment vector and $\mathbf{B}$ is the magnetic flux density vector.
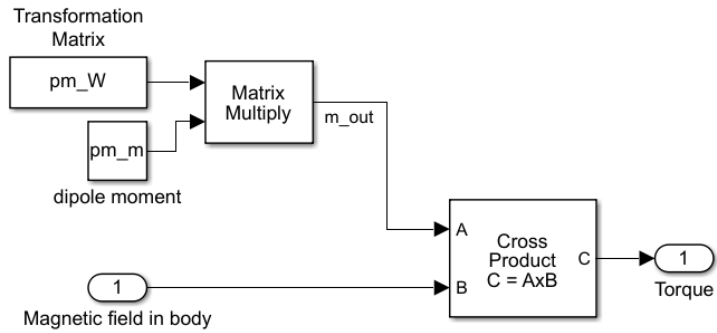
Figure 4.4: Permanent magnet model

Note that the torque produced will be orthogonal to both the magnetic dipole moment and the magnetic flux density vectors, therefore, at any instant, this system is not able to control the attitude of the satellite in the magnetic field direction. Nevertheless, since the direction of the magnetic flux density vector changes during the orbit, globally, all directions will be controllable.

Permanent magnets are usually accompanied by hysteresis rods and are typically placed orthogonal to them.

Hysteresis Rod

Hysteresis rods are made of a ferromagnetic material and provide passive oscillation-damping and de-spin torques. Hysteresis rods are characterized by their hysteresis $B_{rod}(H)$ loop, that is, the component of the geomagnetic field vector, of magnetic field strength H, parallel to the axis of the rod will induce a magnetic flux density (B_{rod}) in the rod that produces a magnetic moment parallel to the axis (figure 4.5) [23]:

$$\mathbf{m} = \frac{\mathbf{B_{rod}} V_{rod}}{\mu_0} \tag{4.11}$$

where μ_0 represents the magnetic permeability of vacuum and V_{rod} is the volume of the rod. Similar to the permanent magnet, the magnetic dipole moment will interact with the geomagnetic field and supply a torque given by (4.10).
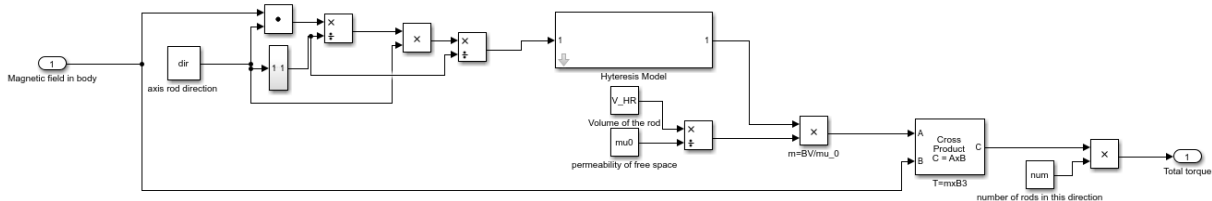
Figure 4.5: Hysteresis rod model

The phenomenon behind $B_{rod}(H)$ loops is extremely complex, non-linear and dependent on several variables, such as material and rod length-to-diameter ratio [44]. However, several mathematical models exist to try and replicate with more or less precision the hysteresis loops. Figure 4.6 shows a hysteresis

loop boundary modeled according to Flatley's [44] hysteresis model. Different characteristic parameters of hysteresis loops, namely, saturation, remanence and coercivity.
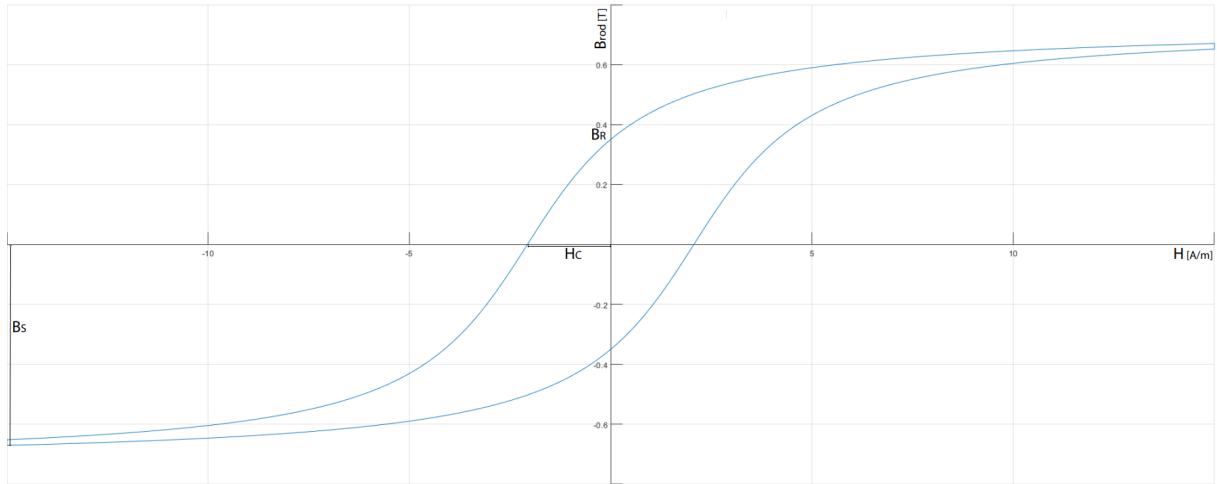
Figure 4.6: Hysteresis loop

The Simulink tool presents the magnetic hysteresis model presented in [44]. This model divides the boundary of the hysteresis loop (Br/H curve) into two distinct boundaries, a left curve and a right curve and approximates them by arctangent functions:

$$B_{rod} = \frac{2}{\pi} B_S \arctan[k(H_L + H_C)] \tag{4.12}$$

$$B_{rod} = \frac{2}{\pi} B_S \arctan[k(H_R - H_C)] \tag{4.13}$$

where B_{rod} stands for the magnitude of the internal induced magnetic flux density of the rod ($-B_S \geq B_{rod} \leq B_S$) parallel to its elongated symmetry axis B_S represents the magnetic flux saturation of the rod, H_C represents the coercivity (H_L for $B_{rod} = 0$) and H_L and H_R represent the value of the external magnetic field strength on the left and right boundary curves, respectively. k is a constant given by:

$$k = \frac{1}{H_C} \tan(\frac{\pi B_r}{2 B_S}) \tag{4.14}$$

where B_r is the magnetic remanence, that is, the value of the induced magnetization B_{rod} when $H_L = 0$.

From (4.12) and (4.13) it is trivial to see that the external magnetic field strength on the left H_L and right H_R boundaries of the loop are given by:

$$H_L = \frac{\tan(\frac{\pi B_{rod}}{2 B_S})}{k} - H_C \tag{4.15}$$

$$H_R = \frac{\tan(\frac{\pi B_{rod}}{2 B_S})}{k} + H_C \tag{4.16}$$

The behavior inside the boundaries and in the first magnetization phase ($H_0 = B_{rod0} = 0$) is given as a

function of the slope of the boundary curves , B'_{rod}, and the fractional horizontal distance between the left and right boundaries, f:

$$f = \frac{H - H_L}{2H_C} \tag{4.17}$$

$$B'_{rod} = \frac{2}{\pi} B_S k \cos(\frac{\pi}{2} \frac{B_{rod}}{Br_S})^2 \tag{4.18}$$

For positive values of $\frac{dH}{dt}$, the behavior inside the boundaries can be expressed as a function of these parameters as:

$$\frac{dB_{rod}}{dH} = [q_0 + (1 - q_0)f^p]B' \tag{4.19}$$

where q_0 and p are shape parameters that can be empirically determined for different rod materials and shapes.

If $\frac{dH}{dt}$ is negative, B_{rod} should be taken from the right side of the boundary and in equation 2.57 the value f shall be replaced with $(1 - f)$.

By applying the chain rule

$$\frac{dB_{rod}}{dt} = \frac{dB_{rod}}{dH}\frac{dH}{dt} = \frac{1}{\mu_0}\frac{dB_{rod}}{dH}\frac{dB}{dt} \tag{4.20}$$

Therefore, by integration the internal induced magnetic flux density of the rod and, consequently it's magnetic dipole (equation (4.11)) can be expressed as a function of the rate of change of the geomagnetic field vector in the body reference frame.

By allowing for the definition of several different loops, by the variation of two shape related parameters q_0 and p, this model allows the user to experiment with several different hysteresis loops and, therefore, hysteresis rods with different materials and shapes. It also permits the achievement of loops extremely close to the real ones.

One disadvantage of this model is that there is no explicit relation between the defined parameters and physical parameters of the hysteresis rods, hence, the selection of this constants has to be achieved by fine-tuning the hysteresis loop obtained shape with empirical data.

The algorithm that models the hysteresis loop of a rod is summarized in table 5.1.

Table 4.1: Hysteresis Loop model algorithm

Step	
1.	Compute the value of H on the left boundary curve, H_L corresponding to B_rod (4.15).
2.	Compute the boundary curve slope,, corresponding to B_rod (4.18).
3.	Compute f (4.17) if $\frac{dH}{dt} > 0$ or $(1 - f)$ in other case
4.	Compute $\frac{dB_{rod}}{dH}$ (4.19)
5.	Compute $\frac{dB_{rod}}{dt}$ (4.20)

Validation of the Passive Magnetic Stabilization

To study the behavior of the passive magnetic stabilization system, a satellite with similar body and orbit to the ORCASat was used. This spacecraft was only equipped with a $0.48 Am^2$ permanent magnet (aligned with the $\hat{b}_3$ axis) and 2 hysteresis rods with volume equal to $6.2 \times 10^{-5} m^3$, $p = 4.75$ and $q_0 = 0.085$.
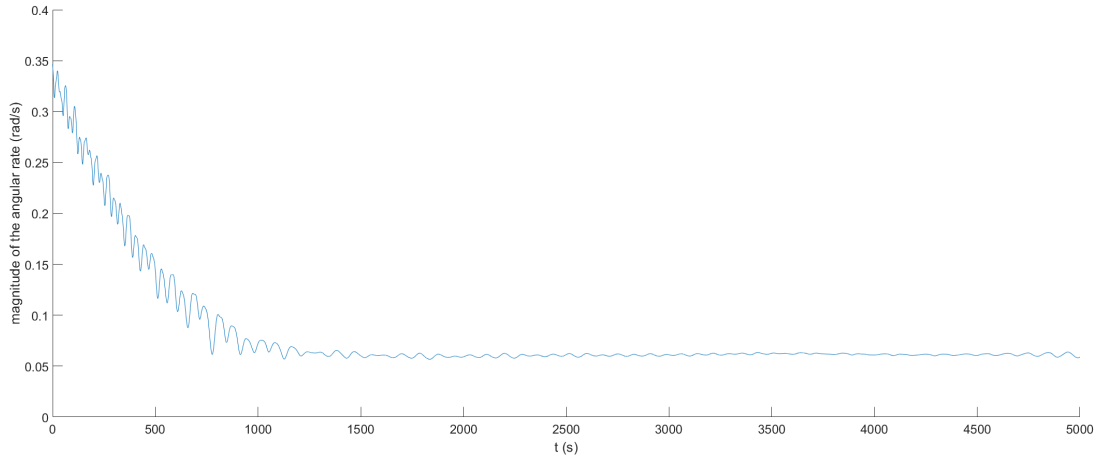
Figure 4.7: Decrease of the magnitude of the angular rates
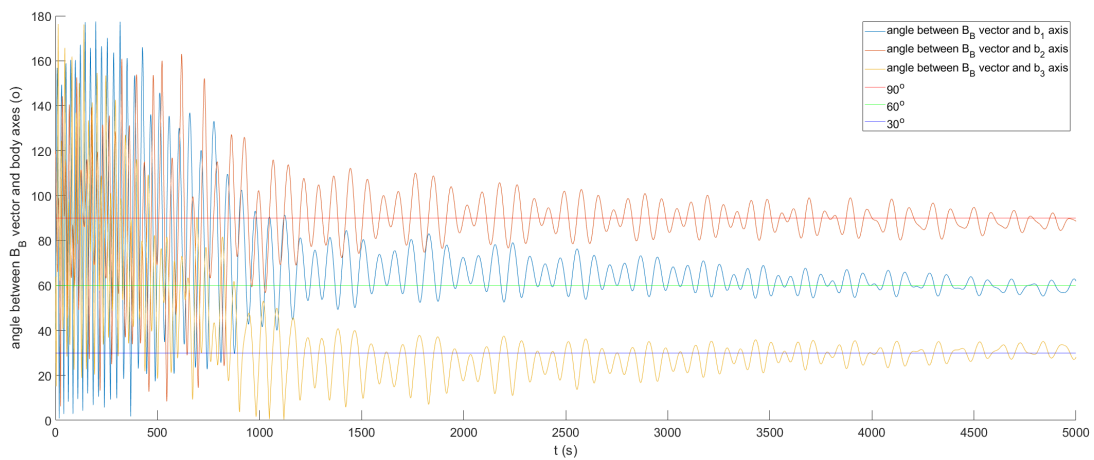
Figure 4.8: Angle between the magnetic vector and body axes

As it can be seen in figures 4.7 and 4.8, the passive magnetic system was capable of reduce the angular speed of the spacecraft from $0.3464 rad/s$ to approximately $0.062 rad/s$ in less than 2000s, aligning the $\hat{b}_2$ orthogonal to the magnetic vector and maintaining a mean angle of approximately 60° and 30°, respectively, with axes $\hat{b}_1$ and $\hat{b}_3$.

Aerodynamic Stabilization Panels

A "shuttlecock" configuration (figure 4.9) of panels was modeled. Each panel is modeled as a rectangular flat plate similarly to the spacecraft surfaces in 2.6.2. The aerodynamic effect of the panel structure

is explained similarly to the one due to body surfaces explained in section 2.6.2.
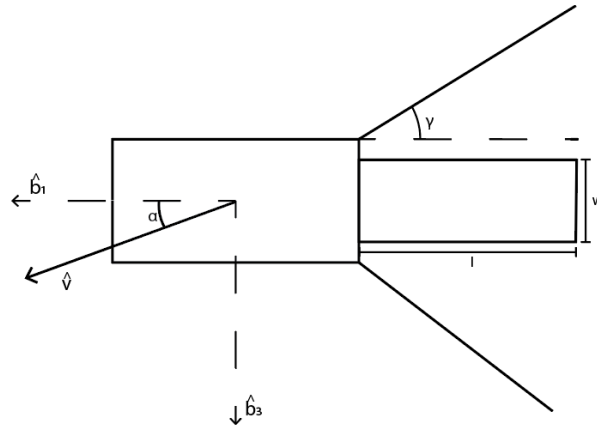
Figure 4.9: Shuttlecock configuration

For a "shuttlecock" configuration, the inward normal of the panels is defined as a function of the angle γ as seen in figure 4.9 [45]:

$$\mathbf{n_{i1}} = \begin{bmatrix} -\sin(\gamma_1) \\ -\cos(\gamma_1) \\ 0 \end{bmatrix} \quad (4.21) \qquad \mathbf{n_{i2}} = \begin{bmatrix} -\sin(\gamma_2) \\ \cos(\gamma_2) \\ 0 \end{bmatrix} \quad (4.22)$$

$$\mathbf{n_{i3}} = \begin{bmatrix} -\sin(\gamma_3) \\ 0 \\ -\cos(\gamma_3) \end{bmatrix} \quad (4.23) \qquad \mathbf{n_{i4}} = \begin{bmatrix} -\sin(\gamma_4) \\ 0 \\ \cos(\gamma_4) \end{bmatrix} \quad (4.24)$$

The deployment of aerodynamic panels will impact the tensor of inertia of the spacecraft. The moment of inertia of each panel of mass m in a reference frame centered in its center of mass and whose axes $\mathbf{P} = \{\hat{\mathbf{p}}_1, \hat{\mathbf{p}}_2, \hat{\mathbf{p}}_3\}$ aligned with its width, w, length, l, and depth is given by [40]:

$$\mathbf{J_R^{rod}} = \begin{bmatrix} \frac{l^2}{12}m & 0 & 0 \\ 0 & \frac{w^2}{12}m & 0 \\ 0 & 0 & \frac{l^2+w^2}{12}m \end{bmatrix} \tag{4.25}$$

The impact of the panels on the total inertia tensor is, typically, much smaller than the one caused by gravity gradient booms, but is analogous to the process described by equations (4.3) to (4.7). The contributions of the panels to the solar radiation perturbation have been neglected.

33

The deployment of the panels has been modeled as uniform:

$$\gamma_i = \gamma_{i0} + \gamma_i' t \tag{4.26}$$

where γ_i is the initial angle of panel i in the stowed configuration. γ_i' is the constant rate of change in the angle.

Figure 4.10 shows the model of the contribution of these panels to the projected area and center of pressure of the spacecraft. The contribution of these panels to the total aerodynamic force and torque are given by equations (2.43) and (2.50), respectively.
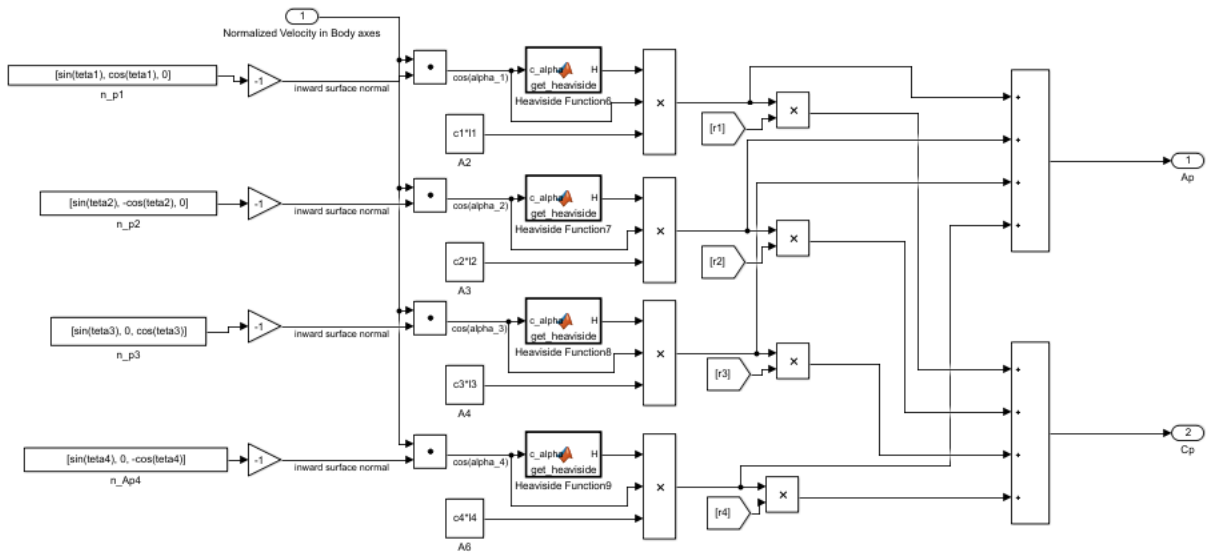
Figure 4.10: Contribution of the Shuttlecock aerodynamic panels to the projected area and center of pressure of the spacecraft

4.3 Sensors Block

The sensors block models the behavior of typical Cubesat attitude sensors, namely, sun sensors, magnetometers and gyroscopes, which can be found in ORCASat's ADCS and whose models are explained in depth in [20, 46], as well as earth sensors and star trackers.

4.3.1 Earth Sensor

Figure 4.11 shows the geometry of a typical Earth sensor problem. The Earth sensor is modeled mounted along the axis $\mathbf{b_3}$ of the body frame. This is a typical configuration as this axis is commonly desired to be aligned with the nadir direction. Other mounting configurations are possible without loss of generality, however, conversions between the sensor reference frame and the body reference frame will be necessary.

34
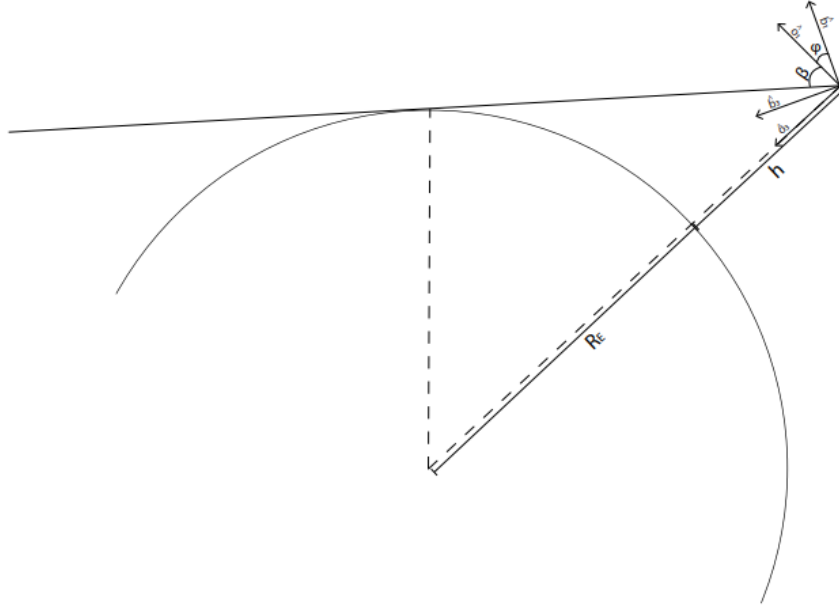
Figure 4.11: Geometry of a typical Earth sensor mounted along the $\mathbf{b_3}$ axis

The Earth sensors detect points in the Earth horizon. The direction of these points in the body frame is given by [34]:

$$\mathbf{y}_e = \begin{bmatrix} \phi_e \\ \theta_e \end{bmatrix} = \begin{bmatrix} \phi \\ \theta \end{bmatrix} + \begin{bmatrix} \beta_{xo} \\ \beta_{yo} \end{bmatrix} + \mathbf{v}_e \tag{4.27}$$

With ϕ_e and θ_e represent the angle between the body roll and pitch axes, respectively, and the horizon direction and ϕ and θ represent the true Euler angles that map the relation between body frame and orbital frame. β_{xo} and β_{yo} are the roll and pitch angular displacements between the Earth's horizon and the orbit frame. $\mathbf{v}_e$ is the white Gaussian noise with null mean and σ_e standard deviation.

Figure 4.11 evidences the geometry behind this mathematical model. Assuming a perfectly spherical Earth with constant, uniform radiation, the relative roll β_{xo} and pitch angle β_{yo} will be equal and independent of latitude and longitude of the satellite. Note that, even though 4.11 only displays the xz-plane cross-section, under the stated assumption, the same conditions apply to the yz-plane. Therefore, β_{xo} and β_{yo} can be determined by [34]:

$$\beta_{xo} = \beta_{yo} = \frac{\pi}{2} - \arcsin \frac{R_E}{R_E + h} = \frac{\pi}{2} - \arcsin \frac{R_E}{x_i} \tag{4.28}$$

where R_E is the equatorial radius of the Earth and h is the orbit altitude. $\dfrac{R_E}{R_E + h}$ represents the radius of "Earth disk" as seen from the sensor and x_i is the magnitude of the position vector in the inertial frame.

By the definition of the orbital frame and Euler angles provided, the measured nadir direction as seen

from the body frame is given by:

$$\mathbf{n_B} = \mathbf{A_{BO}n_O} = \begin{bmatrix} -\sin\theta \\ \sin\theta\sin\phi \\ \cos\theta\cos\phi \end{bmatrix} \tag{4.29}$$

Note that the knowledge of the yaw angle is not necessary to obtain the nadir direction. Therefore, an estimation of the nadir vector can be obtained from the observed vectors $\mathbf{y_e}$ and the position vector estimated by the OBC (on board computer). Most state of the art nadir sensors are capable of calculating the nadir direction and giving it directly (figure 4.12).
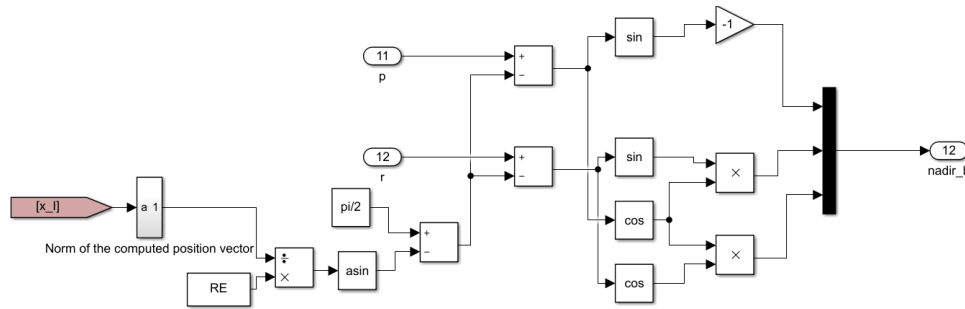
Figure 4.12: Nadir direction measurement

The Earth sensor available in the simulation tool was modeled after the CubeSpace's CubeSense Nadir Sensor. This sensor consists of a CMOS based digital camera with a wide field of view.

The model represented in figure 4.13 imitates the geometric problem behind the Earth sensor, as well as the disturbances of the measurements caused by white Gaussian noise introduced by the electronics, limited field of view, limited precision/sensitivity determined by the pixel size and sampling.
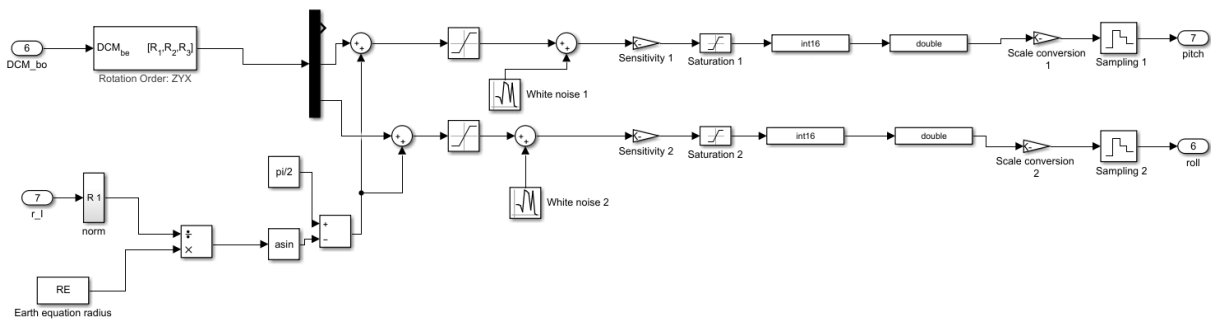
Figure 4.13: Earth sensor model

4.3.2 Star Tracker

Most state-of-the art star trackers provide the attitude of the satellite directly as a quaternion [10]. In the current tool, the star tracker is modeled as a "black box" and the internal processes of this sensor were not taken into account. The star tracker provides the attitude measurement in quaternions. This

measurement is corrupted by additive Gaussian white noise that is added to each element of the quaternion. As seen in figure 4.14, brute force normalization is required to ensure that the output is a unit quaternion.
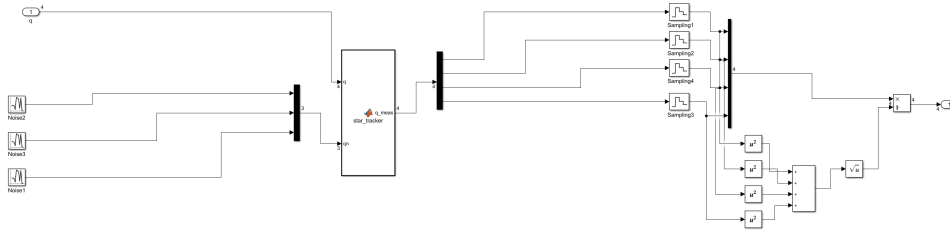
Figure 4.14: Star Tracker model

4.4 Attitude Estimator Block

This block presents multiple options of both static and recursive algorithms. Static determination algorithms are deterministic methods that, at any given time, require at least two measurements. Recursive determination algorithms resort to stochastic methods so as to be able to provide an estimation of attitude parameters when less than two measurements are available.

4.4.1 Static Determination

Static determination algorithms that can be used either on their own, to achieve attitude quaternion knowledge or to initialize recursive methods of estimation. The three options available for the user are the TRIAD algorithm, utilized in the ORCASat, and explained in depth in [13, 46], the QUEST and the Q-method. Despite being slightly more complex than the TRIAD, these two last solutions have the advantages of accepting data from more than two measurements and utilizing complete information of all the measurements to obtain an estimation [10]. Both the Q-method and QUEST are based on Whaba's problem.

Whaba's Problem

Wahba's problem tries to find a rotation matrix between two reference frames from a set of weighted vector observations. This problem is posed as a minimization problem where the cost function is posed as:

$$\mathbf{J} = \frac{1}{2} \sum_{k=1}^{N} a_k \|\mathbf{v_{kB}} - \mathbf{A_{BI}}\mathbf{v_{kI}}\|^2 \tag{4.30}$$

where $\mathbf{v_{1I}}...\mathbf{v_{nI}}$ is a set of reference unit vectors, that is n known directions, in a reference coordinate frame, typically the ECI reference frame, and $\mathbf{v_{1B}}...\mathbf{v_{nB}}$ are the corresponding observation unit vectors, measured in the body frame and $\mathbf{A}$ is the rotation matrix from the reference frame to the body frame. $a_1...a_n$ is a set of non-negative weights that establish how much each measurement is to be trusted.

37

Q-method

The loss function (4.30) can be expanded as:

$$\mathbf{J} = \frac{1}{2}\sum_{k=1}^{N} a_k (\mathbf{v_{kB}} - \mathbf{A_{BI}v_{kI}})^T (\mathbf{v_{kB}} - \mathbf{A_{BI}v_{kI}}) = \frac{1}{2}\sum_{k=1}^{N} a_k (\mathbf{v_{kB}}^T \mathbf{v_{kB}} + \mathbf{v_{kI}}^T \mathbf{v_{kI}} - 2\mathbf{v_{kB}}^T \mathbf{A_{BI}v_{kI}}) \quad (4.31)$$

Since $\mathbf{v_{kB}}$ and $\mathbf{v_{kI}}$ are unit vectors $\mathbf{v_{kB}}^T \mathbf{v_{kB}} = \mathbf{v_{kI}}^T \mathbf{v_{kI}} = 1$. Substituting in (4.31):

$$\mathbf{J} = \sum_{k=1}^{N} a_k - g(\mathbf{A}) \quad (4.32)$$

With $g(\mathbf{A}) = \sum_{k=1}^{N} a_k \mathbf{v_{kB}}^T \mathbf{A_{BI}v_{kI}}$. Minimizing $\mathbf{J}$ is the same as maximizing $g(\mathbf{A})$.

As presented in section 2.2.3 the attitude matrix $\mathbf{A_{BI}}$ can be expressed in terms of quaternions so the cost function can be re-written in terms of quaternions as [47]:

$$g(\mathbf{q}) = \mathbf{q}^T \mathbf{K}(\mathbf{B})\mathbf{q} \quad (4.33)$$

where $\mathbf{K}(\mathbf{B})$ is the traceless symmetric matrix:

$$\mathbf{K}(\mathbf{B}) = \begin{bmatrix} \mathbf{B} + \mathbf{B^T} - tr(\mathbf{B})\mathbf{I_3} & -\mathbf{Z} \\ \mathbf{Z}^T & tr(\mathbf{B}) \end{bmatrix} \quad (4.34)$$

with,

$$\mathbf{B} = \sum_{i=1}^{N} a_k \mathbf{v_{kB}v_{kI}}^T \quad (4.35)$$

and

$$\mathbf{Z} = \begin{bmatrix} B_{23} - B_{32} \\ B_{31} - B_{13} \\ B_{12} - B_{21} \end{bmatrix} \quad (4.36)$$

To find the value of $\mathbf{q}$ that maximizes $g(\mathbf{q})$, its derivative with respect to $\mathbf{q}$ must be evaluated. Since the four elements of the quaternion are not independent, a new gain function is created with this constraint in mind through the addition of a Lagrange multiplier [47]:

$$g(\mathbf{q})' = \mathbf{q}^T \mathbf{K}(\mathbf{B})\mathbf{q} - \lambda \mathbf{q}^T \mathbf{q} \quad (4.37)$$

The differentiation of this gain function yields a stationary point for:

$$\mathbf{q}\mathbf{K}(\mathbf{B}) = \lambda \mathbf{q} \quad (4.38)$$

This equation can be treated as an eigenvalue problem and, therefore, the optimal quaternion will correspond to a eigenvector of $\mathbf{K}$. Substituting (4.38) in (4.33) it is trivial that the eigenvector that maximizes the gain function is the one that corresponds to the largest eigenvalue.

The main fault of this method concerns the case when the two largest eigenvalues are equal, in which the solution of the Q-method is not unique. This means that there is no sufficient data to determine the attitude uniquely. Nevertheless, the Q-method remains one of the best ways to solve Whaba's problem [10] if eigenvalue decomposition methods are available.

QUEST

This method reformulates this problem in a way that avoids the need to perform iterative operations on 4×4 matrices like in Davenport's Q-method. Instead utilizes iterative scalar computations followed by simple matrix multiplications, a less computationally heavy method [10]. Recalling equation (4.32) and substituting for a maximum value of $g(\mathbf{A}) = \lambda_{opt}$:

$$\lambda_{opt} = \sum_{k=1}^{N} a_k - \mathbf{J} \tag{4.39}$$

Acknowledging the fact the optimal eigenvalue of $\mathbf{K}$ the cost function $\mathbf{J}$ should be small, such that [47, 48]:

$$\lambda_{opt} \approx \sum a_k \tag{4.40}$$

Starting from this assumption (λ_0 given by (4.40)) and since the QUEST algorithm obtains an estimate value λ_{opt} through a Newton-Raphson iteration process [48]:

$$\lambda_i = \lambda_{i-1} - \frac{f(\lambda_{i-1})}{f\prime(\lambda_{i-1})} \tag{4.41}$$

where $f(\lambda)$ is the characteristic equation:

$$f(\lambda) = \det\left(\mathbf{K} - \lambda\mathbf{I_{4 \times 4}}\right) \tag{4.42}$$

For most cases, only a single iteration is required [10]. By combining (4.34) and (4.38) and substituting the known optimal eigenvalue λ_{opt}, the optimal quaternion is given by:

$$\frac{\mathbf{q_{1:3}}}{q_4} = [(\lambda_{opt} + tr\mathbf{B})\mathbf{I_3} - \mathbf{S}]^{-1}\mathbf{Z} \tag{4.43}$$

$$\|\mathbf{q}\| = 1 \tag{4.44}$$

where 4.44 states the unit quaternion condition.

Even though in theory it is less robust than the Q-method, the QUEST method has been proven to be extremely robust in practical applications [10]. The QUEST method encounters a singularity for rotations of 180° about any of the axis ($q_4 = 0$). Nevertheless, this singularity can be avoided by applying a method of sequential rotations.

Method of Sequential Rotations

A rotation of an angle greater than 90° can always be described as a rotation of 180° about one of the coordinate axes followed by a rotation about a new axis of less than 90° [48]. Hence, if the attitude corresponds to a $180o$ rotation about one of the body frame axis and a singularity occurs, there is always an alternative reference frame where the singularity is guaranteed to not occur.

A initial rotation of 180° about one of the coordinate axes is equivalent to changing the signs of two components of each of the reference vectors. For initial rotations of 180° around the $\hat{\mathbf{b}}_1$, $\hat{\mathbf{b}}_2$ and $\hat{\mathbf{b}}_3$ axes, the reference vectors in the new reference frame $\mathbf{v'_{kI}}$ are, respectively, given by [48]:

$$\mathbf{v'_{kI}} = (v'_{kI1}, -v'_{kI2}, -v'_{kI3}) \tag{4.45}$$

$$\mathbf{v'_{kI}} = (-v'_{kI1}, v'_{kI2}, -v'_{kI3}) \tag{4.46}$$

$$\mathbf{v'_{kI}} = (-v'_{kI1}, -v'_{kI2}, v'_{kI3}) \tag{4.47}$$

and optimal quaternion $\mathbf{q}$ in the body frame can be expressed as a function of the quaternion in the new reference frame $\mathbf{q'}$ as:

$$\mathbf{q} = (q'_4, -q'_3, q'_2, -q'_1)^T \tag{4.48}$$

$$\mathbf{q} = (q'_3, q'_4, -q'_1, -q'_2)^T \tag{4.49}$$

$$\mathbf{q} = (-q'_2, q'_1, q'_4, -q'_3)^T \tag{4.50}$$

For initial rotations around the $\hat{\mathbf{b}}_1$, $\hat{\mathbf{b}}_2$ and $\hat{\mathbf{b}}_3$ axes, respectively.

TRIAD vs QUEST vs Q-method

The TRIAD, QUEST and Q-method algorithms where compared for a set of sun and magnetic measurements. The performance of the three algorithms is very similar being virtually indistinguishable in figure 4.15, nevertheless, the QUEST algorithm achieved the best results with an average 1.4443^o estimation error, followed by the q-method, 1.4450^o, and then TRIAD 1.6524^o. The performance of the algorithms will be affected by the simulation scenario and a Monte Carlo simulation should be used to compare their performance, this is however, out of the scope of this thesis.
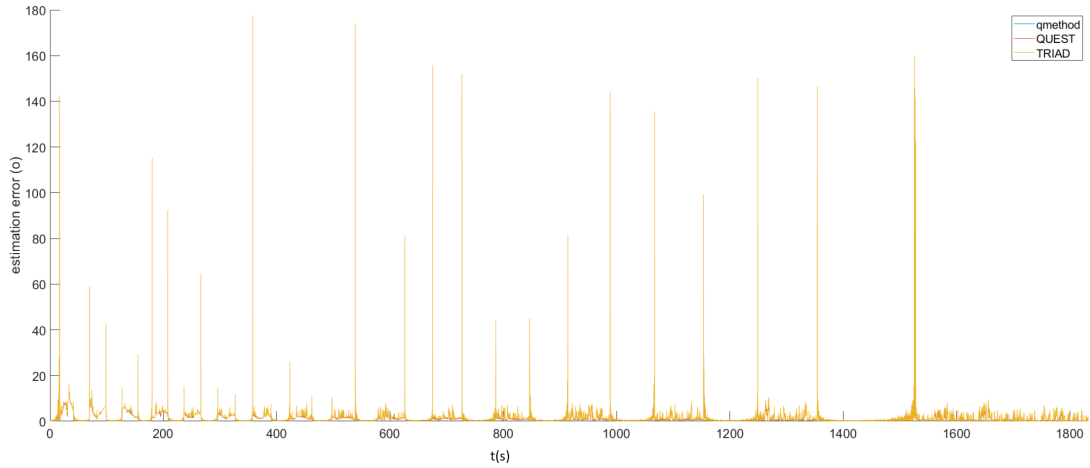
Figure 4.15: Estimation error of the TRIAD, QUEST and Q-method algorithms

4.4.2 Extended Kalman Filters

Recursive (Stochastic) methods are of special importance when it is not possible to obtain at least two valuable measurements required by static algorithms (for instance, in eclipse, if the system relies on sun sensors or when the object whose direction is being used as reference, or a star or Earth is not within the field of view of the sensor). By combining the sensors' observations with a prediction step derived from the satellites dynamics and kinematic equations, recursive algorithms can provide more reliable attitude estimations [49]

The Extended Kalman Filter (EKF) is a type of Kalman Filter which linearizes the a system about an estimate of the current mean and covariance. For non-linear systems, the efficacy and low complexity of the EKF make it a frequent option.

The attitude estimator block is equipped with three different EKF. Two Kalman filters are suitable for vector measurements: a multiplicative extended Kalman filter for spacecrafts equipped with magnetometers and gyroscopes and an additive extended Kalman filter for satellites equipped with magnetometers, sun sensors and/or earth sensors. These filters are explained in depth in [46]. The last Kalman filter is designed for star tracker that output the attitude measurement as a quaternion.

A non-linear system can be represented by the differential equations:

$$\dot{\mathbf{x}}(t) = \mathbf{f}(\mathbf{x}(t), \mathbf{u}(t)) + \mathbf{G}(t)\mathbf{w}(t) \tag{4.51}$$

where $\mathbf{x}$ is th $n \times 1$ state vector, $\mathbf{u}$ is an $m \times 1$ known input vector, $\mathbf{f}$ is a sufficiently differentiable vector function and $\mathbf{w} \sim \mathcal{N}(0, \mathbf{Q}(t))$ is a zero-mean Gaussian white-noise process vector with spectral density matrix $\mathbf{Q}$. Whereas the measurements can be represented by the model:

$$\mathbf{y}(t) = \mathbf{h}(\mathbf{x}(t)) + \mathbf{v}(t) \tag{4.52}$$

where, $\mathbf{y}(t)$ is the measurement vector, $\mathbf{h}(\mathbf{x}(t))$ is the observation vector function and $\mathbf{v}(t) \sim \mathcal{N}(0, \mathbf{R}(t))$

41

is a zero-mean Gaussian white noise measurement vector.

Predict Step

The predict step propagates the state vector and covariance matrices estimations obtained after the update step of a previous iteration (or of a initial guess, in the first iteration) and obtains a new predicted estimated value for the new iteration. An estimated value of the state vector $\hat{\mathbf{x}}$ is defined by:

$$\hat{\mathbf{x}} = E\{\mathbf{x}(t)\} \tag{4.53}$$

where the $E\circ$ is the expected value operator. That is:

$$\dot{\hat{\mathbf{x}}}(t) = \mathbf{f}(\dot{\hat{\mathbf{x}}}(t), \mathbf{u}(t)) \tag{4.54}$$

The extended Kalman filter (EKF) assumes that the true and estimated states are sufficiently close so that the error dynamics can be represented by a linearized first-order Taylor series expansion with a sufficiently high accuracy. Discretizing, through finite difference methods:

$$\hat{\mathbf{x}}_k^- \approx \mathbf{F}(\hat{\mathbf{x}}_{k-1}^+)\hat{\mathbf{x}}_{k-1}^+ + \mathbf{B}\mathbf{u}_{k-1} \tag{4.55}$$

where the superscript "-" indicates an estimate value that has not been updated yet and the superscript "+" indicates an already updated estimation. The state transition matrix $\mathbf{F}$ and the input transition matrix $\mathbf{B}$ are defined as:

$$\mathbf{F} = \left.\frac{\partial \mathbf{f}}{\partial \mathbf{x}}\right|_{\hat{\mathbf{x}}} \tag{4.56}$$

$$\mathbf{B} = \left.\frac{\partial \mathbf{f}}{\partial \mathbf{u}}\right|_{\hat{\mathbf{x}}} \tag{4.57}$$

The error of the prediction step is, by definition:

$$\mathbf{e}_k^- = \mathbf{x}_k - \hat{\mathbf{x}}_k^- \tag{4.58}$$

This error is not taken account in the predicted state, however, it's covariance will also be propagated in the predict step. The covariance matrix of $\dot{\mathbf{e}}_k^-$ is given by:

$$\mathbf{P}_k^- = E\{\mathbf{e}_k[\mathbf{e}_k^-]^T\} \tag{4.59}$$

From equations (4.55), (4.60) and discretizing (4.51), the covariance matrix will be propagated in the predict step as:

$$\mathbf{P}_k^- = \mathbf{F}_{k-1}^+\mathbf{P}_{k-1}^+(\mathbf{F}_{k-1}^+)^T + \mathbf{G}\mathbf{Q}\mathbf{G}^T \tag{4.60}$$

Update Step

The update step improves the predicted estimated values by taking into account the data obtained by the sensor measurements. The measurement model presented in (4.52) is discretized through finite difference methods as:

$$\mathbf{y}_k = \mathbf{h}(\mathbf{x}_k) + \mathbf{v}_k \tag{4.61}$$

where $\mathbf{h}(\mathbf{x}_k)$ can be approximated by:

$$\mathbf{h}(\mathbf{x}_k) \approx \mathbf{h}(\hat{\mathbf{x}}_k) + \mathbf{H}_k(\mathbf{x}_k - \hat{\mathbf{x}}_k) \tag{4.62}$$

$\mathbf{H}$ is known as the measurement sensitivity matrix, given by:

$$\mathbf{H} = \left.\frac{\partial \mathbf{h}}{\partial \mathbf{x}}\right|_{\hat{\mathbf{x}}} \tag{4.63}$$

In the update stage, the estimated state vector is corrected with the new observation as:

$$\hat{\mathbf{x}}_k^+ = \hat{\mathbf{x}}_k^- + \Delta\hat{\mathbf{x}} = \hat{\mathbf{x}}_k^- + \mathbf{K}_k[\mathbf{y}_k - \mathbf{H}_k\mathbf{x}_k^-] \tag{4.64}$$

where $\Delta\hat{\mathbf{x}}$ is a correction applied to the predicted state. This correction reflects the difference between the predicted estimated state at iteration k and the measured state at this iteration. $\mathbf{K}_k$ is the Kalman matrix, which serves as an index of how much the measurement data can be trusted. The Kalman matrix is given by the minimization of the cost function:

$$\mathbf{J_k} = tr(\mathbf{P}_k^+) \tag{4.65}$$

where $\mathbf{P}_k^+$ is the updated covariance matrix given by:

$$\mathbf{P}_k^+ = E\{\mathbf{e}_k^+[\mathbf{e}_k^+]^T\} \tag{4.66}$$

where $\mathbf{e}_k^+$ is the update error defined as:

$$\mathbf{e}_k^+ = \mathbf{x}_k - \hat{\mathbf{x}}_k^+ \tag{4.67}$$

Substituting (4.64) and the discretized (4.51) in (4.67) and applying (4.66):

$$\mathbf{P}_k^+ = (\mathbf{I}_n - \mathbf{K}_k\mathbf{H}_k)\mathbf{P}_k^- \tag{4.68}$$

Therefore yielding:

$$\mathbf{K}_k = \mathbf{P}_k^-\mathbf{H}_k^T(\mathbf{H}_k\mathbf{P}_k^-\mathbf{H}_k^T + \mathbf{R})^{-1} \tag{4.69}$$

In the first iteration, an initial guess is necessary for faster conversion. For this purpose, static algorithms can be used to initialize the Kalman filter. Moreover, good knowledge of the process behind the

propagation of the state system vector and of the measurements conduced by the sensors is necessary. Therefore, good knowledge of the environment and disturbances applied on the satellite is necessary, as well as good knowledge of the spacecraft parameters.

The EKF algorithms used in this thesis are summarized in table 4.2.

Table 4.2: General EKF algorithm

Step	
1.	Calculate $\mathbf{F}(\hat{\mathbf{x}}^+_{k-1})$ and $+\mathbf{B}\mathbf{u}_{k-1}$
2.	Calculate $\hat{\mathbf{x}}^-_{\mathbf{k}} = \mathbf{F}(\mathbf{x}^+_{\mathbf{k-1}})\mathbf{x}^+_{\mathbf{k-1}} + \mathbf{B}\mathbf{u}_{\mathbf{k-1}}$
3.	Calculate $\mathbf{P}^-_k = \mathbf{F}^+_{k-1}\mathbf{P}^+_{k-1}(\mathbf{F}^+_{k-1})^T + \mathbf{G}\mathbf{Q}\mathbf{G}^T$
4.	Calculate $\mathbf{H}_k$
5.	Calculate $\mathbf{K}_k = \mathbf{P}^-_k\mathbf{H}^T_k(\mathbf{H}_k\mathbf{P}^-_k\mathbf{H}^T_k + \mathbf{R})^{-1}$
6.	Calculate $\Delta\hat{\mathbf{x}} = \mathbf{K}_k[\mathbf{y}_k - \mathbf{H}_k\mathbf{x}^-_k]$
7.	Calculate $\hat{\mathbf{x}}^+_k = \hat{\mathbf{x}}^-_k + \Delta\hat{\mathbf{x}}$
8.	Calculate $\mathbf{P}^+_k = (\mathbf{I}_n - \mathbf{K}_k\mathbf{H}_k)\mathbf{P}^-_k$

For each iteration, steps 1. to 8. are followed. The first 3 steps correspond to the predict phase and the remaining to the update phase. When the quaternion is part of the state vector, $\hat{\mathbf{q}}^+_k$ is divided by its norm in step 7. in order to maintain the unit value:

$$\hat{\mathbf{q}}^+_{kcorrected} = \frac{\hat{\mathbf{q}}^+_k}{\|\hat{\mathbf{q}}^+_k\|} \tag{4.70}$$

$\mathbf{F}(\hat{\mathbf{x}}^+_{k-1})$ and $+\mathbf{B}\mathbf{u}_{k-1}$ depend on the process and on the state vector $\mathbf{x}$ and $\mathbf{H}_k$ depends on the sensor measurements and the state vector. Its calculations will be particularized for the star tracker additive EKF developed in the following subsection.

Additive Extended Kalman Filter

The additive extended Kalman filter treats the four elements of the quaternion as independent of each other, relaxing the normalization condition and calculating the quaternion error as [50]:

$$\mathbf{q} = \hat{\mathbf{q}} + \mathbf{\Delta}\mathbf{q} \tag{4.71}$$

where $\hat{\mathbf{q}}$ is the estimated value of $\mathbf{q}$ and $\mathbf{\Delta}\mathbf{q}$ is the estimation error. The normalization condition is enforced in the update state using the "brute force" approach expressed in (4.70).

The AEKF estimates the state vector:

$$\mathbf{x} = \begin{bmatrix} \mathbf{q} \\ \omega \end{bmatrix} \tag{4.72}$$

where $\mathbf{q}$ stands for the unit quaternion and ω represents the body rates. The value of $\dot{\mathbf{x}}$ can be calculated

44

by combining the previously stated equations of kinematics and dynamics:

$$\dot{\mathbf{q}} = \frac{1}{2}\Omega(\boldsymbol{\omega})\mathbf{q} \tag{4.73}$$

$$\mathbf{J}\dot{\boldsymbol{\omega}} = -\boldsymbol{\omega} \times (\mathbf{J}\boldsymbol{\omega} + \mathbf{h}) - \tau - \dot{\mathbf{h}} \tag{4.74}$$

where $\mathbf{h}$ is the angular momentum exchange device $\mathbf{h^{med}}$, when reaction wheels, momentum wheels or control moment gyros cluster are present. When the satellite is not equipped with moment devices $\mathbf{h} = \mathbf{0}$.

Predict

The predict step follows the steps 1-3 in table 4.2, where the error transition matrix is obtained by substituting (4.73) and (4.74) in (4.55):

$$\mathbf{F_{k-1}} = \mathbf{I_7} + \begin{bmatrix} \mathbf{F_{11}} & \mathbf{F_{21}} \\ \mathbf{F_{12}} & \mathbf{F_{22}} \end{bmatrix} \tag{4.75}$$

$$\mathbf{F_{11}} = \frac{\Delta t}{4} \begin{bmatrix} 0 & (\omega_z)_{k-1}^+ & -(\omega_y)_{k-1}^+ & (\omega_x)_{k-1}^+ \\ -(\omega_z)_{k-1}^+ & 0 & (\omega_x)_{k-1}^+ & (\omega_y)_{k-1}^+ \\ (\omega_y)_{k-1}^+ & -(\omega_x)_{k-1}^+ & 0 & (\omega_z)_{k-1}^+ \\ -(\omega_x)_{k-1}^+ & -(\omega_y)_{k-1}^+ & -(\omega_z)_{k-1}^+ & 0 \end{bmatrix} \tag{4.76}$$

$$\mathbf{F_{12}} = \frac{\Delta t}{4} \begin{bmatrix} (q_4)_{k-1}^+ & -(q_3)_{k-1}^+ & (q_2)_{k-1}^+ \\ (q_3)_{k-1}^+ & (q_4)_{k-1}^+ & -(q_1)_{k-1}^+ \\ -(q_2)_{k-1}^+ & (q_1)_{k-1}^+ & (q_4)_{k-1}^+ \\ -(q_1)_{k-1}^+ & -(q_2)_{k-1}^+ & -(q_3)_{k-1}^+ \end{bmatrix} \tag{4.77}$$

$$\mathbf{F_{21}} = \mathbf{0_{3\times4}} \tag{4.78}$$

$$\mathbf{F_{22}} = \Delta t \begin{bmatrix} 0 & \dfrac{(\omega_z)_{k-1}^+(J_y - J_z) - (h_z)_{k-1}^+}{2J_x} & \dfrac{(\omega_y)_{k-1}^+(J_y - J_z) - (h_y)_{k-1}^+}{2J_x} \\ \dfrac{(\omega_z)_{k-1}^+(J_z - J_x) - (h_z)_{k-1}^+ - H_0}{2J_y} & 0 & \dfrac{(\omega_x)_{k-1}^+(J_z - J_x) - (h_x)_{k-1}^+}{2J_y} \\ \dfrac{(\omega_y)_{k-1}^+(J_x - J_y) - (h_y)_{k-1}^+ + H_0}{2J_z} & \dfrac{(\omega_x)_{k-1}^+(J_x - J_y) - (h_x)_{k-1}^+}{2J_z} & 0 \end{bmatrix} \tag{4.79}$$

where H_0 is the orbit angular momentum.

As previously stated in (4.55):

$$\hat{\mathbf{x}}_{\mathbf{k}}^- = \mathbf{F}(\mathbf{x_{k-1}^+})\mathbf{x_{k-1}^+} + \mathbf{Bu_{k-1}} \tag{4.80}$$

With

$$\mathbf{Bu_{k-1}} = \begin{bmatrix} \mathbf{0_{4\times1}} \\ \mathbf{J}^{-1}[\tau_{k-1} - \dot{\mathbf{h}}_{k-1}]\delta t \end{bmatrix} \tag{4.81}$$

The efficiency accuracy of this EKF is strongly dependent on robust environment models and strong estimation of the satellite parameters as this significantly affect (4.81)

Update

Most commercially available star trackers output directly the attitude of the satellite as a quaternion:

$$\hat{\mathbf{y}}_{\mathbf{k}} = \mathbf{h}(\mathbf{x}_k) = \hat{\mathbf{q}}_{\mathbf{k}}^{-} \tag{4.82}$$

applying (4.63) to (4.82) the sensitivity matrix in step 4. of table 4.2 is simply given by [34]:

$$\mathbf{H}_{\mathbf{k}} = \begin{bmatrix} \mathbf{I_{4x4}} & \mathbf{0_{4x3}} \end{bmatrix} \tag{4.83}$$

After this calculation, the algorithm follows steps 5. to 8. of table 4.2, with normalization of $\hat{\mathbf{q}}_k^{+}$ (equation (4.70)), for each iteration.

4.4.3   Validation of the Algorithm

This algorithm was tested with a token star tracker with sampling rate of $0.1s$ and white gaussian noise with standard deviation of $\sigma = 1.2 \times 10^{-3}$. The results can be seen in figures 4.16 and 4.17. The mean estimation error achieved was 0.0864^{o} and body rate errors of $\begin{bmatrix} 4.2406 \times 10^{-4} & -4.5248 \times 10^{-5} & -3.0209 \times 10^{-5} \end{bmatrix}^{T}$.
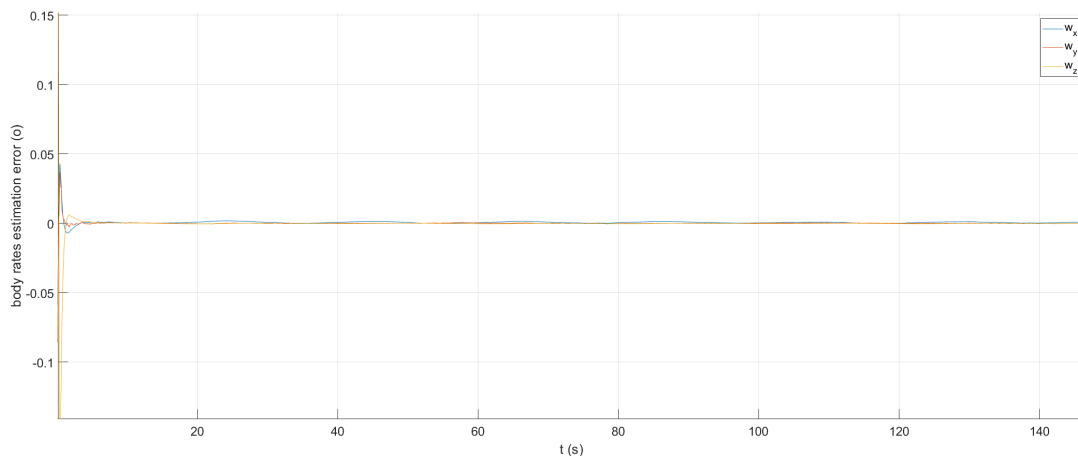
Figure 4.16: Angular rate estimation error: detailed view
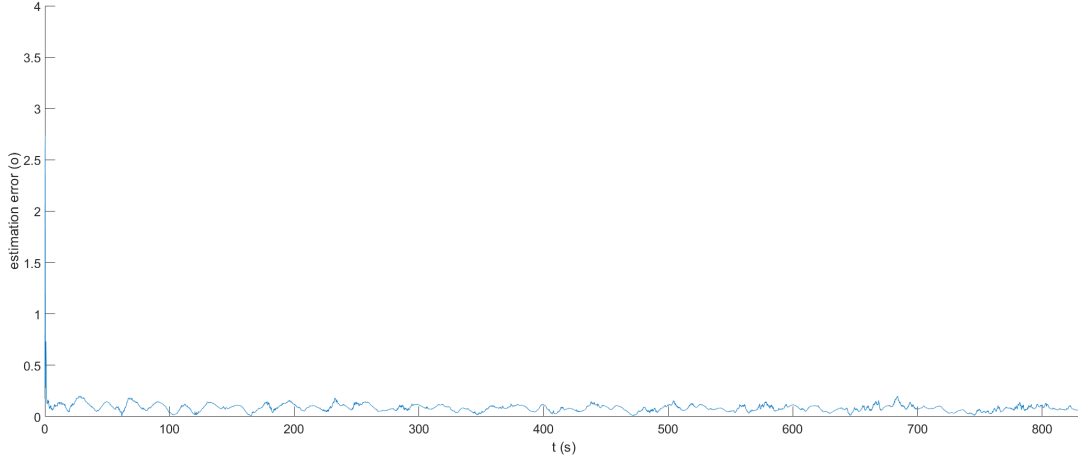
Figure 4.17: AEKF estimation error

4.5 On Board Computer Block

The On Board Computer (OBC) block uses data obtained by the attitude sensors and/or the attitude determination algorithms in conjunction to position measurements obtained by the Global Positioning System (GPS) to compute an estimate of all the kinematic and dynamic variables.

This block contains an environmental model subsystem that, similarly to the spacecraft environment block, models the gravitational and magnetic fields and calculates the both the sun direction and eclipse occurrence and a perturbation model subsystem that estimates the disturbance forces and torques experienced by the spacecraft in any instance (explained in depth in section 2.6). Finally, a propagator subsystem propagates both the position and attitude of the spacecraft along its orbit (section 2.3). This propagator is reset at regular intervals (defined by the OBC controller in the attitude control block, section 4.8) by the GPS measurements in order to reduce the accumulation of estimation errors propagated over time.

4.6 Power Analysis Block

As suggested by the name, this block analyses the power consumption and availability of the satellite.

The power consumption is obtained by adding the power consumed by all the actuators at any time instance. The power availability (figure 4.18) of a spacecraft with N solar panel covered surfaces (either body mounted or deployable solar arrays) is calculated as:

$$P = \sum_{i=1}^{N} max\{P_i^{max} \cos \alpha_i, 0\} \tag{4.84}$$

where P is the total power available and α_i is the angle between the sun unit vector, computed in the spacecraft mechanics block, and the panel inward normal. P_i^{max} is the peak power of the solar panel for a constant power density of $1350W/m^2$. For surfaces with no solar panels, $P_i^{max} = 0$.
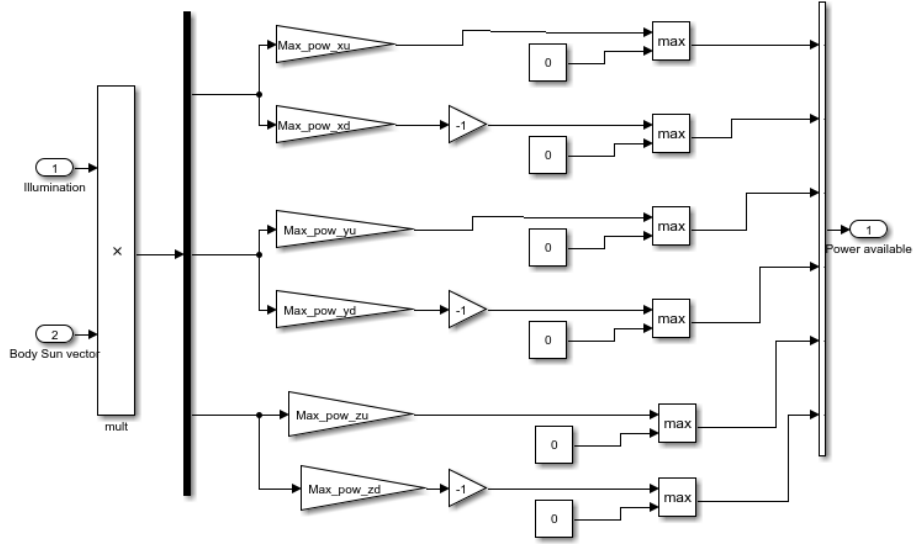
Figure 4.18: Power analysis for body mounted solar panels

This analysis does not take into account self-shadowing caused by other parts of the satellite.

4.7 Actuators Block

This block models different attitude actuators available for CubeSats, namely, magnetometers and momentum wheels, whose models are further explained in [46], reaction wheels and control moment gyros, whose models are going to be further explained in sections 4.7.1 and 4.7.2, respectively. Several cluster architectures for each momentum exchange device.

4.7.1 Reaction Wheel Model

Reaction wheels consist of a rotating disk (flywheel), normally supported by ball bearings, an internal Brushless Direct Current (BLDC) electric motor, and electronics. Configurations of one or two reaction wheels, are commonly used, but full three-axis attitude control requires the use of three or more wheels. The actuator model allows the user to simulate clusters of up to 3 orthogonal reaction wheels.

The angular momentum of a cluster of reaction wheels given in the body frame by:

$$h = \sum_{i=1}^{N} h = \sum_{i=1}^{N} \mathbf{J^{RW}} \Omega^{RW} \mathbf{\hat{g}_{si}} \tag{4.85}$$

where $\mathbf{J_i^{RW}}$, Ω^{RW} and $\mathbf{\hat{g}_{si}}$ represent, respectively, the moment of inertia, the magnitude of the spin rate and a unit vector in the direction of the spin axis of the ith wheel in the body frame.

Applying (2.33) the torque of a cluster of reaction wheels in the body frame is:

$$\boldsymbol{\tau} = \sum_{i=1}^{N} \boldsymbol{\tau_i} = \mathbf{J^{RW}} \dot{\Omega}^{RW} \mathbf{\hat{g}_{si}} \tag{4.86}$$

Torque Transfer

The actuator block allows for architectures of up to 3 orthogonal reaction wheels to be modeled. Due to the orthogonality of the reaction wheels, a torque command issued in the body frame, is simply expressed in the wheel i reference frame as:

$$\tau_{Wi} = \boldsymbol{\tau_B} \cdot \hat{\mathbf{g}}_{\mathbf{siB}} \tag{4.87}$$

where $\boldsymbol{\tau_B}$ is the commanded torque in the body frame, $\hat{\mathbf{g}}_{\mathbf{siB}}$ is a unit vector in the direction of the spin axis of the ith wheel in body frame coordinates and τ_{Wi} is the magnitude of the command torque of the ith reaction wheel.

Note that, equation (4.87) highlights the fact that in order for 3-axis control to be achieved, at least 3 reaction wheels are necessary.

Motor Model

A basic Direct Current (DC) motor (figure 4.19) can be modeled as an armature circuit, constituted of a resistence (R_a) and an inductance (L_a) connected in series, and a voltage source (e_b) associated with the back electromotive force (emf) induced in the armature during rotation [51, 52]. While the torque of a DC motor t_M is proportional to the armature current i_a:

$$\tau_m = K_i i_a \tag{4.88}$$

Its speed is proportional to the voltage [52]:

$$e_b = K_b \frac{d\theta}{dt} \tag{4.89}$$

In (4.88), the proportionality constant K_i is denominated torque constant and, in (4.89), K_b represents the back emf constant.

Combining Newton's and Kirchoff's laws, the behavior of the motor can be described by:

$$L_a \frac{di_a}{dt} + R_a i_a = e_a - K_b \frac{d\theta}{dt} \tag{4.90}$$

$$J \frac{d^2\theta}{dt^2} + \tau_d = K_i i_a \tag{4.91}$$

where τ_d is the friction disturbance torque modeled as a combination of viscous and Coulomb friction contributions [10]:

$$\tau_d = B_m \frac{d\theta_{rel}}{dt} + csign(\frac{d\theta_{rel}}{dt}) \tag{4.92}$$

where B_m is the viscous friction coefficient, c is the Coulomb friction coefficient. And $\frac{d\theta_{rel}}{dt}$ is the relative

velocity between the moving parts of the motor and the static ones (fixed to the spacecraft):

$$\frac{d\theta_{rel}}{dt} = \frac{d\theta_{rel}}{dt}\hat{\mathbf{g}}_{\mathbf{si}} - \boldsymbol{\omega}_{sat} \cdot \hat{\mathbf{g}}_{\mathbf{si}}$$ (4.93)

Disturbances caused by eccentricity of the wheel have been modeled as gaussian white noise.
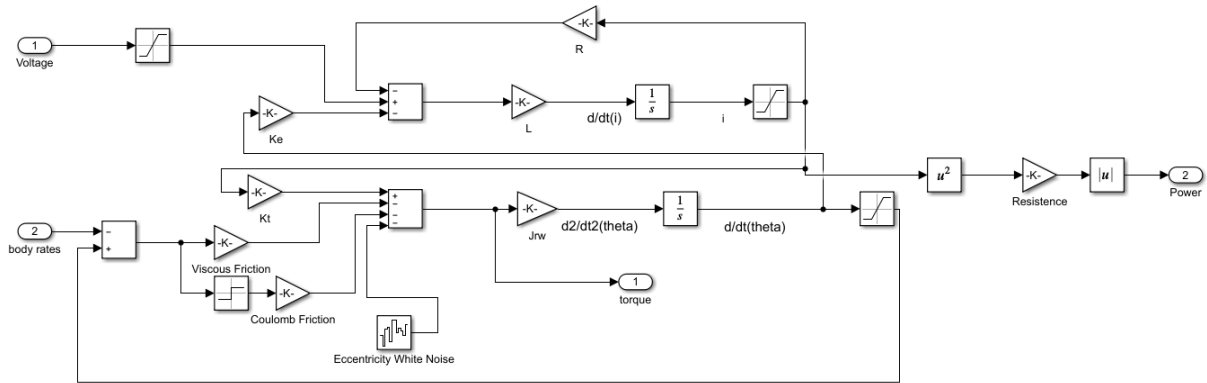
Figure 4.19: BLDC motor driver

The power consumption is calculated as:

$$P = R_a I_a^2$$ (4.94)

Reaction Wheel Motor Control
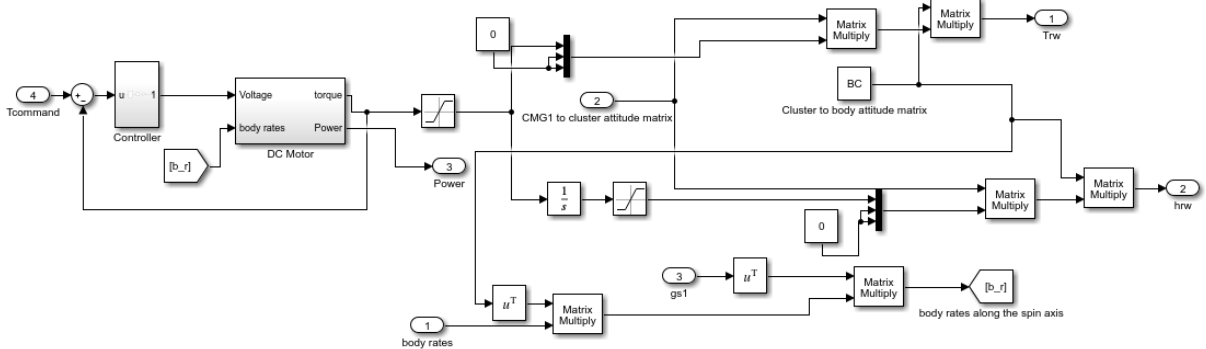
Figure 4.20: Reaction wheel with motor driver and motor driver controller

The motor driver of reaction wheels typically accept a torque command [10, 22], as seen in figure 4.20. A proportional integral derivative controller was developed for this effect. The parameters of the developed controller can always be altered by the user in order to obtain results that better suit the particular case.

Both the time response to a step input and the saturation of a single reaction wheel are presented in figure 4.21. Details regarding this analysis can be found in annex B.1.
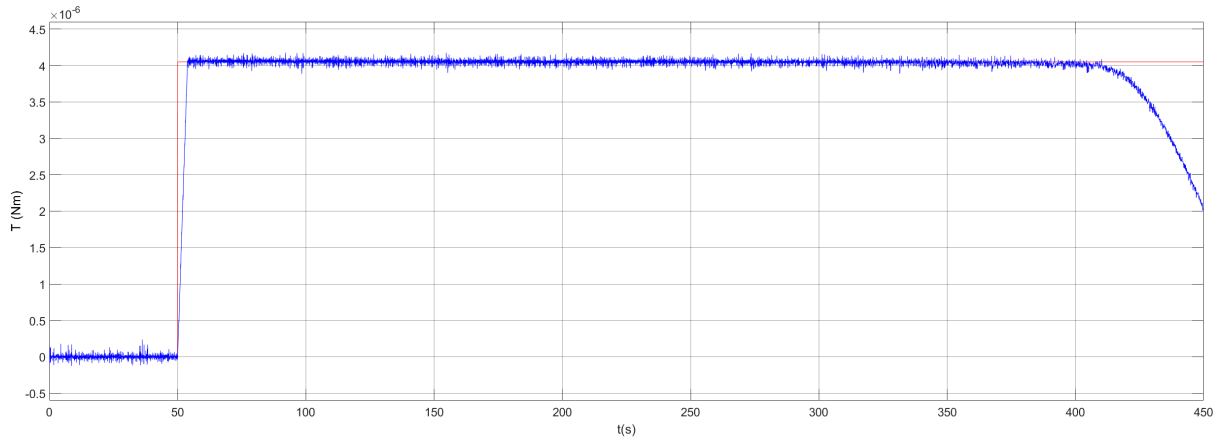
Figure 4.21: Time response to a step input and saturation of the reaction wheel

As a response to a $4 \times 10^{-6} Nm$ step input in the reaction wheel reference frame, the steady state is achieved under $5s$ and saturation occurs after $360s$.

4.7.2 Single Gimbal Control Moment Gyro model

To better understand the behavior of a cluster of single gimbal control moment gyros it is important to introduce two reference frames.
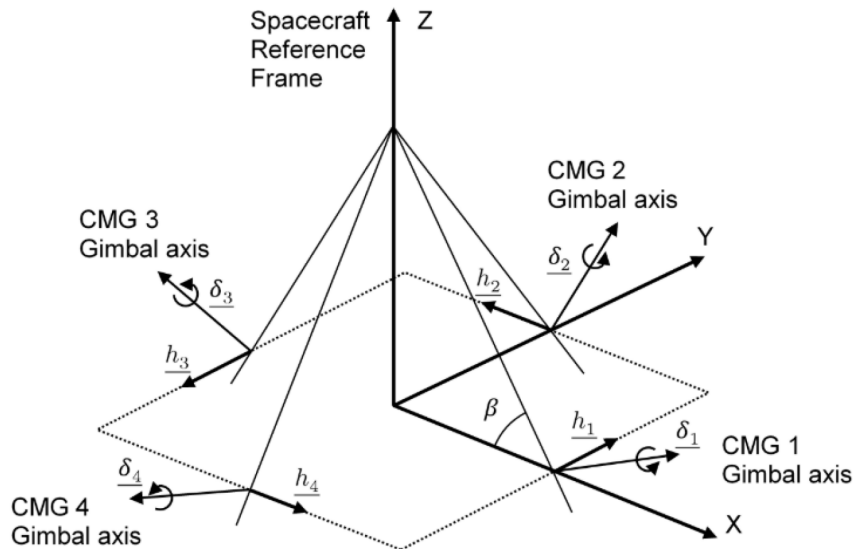
Figure 4.22: Cluster of four SGCMG in pyramid configuration [16]

- **CMG reference frame:** given by the triad of unit vectors $\{\hat{\mathbf{g}}_{\mathbf{s}}, \hat{\mathbf{g}}_{\mathbf{t}}, \hat{\mathbf{g}}_{\mathbf{g}}\}$. $\hat{\mathbf{g}}_{\mathbf{s}}$ is a vector in the direction of spin of the spinning wheel (direction of the angular momentum of the spinning wheel), $\hat{\mathbf{g}}_{\mathbf{g}}$ has the direction of the gimbal axis and $\hat{\mathbf{g}}_{\mathbf{t}}$ completes the right hand triad. Out of this three unit vectors,

only $\hat{\mathbf{g}}_{\mathbf{g}}$ is constant in time. Given an initial gimbal angle δ_0 [12]:

$$\hat{\mathbf{g}}_{\mathbf{s}}(t) = \cos(\delta(t) - \delta_0)\hat{\mathbf{g}}_{\mathbf{s}}(t_0) + \sin(\delta(t) - \delta_0)\hat{\mathbf{g}}_{\mathbf{t}}(t_0) \tag{4.95}$$

$$\hat{\mathbf{g}}_{\mathbf{t}}(t) = -\sin(\delta(t) - \delta_0)\hat{\mathbf{g}}_{\mathbf{s}}(t_0) + \cos(\delta(t) - \delta_0)\hat{\mathbf{g}}_{\mathbf{t}}(t_0) \tag{4.96}$$

- **Cluster reference frame:** represented in figure 4.22 by the axes X, Y, Z, provides a common reference frame for all the CMGs in the cluster. Contrary to the CMG reference frame, the cluster reference frame is constant in time and can be easily related to the body reference frame through a constant attitude matrix. It relates to the individual CMG reference frames through the current gimbal angle and constant shape parameters.

Typical CMG clusters are constituted by equal individual CMG.

$$\mathbf{h} = \sum_{i=1}^{N} \mathbf{h_i} \tag{4.97}$$

where $\mathbf{h_i}$ ($i = 1, ..n$ where n is the number of CMGs of the cluster) is given by [9]:

$$\mathbf{h_i} = \mathbf{h_i^f} + \mathbf{h_i^g} = h_i^f \hat{\mathbf{g}}_{\mathbf{si}} + h_i^g \hat{\mathbf{g}}_{\mathbf{gi}} = \mathbf{J_i^f} \boldsymbol{\omega_i^f} + \mathbf{J_i^g} \dot{\boldsymbol{\delta}_i} = \mathbf{J_i^f} \omega_i^f \hat{\mathbf{g}}_{\mathbf{si}} + \mathbf{J_i^g} \dot{\delta}_i \hat{\mathbf{g}}_{\mathbf{gi}} \tag{4.98}$$

where $\mathbf{J_i^f}$ and $\mathbf{J_i^g}$ represent the inertia of the flywheel (spinning disk) and the gimbal, respectivelly and $\mathbf{h_i^f}$ and $\mathbf{h_i^g}$ represent the angular momentum of the flywheel and gimbal. $\hat{\mathbf{g}}_{\mathbf{si}}$ and $\hat{\mathbf{g}}_{\mathbf{gi}}$ are the spin and gimbal axis.

Substituting in (2.33), the torque acting on the system can be obtained as:

$$\frac{d\mathbf{h_i}}{dt} = \mathbf{J_i^f} \dot{\omega}_i^f \hat{\mathbf{g}}_{\mathbf{si}} + \mathbf{J_i^f} \omega_i^f \dot{\hat{\mathbf{g}}}_{\mathbf{si}} + \mathbf{J_i^g} \ddot{\delta}_i \hat{\mathbf{g}}_{\mathbf{gi}} = \mathbf{J_i^f} \dot{\omega}_i^f \hat{\mathbf{g}}_{\mathbf{si}} + \dot{\delta}_i \mathbf{J_i^f} \omega_i^f \hat{\mathbf{g}}_{\mathbf{ti}} + \mathbf{J_i^g} \ddot{\delta}_i \hat{\mathbf{g}}_{\mathbf{gi}} \tag{4.99}$$

$$\frac{d\mathbf{h_i}}{dt} = \mathbf{J_i^f} \dot{\boldsymbol{\omega}}_i^f + \mathbf{J_i^g} \ddot{\boldsymbol{\delta}}_i + \dot{\boldsymbol{\delta}}_i \times (\mathbf{J_i^f} \boldsymbol{\omega}_i^f) = \boldsymbol{\tau}_i^d \tag{4.100}$$

where $\mathbf{J_i^f} \dot{\boldsymbol{\omega}}_i^f$ is the torque due to the acceleration of the flywheel i, $\mathbf{J_i^g} \ddot{\boldsymbol{\delta}}_i$ is the torque due to the acceleration of the gimbal i, $\dot{\boldsymbol{\delta}}_i \times (\mathbf{J_i^f} \boldsymbol{\omega}_i^f)$ is the gyroscopic (control) torque of the CMG i and $\boldsymbol{\tau}^d$ is the total dynamic torque of the CMG i.

Contrary to the control (gyroscopic) torque, the torque caused by the accelerations of both flywheel and gimbal are undesirable. For small satellites, these torques are considerable and cannot be neglected.

Moreover, since real motors are subject to friction and other disturbances, as explored in subsection 4.7.1, the total torque acting on the spacecraft due to one CMG is:

$$\tau_i = \tau^{control} + \tau_i^{fa} + \tau_i^{ga} + \tau_i^{ff} + \tau_i^{gf} \tag{4.101}$$

τ_i^{ff} and τ_i^{gf} are the disturbance/friction torques experienced by the flywheel and the gimbal, respectively, and were modeled as a combination of viscous and Coulomb friction described in (4.92). The total

torque due to the cluster of N control moment gyros is:

$$\boldsymbol{\tau} = \sum_{i=1}^{N} \boldsymbol{\tau_i} \qquad (4.102)$$

Since each CMG of the cluster will possess its own individual reference and the direction of the axes of each CMG reference frame varies with time (except for $\hat{g}_g$), the definition of a cluster reference simplifies the computation of (4.86) and (4.102). The definition of these parameters in the cluster reference frame is dependent on the configuration. Table 4.3 presents the CMG reference frame axes in the cluster reference frame for the different configurations available in the actuator block. The definition of the torque and angular momentum vector in the cluster reference frame will be further explained for the pyramid configuration (figure 4.22), without loss of generality.

For a pyramid configuration equations (4.98) and (4.97) in the cluster reference frame are given by:

$$\mathbf{h_C^g} = \sum_{i=1}^{N} \mathbf{h_{iC}^g} = \mathbf{J_1^g} \dot{\delta}_1 \begin{bmatrix} \cos\beta \\ 0 \\ \sin\beta \end{bmatrix} + \mathbf{J_2^g} \dot{\delta}_2 \begin{bmatrix} 0 \\ \cos\beta \\ \sin\beta \end{bmatrix} + \mathbf{J_3^g} \dot{\delta}_3 \begin{bmatrix} -\cos\beta \\ 0 \\ \sin\beta \end{bmatrix} + \mathbf{J_4^g} \dot{\delta}_4 \begin{bmatrix} 0 \\ -\cos\beta \\ \sin\beta \end{bmatrix} \qquad (4.103)$$

$$\mathbf{h_C^f} = \sum_{i=1}^{N} \mathbf{h_{iC}^f} = h_1 \begin{bmatrix} -\cos\beta\sin\delta_1 \\ \cos\delta_1 \\ \sin\beta\sin\delta_1 \end{bmatrix} + h_2 \begin{bmatrix} -\cos\delta_2 \\ -\cos\beta\sin\delta_2 \\ \sin\beta\sin\delta_2 \end{bmatrix} + h_3 \begin{bmatrix} \cos\beta\sin\delta_3 \\ -\cos\delta_3 \\ \sin\beta\sin\delta_3 \end{bmatrix} + h_4 \begin{bmatrix} \cos\delta_4 \\ \cos\beta\sin\delta_4 \\ \sin\beta\sin\delta_4 \end{bmatrix} \qquad (4.104)$$

β is a constant parameter defined by the architecture. Typically, for pyramid architecture, $\beta = 54.73^o$ [53]. δ_i (with $i = 1, 2, ...n$ with n equal to the number of CMGs in the cluster) are the gimbal angles.

Normally, the individual CMGs are operating with the same flywheel nominal speed, that is, $h_1 = h_2 = h_3 = h_4 = ... = h_n = h$. For a cluster of CMG acting with the same angular momentum, h_{cmg}, (4.104) is reduced to:

$$\mathbf{h_C^f} = h_{cmg} \mathbf{A} \qquad (4.105)$$

where A is a $3 \times n$ matrix, n is the number of CMGs of the cluster, resulting by summing the directional matrices of each individual CMG axis. That is:

$$\mathbf{A} = \begin{bmatrix} \hat{\mathbf{g}}_{\mathbf{s1}} & \hat{\mathbf{g}}_{\mathbf{s2}} & .... & \hat{\mathbf{g}}_{\mathbf{sn}} \end{bmatrix} \qquad (4.106)$$

Substituting $\hat{\mathbf{g}}_{\mathbf{siC}}$ and $\hat{\mathbf{g}}_{\mathbf{giC}}$ according to table 4.3, the flywheel and gimbal acceleration components of

the torque in equation (4.99) can be analogously obtained in the cluster frame:

$$(\mathbf{J^g}\ddot{\boldsymbol{\delta}})_\mathbf{C} = \sum_{i=1}^{N}(\mathbf{J_i^g}\ddot{\delta_i})_\mathbf{C} = \mathbf{J_1^g}\ddot{\delta_1}\begin{bmatrix}\cos\beta\\0\\\sin\beta\end{bmatrix} + \mathbf{J_2^g}\ddot{\delta_2}\begin{bmatrix}0\\\cos\beta\\\sin\beta\end{bmatrix} + \mathbf{J_3^g}\ddot{\delta_3}\begin{bmatrix}-\cos\beta\\0\\\sin\beta\end{bmatrix}$$

$$+ \mathbf{J_4^g}\ddot{\delta_4}\begin{bmatrix}0\\-\cos\beta\\\sin\beta\end{bmatrix} \tag{4.107}$$

$$(\mathbf{J^f}\dot{\boldsymbol{\omega}}^f)_\mathbf{C} = \sum_{i=1}^{N}(\mathbf{J_i^f}\dot{\omega_i^f})_\mathbf{C} = \mathbf{J_1^f}\dot{\omega_1^f}\begin{bmatrix}-\cos\beta\sin\delta_1\\\cos\delta_1\\\sin\beta\sin\delta_1\end{bmatrix} + \mathbf{J_1^f}\dot{\omega_2^f}\begin{bmatrix}-\cos\delta_2\\-\cos\beta\sin\delta_2\\\sin\beta\sin\delta_2\end{bmatrix} + \mathbf{J_3^f}\dot{\omega_3^f}\begin{bmatrix}\cos\beta\sin\delta_3\\-\cos\delta_3\\\sin\beta\sin\delta_3\end{bmatrix}$$

$$+ \mathbf{J_4^f}\dot{\omega_4^f}\begin{bmatrix}\cos\delta_4\\\cos\beta\sin\delta_4\\\sin\beta\sin\delta_4\end{bmatrix} \tag{4.108}$$

Finally, the control torque can also be obtained in the pyramid cluster reference frame:

$$\tau_C^{control} = \sum_{i=1}^{N}\mathbf{J_i}(\delta_i)\dot{\delta_i} = h_1\begin{bmatrix}-\cos\beta\cos\delta_1\\-\sin\delta_1\\\sin\beta\cos\delta_1\end{bmatrix}\dot{\delta_1} + h_2\begin{bmatrix}\sin\delta_2\\-\cos\beta\cos\delta_2\\\sin\beta\cos\delta_2\end{bmatrix}\dot{\delta_2} + h_3\begin{bmatrix}\cos\beta\cos\delta_3\\\sin\delta_3\\\sin\beta\cos\delta_3\end{bmatrix}\dot{\delta_3}$$

$$+ h_4\begin{bmatrix}-\sin\delta_4\\\cos\beta\cos\delta_4\\\sin\beta\cos\delta_4\end{bmatrix}\dot{\delta_4} \tag{4.109}$$

For a cluster of CMG acting with the same angular momentum, (4.109) is reduced to:

$$\tau_C^{control} = \mathbf{J}(\delta)\dot{\boldsymbol{\delta}} \tag{4.110}$$

where $\mathbf{J}$ is the Jacobian Matrix:

$$\mathbf{J} = \frac{\partial \mathbf{h_C^f}}{\partial\delta} \tag{4.111}$$

For clusters where all CMGs have the same flywheel nominal angular momentum:

$$\mathbf{J} = h_{cmg}\frac{\partial\mathbf{A}}{\partial\delta} \tag{4.112}$$

Note that even though these results have been particularized for the pyramid cluster, analogous results can be obtained for the other architectures, by substituting the expressions in table 4.3 in each component of equations (4.98) and (4.100).

54

Table 4.3: CMG axes in cluster reference frame coordinates for different architectures

Architecture	No.CMG	$\hat{\mathbf{g}}_{\mathbf{s}}$	$\hat{\mathbf{g}}_{\mathbf{t}}$	$\hat{\mathbf{g}}_{\mathbf{g}}$
Single	1	$\hat{\mathbf{g}}_{\mathbf{s1}} = \begin{bmatrix} \cos\delta_1 \\ \sin\delta_1 \\ 0 \end{bmatrix}$	$\hat{\mathbf{g}}_{\mathbf{t1}} = \begin{bmatrix} -\sin\delta_1 \\ \cos\delta_1 \\ 0 \end{bmatrix}$	$\hat{\mathbf{g}}_{\mathbf{g1}} = \begin{bmatrix} 0 \\ 0 \\ 1 \end{bmatrix}$
Twin Scissored Pair [54]	2	$\hat{\mathbf{g}}_{\mathbf{s1}} = \begin{bmatrix} -\cos\delta_1 \\ \sin\delta_1 \\ 0 \end{bmatrix}$ $\hat{\mathbf{g}}_{\mathbf{s2}} = \begin{bmatrix} \cos\delta_2 \\ \sin\delta_2 \\ 0 \end{bmatrix}$	$\hat{\mathbf{g}}_{\mathbf{t1}} = \begin{bmatrix} \sin\delta_1 \\ \cos\delta_1 \\ 0 \end{bmatrix}$ $\hat{\mathbf{g}}_{\mathbf{t2}} = \begin{bmatrix} -\sin\delta_2 \\ \cos\delta_2 \\ 0 \end{bmatrix}$	$\hat{\mathbf{g}}_{\mathbf{g1}} = \begin{bmatrix} 0 \\ 0 \\ -1 \end{bmatrix}$ $\hat{\mathbf{g}}_{\mathbf{g2}} = \begin{bmatrix} 0 \\ 0 \\ 1 \end{bmatrix}$
Pyramid [16]	4	$\hat{\mathbf{g}}_{\mathbf{s1}} = \begin{bmatrix} -\cos\beta\sin\delta_1 \\ \cos\delta_1 \\ \sin\beta\sin\delta_1 \end{bmatrix}$ $\hat{\mathbf{g}}_{\mathbf{s2}} = \begin{bmatrix} -\cos\delta_2 \\ -\cos\beta\sin\delta_2 \\ \sin\beta\sin\delta_2 \end{bmatrix}$ $\hat{\mathbf{g}}_{\mathbf{s3}} = \begin{bmatrix} \cos\beta\sin\delta_3 \\ -\cos\delta_3 \\ \sin\beta\sin\delta_3 \end{bmatrix}$ $\hat{\mathbf{g}}_{\mathbf{s4}} = \begin{bmatrix} \cos\delta_4 \\ \cos\beta\sin\delta_4 \\ \sin\beta\sin\delta_4 \end{bmatrix}$	$\hat{\mathbf{g}}_{\mathbf{t1}} = \begin{bmatrix} -\cos\beta\cos\delta_1 \\ -\sin\delta_1 \\ \sin\beta\cos\delta_1 \end{bmatrix}$ $\hat{\mathbf{g}}_{\mathbf{t2}} = \begin{bmatrix} \sin\delta_2 \\ -\cos\beta\cos\delta_2 \\ \sin\beta\cos\delta_2 \end{bmatrix}$ $\hat{\mathbf{g}}_{\mathbf{t1}} = \begin{bmatrix} \cos\beta\cos\delta_3 \\ \sin\delta_3 \\ \sin\beta\cos\delta_3 \end{bmatrix}$ $\hat{\mathbf{g}}_{\mathbf{t2}} = \begin{bmatrix} -\sin\delta_4 \\ \cos\beta\cos\delta_4 \\ \sin\beta\cos\delta_4 \end{bmatrix}$	$\hat{\mathbf{g}}_{\mathbf{g1}} = \begin{bmatrix} \cos\beta \\ 0 \\ \sin\beta \end{bmatrix}$ $\hat{\mathbf{g}}_{\mathbf{g2}} = \begin{bmatrix} 0 \\ \cos\beta \\ \sin\beta \end{bmatrix}$ $\hat{\mathbf{g}}_{\mathbf{g3}} = \begin{bmatrix} -\cos\beta \\ 0 \\ \sin\beta \end{bmatrix}$ $\hat{\mathbf{g}}_{\mathbf{g4}} = \begin{bmatrix} 0 \\ -\cos\beta \\ \sin\beta \end{bmatrix}$
Box-90 [53]	4	$\hat{\mathbf{g}}_{\mathbf{s1}} = \begin{bmatrix} \cos\delta_1 \\ \sin\delta_1 \\ 0 \end{bmatrix}$ $\hat{\mathbf{g}}_{\mathbf{s2}} = \begin{bmatrix} \cos\delta_2 \\ \sin\delta_2 \\ 0 \end{bmatrix}$ $\hat{\mathbf{g}}_{\mathbf{s3}} = \begin{bmatrix} \cos\delta_3 \\ 0 \\ \sin\delta_3 \end{bmatrix}$ $\hat{\mathbf{g}}_{\mathbf{s4}} = \begin{bmatrix} \cos\delta_4 \\ 0 \\ \sin\delta_4 \end{bmatrix}$	$\hat{\mathbf{g}}_{\mathbf{t1}} = \begin{bmatrix} -\sin\delta_1 \\ \cos\delta_1 \\ 0 \end{bmatrix}$ $\hat{\mathbf{g}}_{\mathbf{t2}} = \begin{bmatrix} -\sin\delta_2 \\ \cos\delta_2 \\ 0 \end{bmatrix}$ $\hat{\mathbf{g}}_{\mathbf{t3}} = \begin{bmatrix} -\sin\delta_3 \\ 0 \\ \cos\delta_3 \end{bmatrix}$ $\hat{\mathbf{g}}_{\mathbf{t4}} = \begin{bmatrix} -\sin\delta_4 \\ 0 \\ \cos\delta_4 \end{bmatrix}$	$\hat{\mathbf{g}}_{\mathbf{g1}} = \begin{bmatrix} 0 \\ 0 \\ 1 \end{bmatrix}$ $\hat{\mathbf{g}}_{\mathbf{g2}} = \begin{bmatrix} 0 \\ 0 \\ 1 \end{bmatrix}$ $\hat{\mathbf{g}}_{\mathbf{t1}} = \begin{bmatrix} 0 \\ -1 \\ 0 \end{bmatrix}$ $\hat{\mathbf{g}}_{\mathbf{t2}} = \begin{bmatrix} 0 \\ -1 \\ 0 \end{bmatrix}$

Finally, the net angular momentum and torque vectors can be obtained in the body frame as:

$$\mathbf{h_B} = \mathbf{A_{BC}}\mathbf{h_C} \tag{4.113}$$

$$\tau_B = \mathbf{A_{BC}} \tau_C \tag{4.114}$$

where $\mathbf{A_{BC}}$ is the rotation matrix that transforms a vector in the cluster coordinate frame in the same vector in the body frame.

The CMG structure was modeled as a momentum wheel spun up to a nominal speed, in appendix B.2, (whose motor driver and motor driver control follow the model developed in [46] and can be seen in appendix B.2) whose spin axis direction rotates about a gimbal direction. The gimbal of the CMG is driven by a BLDC motor similar to the one explained in 4.7.1.

A big disadvantage of CMGs is that singularities may arise for certain values of $\mathbf{J}$. A singular state is defined as the range of gimbal angles for which the CMG system is not able to generate torque along a desired direction.

For a redundant system of four CMGs (for example, a pyramid or Box-90 configurations) this occurs when the rank of the Jacobian matrix is lower than three. In order to have 3-axis control the rank of the Jacobian matrix must be three, and the minimal rank is two because the gimbal axes are not positioned co-planar [54]. Internal singularities can be partially or totally avoided by employing the correct steering laws.

Steering Law

Contrary to reaction wheels, most CMG do not receive the motor torque as a control input but rather, the gimbal angle rate as a control input [12]. This fact makes the existence of a steering law algorithm necessary. Steering laws can also be used to avoid or pass some singular configurations of the control momentum gyro. The typical feedback loop of a control moment gyro is presented in figure 4.23.
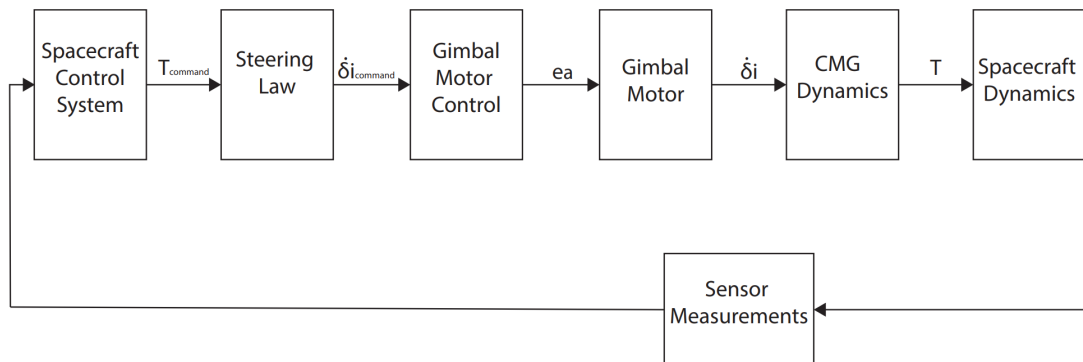
Figure 4.23: CMG control loop

The current Simulink actuator block presents three different options of steering laws: pseudo-inverse steering law, singularity avoidance steering law [55] and singularity passing steering law [54].

Pseudo-inverse steering law This law simply computes the desired gimbal rates from the commanded torque by multiplying both sides of (4.110) by the inverse of the Jacobian, $\mathbf{J}(\delta)$. Because

isn't necessarily a square matrix, the Moore Penrose $\mathbf{J}(\delta)^\star$ pseudo-inverse is used instead:

$$\mathbf{J}(\delta)^\star = \mathbf{J}(\delta)^T [\mathbf{J}(\delta)\mathbf{J}(\delta)^T]^{-1} \tag{4.115}$$

Therefore, the commanded gimbal rates are given by:

$$\dot{\boldsymbol{\delta}} = \mathbf{J}(\delta)^\star \dot{\boldsymbol{h}}_C^{command} \tag{4.116}$$

The Moore-Penrose pseudo-inverse is valid for all CMG configurations and it's the default steering law of the Box-90 architecture of the commercially available Microsat CMG by Honeybee Robotics [6]. Nevertheless, this steering law does not grant protection against singularities.

Singularity robust inverse law The singularity robust inverse law is part of the singularity avoidance category. As suggested, steering laws from this group solve the singularity problem by completely avoiding singular states. The singularity robust inverse law avoids singularities by introducing small torque errors when the CMG cluster is near singular configurations. The closeness to a singularity evaluated by the parameter m [55]:

$$m = \sqrt{\det\left[\mathbf{J}(\delta)\mathbf{J}(\delta)^T\right]} \tag{4.117}$$

And the commanded gimbal rates are given by:

$$\dot{\boldsymbol{\delta}} = \mathbf{J}(\delta)^T [\mathbf{J}(\delta)\mathbf{J}(\delta)^T + k\mathbf{I}]^{-1} \dot{\boldsymbol{h}}_C^{command} \tag{4.118}$$

with k given by:

$$\begin{cases} k = 0, & m > m_{cr} \\ k = \frac{k_0}{m}, & m < m_{cr} \text{ and } \frac{k_0}{m} < k_{max} \\ k = k_{max}, & m < m_{cr} \text{ and } \frac{k_0}{m} > k_{max} \end{cases} \tag{4.119}$$

where k is the torque error introduced for values of m smaller than a critical threshold, $m < m_{cr}$. k_{max} is the maximum error introduced and k_0 is a constant that correlates the size of the torque error introduced to the proximity to a singularity state.

The singularity robust inverse law has been showed in [55] to be successful in avoiding singularities for redundant configurations (more than three CMG). This is not an effective method to avoid singularities for scissored pairs of control moment gyros.

Singularity passing steering law The singularity robust steering law is not effective in avoiding singularities for non-redundant configurations such as singular or 2-CMG scissored pair architectures, so

a singularity escaping steering law was used as an alternative for this architecture. This steering law is a modified version of the modified singularity robust [56] developed in [54]. In which the inverse is calculated as:

$$\mathbf{J}(\delta)^{\#} = \mathbf{W}\mathbf{J}(\delta)^{T}[\mathbf{J}(\delta)\mathbf{W}\mathbf{J}(\delta)^{T} + k\mathbf{\Phi}]^{-1} \tag{4.120}$$

Note that, despite offering protection against singularities, this steering law normally introduces a bigger torque error.

For 2-CMG scissored pair architectures a different parameterization is useful for steering law purposes [54]. Table 4.4 summarizes the parameters δ, A, J and $\dot{h}_C^{command}$ used for steering law purposes in different architectures.

Table 4.4: Steering law parameters for different architectures

Architecture	δ	A	J	$\dot{h}_C^{command}$
Single	δ_1	$\begin{bmatrix} \cos\delta_1 \\ \sin\delta_1 \end{bmatrix}$	$\begin{bmatrix} -\sin\delta_1 \\ \cos\delta_1 \end{bmatrix}$	$\begin{bmatrix} \tau_x \\ \tau_y \end{bmatrix}$
Twin Scissored Pair [54]	$\begin{bmatrix} \alpha \\ \gamma \end{bmatrix}$, where $\alpha = \frac{\pi - \delta_1 + \delta_2}{2}$ and $\gamma = \frac{\pi - \delta_1 - \delta_2}{2}$	$2\begin{bmatrix} \cos\alpha\cos\gamma \\ \sin\alpha\cos\gamma \end{bmatrix}$	$2\begin{bmatrix} -\sin\alpha\cos\gamma & -\cos\alpha\sin\gamma \\ \cos\alpha\cos\gamma & -\sin\alpha\sin\gamma \end{bmatrix}$	$\begin{bmatrix} \tau_x \\ \tau_y \end{bmatrix}$
Pyramid [16]	$\begin{bmatrix} \delta_1 \\ \delta_2 \\ \delta_3 \\ \delta_4 \end{bmatrix}$	$\begin{bmatrix} -c\beta s\delta_1 & -c\delta_2 & c\beta s\delta_3 & c\delta_4 \\ c\delta_1 & -c\beta s\delta_2 & -c\delta_3 & c\beta s\delta_4 \\ s\beta s\delta_1 & s\beta s\delta_2 & s\beta s\delta_3 & s\beta s\delta_4 \end{bmatrix}$	$\begin{bmatrix} -c\beta c\delta_1 & s\delta_2 & c\beta c\delta_3 & -s\delta_4 \\ -s\delta_1 & -c\beta c\delta_2 & s\delta_3 & c\beta c\delta_4 \\ s\beta c\delta_1 & s\beta c\delta_2 & s\beta c\delta_3 & s\beta c\delta_4 \end{bmatrix}$	$\begin{bmatrix} \tau_x \\ \tau_y \\ \tau_z \end{bmatrix}$
Box-90 [53]	$\begin{bmatrix} \delta_1 \\ \delta_2 \\ \delta_3 \\ \delta_4 \end{bmatrix}$	$\begin{bmatrix} c\delta_1 & c\delta_2 & c\delta_3 & c\delta_4 \\ s\delta_1 & s\delta_2 & 0 & 0 \\ 0 & 0 & s\delta_3 & s\delta_4 \end{bmatrix}$	$\begin{bmatrix} -s\delta_1 & -s\delta_2 & -s\delta_3 & -s\delta_4 \\ c\delta_1 & c\delta_2 & 0 & 0 \\ 0 & 0 & c\delta_3 & c\delta_4 \end{bmatrix}$	$\begin{bmatrix} \tau_x \\ \tau_y \\ \tau_z \end{bmatrix}$

The steering laws available in the actuator block for each architecture are presented in table B.4

Table 4.5: Steering laws available in the actuator block [10]

Architecture	Moore Penrose pseudo-inverse	Singularity robust inverse	Singularity passing inverse
Single	×		
Twin Scissored Pair	×		×
Pyramid	×	×	
Box-90	×	×	

Gimbal Motor Control

Contrary to the CMGs flywheel motor, which similarly to momentum wheels are normally spun up to their maximum speed and kept at a nominal angular momentum equal to their maximum momentum storage, the gimbal motor drives of reaction wheels typically accept a speed command, as seen in figure 4.24.
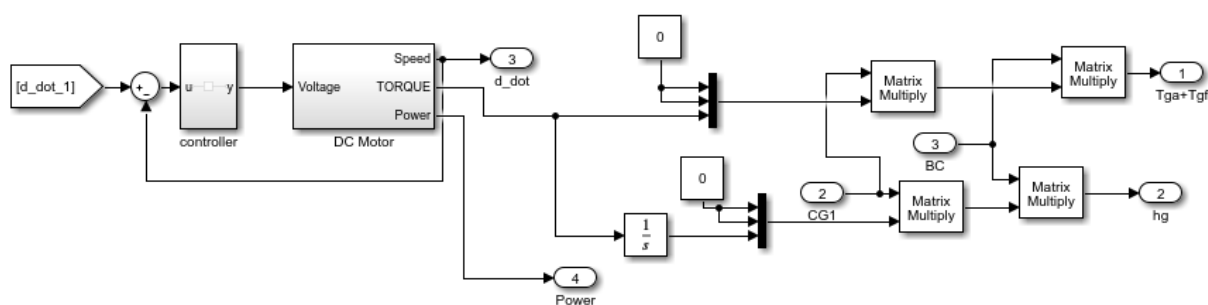
Figure 4.24: Gimbal with motor drive and motor drive controller

A linear quadratic regulator controller (LQR) was designed for this purpose.

Linear Quadratic Regulator (LQR)

Neglecting the contributions of Coloumb friction and eccentricity disturbances, equations (4.90) and (4.91) can be written in matrix form as:

$$\begin{bmatrix} \dot{i}_a \\ \dot{\omega}_m \end{bmatrix} = \begin{bmatrix} -R_a/L_a & -K_b/L_a \\ K_i/J & -B_m/J \end{bmatrix} \begin{bmatrix} i_a \\ \omega_m \end{bmatrix} + \begin{bmatrix} 1/L_a \\ 0 \end{bmatrix} e_a \qquad (4.121)$$

From (4.121) it is trivial that a possible state-space representation of the BLDC motor is:

$$\dot{\mathbf{x}} = \mathbf{A}\mathbf{x} + \mathbf{B}u \qquad (4.122)$$

with

$$x = \begin{bmatrix} i_a \\ \omega_m \end{bmatrix} \quad (4.123) \qquad \mathbf{A} = \begin{bmatrix} -R_a/L_a & -K_b/L_a \\ K_i/J & -B_m/J \end{bmatrix} \quad (4.124)$$

$$\mathbf{B} = \begin{bmatrix} 1/L_a \\ 0 \end{bmatrix} \quad (4.125) \qquad\qquad u = e_a \quad (4.126)$$

The feedback controller

$$u = -\mathbf{Kx} \tag{4.127}$$

is going to be designed in order to minimize the performance index

$$J = \int_0^\infty (\mathbf{x}^T \mathbf{Q} \mathbf{x} + \mathbf{R} \mathbf{u}^2) \tag{4.128}$$

where $\mathbf{Q}$ is a positive semi-definite matrix and $\mathbf{R}$ is a positive definite matrix. The cost function (4.128) is minimized for an optimal feedback control gain:

$$\mathbf{K} = \mathbf{R}^{-1} \mathbf{B}^T \mathbf{P} \tag{4.129}$$

For a symmetric positive definite matrix $\mathbf{P}$, defined by the solution off the algebraic Ricatti equation:

$$\mathbf{A}^T \mathbf{P} + \mathbf{P} \mathbf{A} - \mathbf{P} \mathbf{B} \mathbf{R}^{-1} \mathbf{B}^T \mathbf{P} + \mathbf{Q} = 0 \tag{4.130}$$

4.8 Attitude Control

This block contains both an OBC controller and actuator controllers.

The OBC controller consists of a set of conditional *if* statements that determine the operational pointing mode (nadir pointing, sun pointing or detumble) of the on board computer. This controller is also responsible for toggling actuators such as momentum exchange devices, switching the on-board computer propagator on and off as well as commanding the performance of the reset of its value with periodic GPS measurements. Finally, it determines when should determination algorithms be used for attitude determination and when is the attitude considered to be acquired.

The set of available controllers can be divided into detumbling and nominal pointing algorithms. The actuator block is equipped with 4 detumbling algorithms developed in [46], that will not be further explained in this work, as well as two nominal pointing algorithms: a constant gain linear quadratic regulator developed by [57] and a feedback controller for CMG equipped spacecrafts further detailed in subsection 4.8.1.

4.8.1 Feedback Controller for CMG

Since obtaining an optimal controller for a specific case wasn't the objective of this thesis, a generic feedback controller [58] was developed. Recall the dynamics equation:

$$\mathbf{J}\dot{\boldsymbol{\omega}} = -\boldsymbol{\omega} \times (\mathbf{J}\boldsymbol{\omega} + \mathbf{h}) - \boldsymbol{\tau}_{ext} - \dot{\mathbf{h}} \tag{4.131}$$

Where τ_{ext} is the net disturbance torque and h is the angular momentum of the control moment gyro cluster such that:

$$-\boldsymbol{\tau} = \boldsymbol{\omega} \times \mathbf{h} + \dot{\mathbf{h}} \tag{4.132}$$

A feedback control law was developed in [58] such that:

$$\boldsymbol{\tau}_{req} = -\mathbf{K_p}\mathbf{q}^{\mathbf{e}}_{1:3} - \mathbf{K_d}\boldsymbol{\omega}^e \tag{4.133}$$

Where τ_{req} stands for the requested torque, $\mathbf{q}^{\mathbf{e}}_{1:3}$ and ω^e are the quaternion and body-rate vector errors of the spacecraft:

$$\mathbf{q}^{\mathbf{e}} = \mathbf{q_{BI}} \otimes \mathbf{q}^{-1}_{\text{desired}} = \begin{bmatrix} \mathbf{q}^{\mathbf{e}}_{1:3} \\ q^e_4 \end{bmatrix} \tag{4.134}$$

$$\omega^e = \omega^{BI}_B - \omega^{desired}_B \tag{4.135}$$

Where $\mathbf{q_{BI}}$ and ω^{BI}_B describe the current attitude and body rates of the spacecraft and $\mathbf{q}^{-1}_{\text{desired}}$ and $\omega^{desired}_B$ refer to their desired values.

$\mathbf{K_p}$ and $\mathbf{K_d}$ are the gain matrices of the controller. The gain matrices can be determined with a Lyapunov stability analysis.

For a positive definite matrix $\mathbf{K_P}$:

$$V = \mathbf{K_p}[(q_4 - 1)^2 + \mathbf{q}^{\mathbf{T}}_{1:3}\mathbf{q}_{1:3}] + \frac{1}{2}\boldsymbol{\omega}^T\mathbf{J}\boldsymbol{\omega} \tag{4.136}$$

is a positive definite function. The derivative of this Lyapunov's candidate function is:

$$\dot{V} = \mathbf{K_p}[2(q_4 - 1)\dot{q}_4 + 2\mathbf{q}^{\mathbf{T}}_{1:3}\dot{\mathbf{q}}_{\mathbf{i}:3}] + \boldsymbol{\omega}^T\mathbf{J}\dot{\boldsymbol{\omega}} \tag{4.137}$$

Recall that:

$$\dot{q}_4 = -\frac{1}{2}\boldsymbol{\omega}^T\mathbf{q_{1:3}} \tag{4.138}$$

$$\dot{\mathbf{q}}_{\mathbf{1:3}} = \frac{1}{2}[\boldsymbol{\omega}\times]\mathbf{q}_{1:3} + \frac{1}{2}q_4\boldsymbol{\omega} \tag{4.139}$$

Substituting in 4.137:

$$\dot{V} = \mathbf{K_p}[-(q_4 - 1)\boldsymbol{\omega}^T\mathbf{q_{1:3}} + \mathbf{q}^{\mathbf{T}}_{1:3}([\boldsymbol{\omega}\times]\mathbf{q_{1:3}} + q_4\boldsymbol{\omega})] + \boldsymbol{\omega}^T\mathbf{J}\dot{\boldsymbol{\omega}} \tag{4.140}$$

Invoking the mathematical the following mathematical properties:

- The triple product of a vector with another and itself is null, that is, $\mathbf{a} \cdot (\mathbf{b} \times \mathbf{a}) = \mathbf{a} \cdot (\mathbf{a} \times \mathbf{b})$;

- Given two matrices A and B such that $A^T B$ is a scalar, than $B^T A$;

(4.140) can be reformulated as:

$$\dot{V} = \mathbf{K_p} \boldsymbol{\omega}^T \mathbf{q_{1:3}} + \boldsymbol{\omega}^T \mathbf{J} \dot{\boldsymbol{\omega}} \qquad (4.141)$$

Substituting (4.131) and (4.132) in (4.143):

$$\dot{V} = \mathbf{K_p} \boldsymbol{\omega}^T \mathbf{q_{1:3}} + \boldsymbol{\omega}^T \mathbf{J} \mathbf{J}^{-1} (-\boldsymbol{\omega} \times \mathbf{J}\boldsymbol{\omega} + \boldsymbol{\tau}) \qquad (4.142)$$

Resorting once again to the stated triple product and substituting (4.133) in (4.143):

$$\dot{V} = \mathbf{K_p} \boldsymbol{\omega}^T \mathbf{q_{1:3}} - \mathbf{K_p} \boldsymbol{\omega}^T \mathbf{q_{1:3}} - \mathbf{K_d} \boldsymbol{\omega}^T \boldsymbol{\omega} = -\mathbf{K_d} \boldsymbol{\omega}^T \boldsymbol{\omega} \qquad (4.143)$$

Since for any $\mathbf{x} \neq 0$, where $\mathbf{x} = \begin{bmatrix} \mathbf{q_{1:3}} & \boldsymbol{\omega} \end{bmatrix}^T$, $\boldsymbol{\omega}^T \boldsymbol{\omega} > 0$, for any positive definite $\mathbf{K_d}$, $\dot{V} < 0$. Therefore, for positive define gain matrices $\mathbf{K_d}$ and $\mathbf{K_p}$, the $\mathbf{x}$ shall be asymptotically stable.

CMG Controller Performance Analysis

As control moment gyros are complex devices, that involve several control structures, disturbance torques, as well as singularity configurations, the performance of the CMG controller was tested in a realistic scenario. Using the ORCASat spacecraft as the base, the both the magnetorquers and the momentum wheel of the spacecraft were substituted with a CMG pyramid configuration with parameters detailed in appendix B.2 and cluster frame parallel to the body frame.

Starting from the initial conditions (realistic conditions for the spacecraft after detumbling):

- $q_e = [0.0851; 0.0181; -0.0375; 1.0551]$

- $w_e = [2.041 \times 10^{-5}; -0.001; 3.57 \times 10^{-5}] rad/s$

The initial gimbal angles were also chosen to guarantee that a singular state occurs (figure 4.26) so as to test the singularity robust inverse steering law's ability to avoid singularities (details in appendix B.2):

- $\delta_1 = 0$

- $\delta_2 = 0$

- $\delta_3 = \pi$

- $\delta_4 = 0$

In an initial phase (first 500s) the satellite is commanded to point towards nadir. At 500s, the satellite is commanded to perform a rest-to-rest maneuver, of 30° around the pitch axis, and maintaining this attitude for the remaining time.

The objective of this maneuver was to test: the transitory response of the CMG immediately after being turned on, when the response is heavily influenced by the CMG, flywheel motor and gimbal motor controllers as well as increased disturbance torques due to the acceleration from rest of the gimbal and, mainly, the flywheel, the agility of the spacecraft after an initial stabilization and the steady state pointing error.
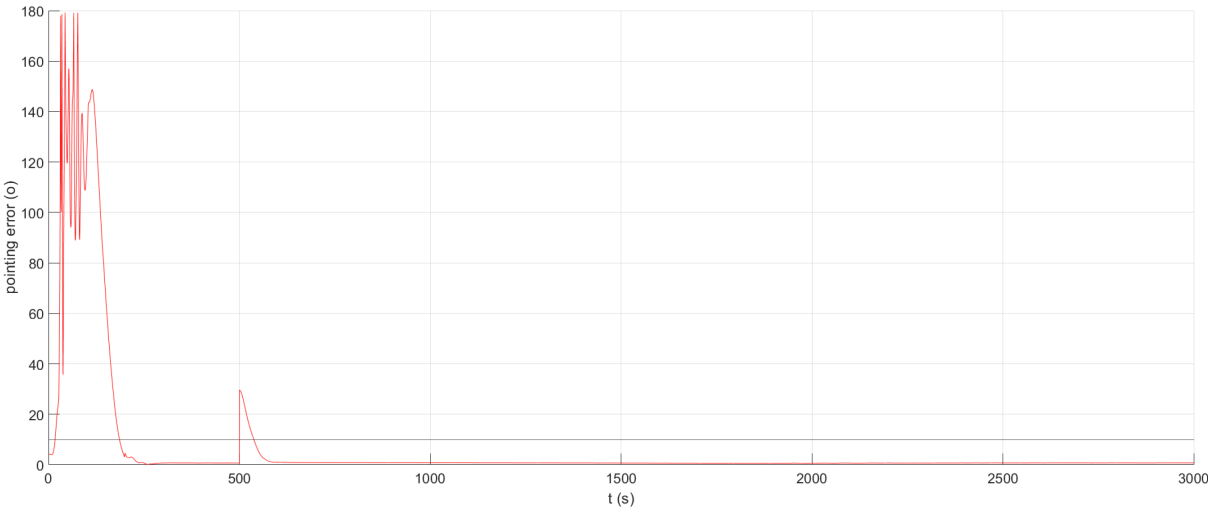
Figure 4.25: Pointing error

In figure 4.25, it is visible that immediately after being turned on, the CMG cluster torque causes the spacecraft to spin abnormally, causing the pointing error to spike. Despite undesirable, this result is expected as the disturbance torque necessary to accelerate one flywheel alone to its nominal speed can achieve a order of magnitude similar to the command torque. This erratic behavior is exacerbated by the control error introduced by the singularity robust inverse steering law when proximity to the singularity is detected at $t = 36s$.
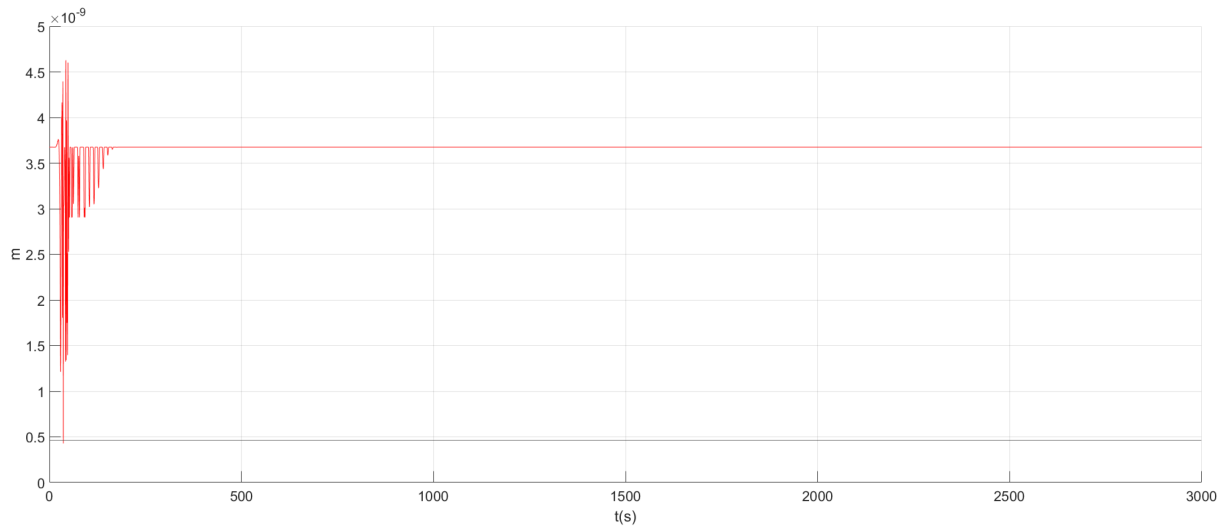
Figure 4.26: Index of proximity to a singular state m

Nevertheless, the controller manages to stabilize the motion of the spacecraft, regaining a pointing error lower than 10° in $186s$. When a new pointing direction is commanded at $500s$, the spacecraft managed to perform this maneuver smoothly achieving the ORCASats 10° pointing error requirement in $39s$ and a steady state error of approximately 0.7^o. Further results can be found in appendix B.2.

Chapter 5

Simulations and Results

In this chapter the ADCS solution selected for the ORCASat is going to be analyzed using the simulator tool. Section 5.1 summarizes ORCASat's ADCS solution and mission phases. In section 5.2 the impact of the initial conditions on the ADCS performance is analyzed. Section 5.3 studies the capability of achieving the ADCS requirements in case of failure of different sensors and actuators. Finally, section 5.4 compares ORCASat's ADCS solution with possible alternative solutions.

5.1   ORCASat's Mission and ADCS

5.1.1   ORCASat's ADCS

ORCASat utilizes a COTS solution by CubeSpace, visible in figure 5.1. This solution comprises a 3-axis Fluxgate Magnetometer, a 180° FOV CubeSense sun sensor with bore sight axis pointing towards $-\hat{b}_3$, aided by 10 photodiods, as well as a 3-Axis MEMS rate sensor (gyroscope). Regarding actuators, OrcaSat is equipped with 3-axis Magnetic torquers as well as CubeSpace's Y-axis CubeWheel Small momentum wheel. The commercial solution is complemented with CubeSpace's CubeComputer.
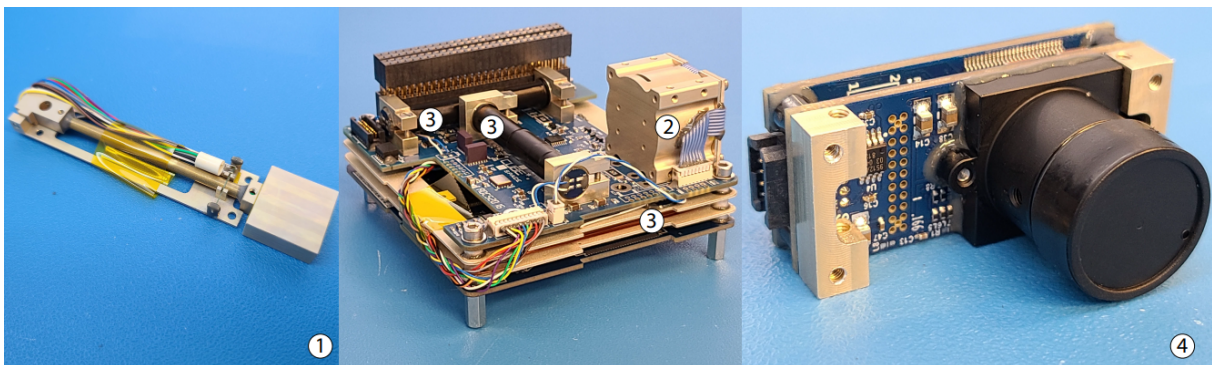
Figure 5.1: ORCASat's ADCS solution with visible magnetometer (1), momentum wheel (2), magnetorquers (3) and sun sensor (4)

As suggested in [46], the TRIAD algorithm makes use of the sun sensor and magnetometer measurements to initialize a AEKF. Finally, detumbling is achieved with a Fast detumbling B-dot algorithm purposed in [46]. In nominal mode, control is achieved via a constant gain LQR purposed in [20, 57].

5.1.2 ORCASat's Mission Phases

ORCASat's mission can be divided in the following sequential phases initiated by the OBC computer:

Table 5.1: ORCASat's ADCS mission phases

Phase	Start Condition	Description
Fast detumbling	$\omega \geq 0.15 rad/s$	Fast detumbling controller detumbles the spacecraft The wheel is turned off No attitude knowledge Body rates measured by the gyro
Wheel Toggling	$0.13 rad/s \geq \omega < 0.15 rad/s$	Fast detumbling controller detumbles the spacecraft The wheel is turned on No attitude knowledge Body rates measured by the gyro
OBC Propagator initialization	$0.11 rad/s \geq \omega < 0.13 rad/s$	Wheel toggling phase conditions are maintained The OBC propagator is toggled on The OBC starts computing orbit and attitude reference variables
Estimator Toggling	$0.02 rad/s \geq \omega < 0.11 rad/s$	The estimator is turned on Body rates are still given by the gyro measurement
Estimation Aquisition	$\omega < 0.02 rad/s$ $(\theta_e \geq 25^o \vee \dot{\theta}_e \geq 0.05 rad/s)$	Attitude given by the estimator Body rates given by the estimator Fast detumbling controller is still used to detumble the spacecraft
Nominal	$\omega < 0.02 rad/s$ $(\theta_e < 25^o \wedge \dot{\theta}_e < 0.05 rad/s)$	Attitude given by the estimator Body rates given by the estimator Magnetic dipole command given by the LQR

5.2 Initial Conditions

In order to compare the performance of different ADCS architectures in section 5.4 it was necessary to first study the impact of the chosen initial conditions in the pointing and estimation errors of the spacecraft. For that, the different realistic initial conditions in the base simulation scenario (table 5.2) were studied by changing their values one by one.

The impact of parameters whose real values can be well estimated (such as the orbital parameters), has been studied by introducing slight variations to their expected value (nominal value in table 5.2), whereas for parameters whose nominal value can not be predicted (such as initial orientation and angular rates), random values (drawn from the standard normal distribution) within a realistic range, were used.

Table 5.2: Base simulation conditions

Parameter	Value
Semimajor axis	$6768.24 km$
Eccentricity	0.00005
Inclination	51.64^o
Right ascension of the ascending node	117.76^o
Argument of the Perigee	34.8^o
Initial Mean Anomaly	60°
Initial quaternion orientation	$\begin{bmatrix} 1 & 0 & 0 & 0 \end{bmatrix}^T$
Initial angular rates	$\begin{bmatrix} 0.2 & 0.2 & 0.2 \end{bmatrix}^T$
Mass	$3.6 kg$
Inertia Matrix	$\begin{bmatrix} 0.003 & 0 & 0 \\ 0 & 0.007 & 0 \\ 0 & 0 & 0.008 \end{bmatrix} kgm^2$
Parasitic dipole moment	$\begin{bmatrix} 0.00707 & 0 & 0.00707 \end{bmatrix}^T Am^2$
Initial epoch	7pm, 1 January 2022

It has been shown that even though most initial conditions impact the detumbling time and the power consumption during detumble, these do not significantly impact the mission requirements for a realistic range of values (more results presented in appendix C). The exception is the initial body rates that seem to have an impact on the estimation error. As seen in figures 5.2 and 5.3 the estimation error depends on the initial angular rates. The 2° estimation error requirement is mostly satisfied, but can be locally unsatisfied for certain initial angular rates.
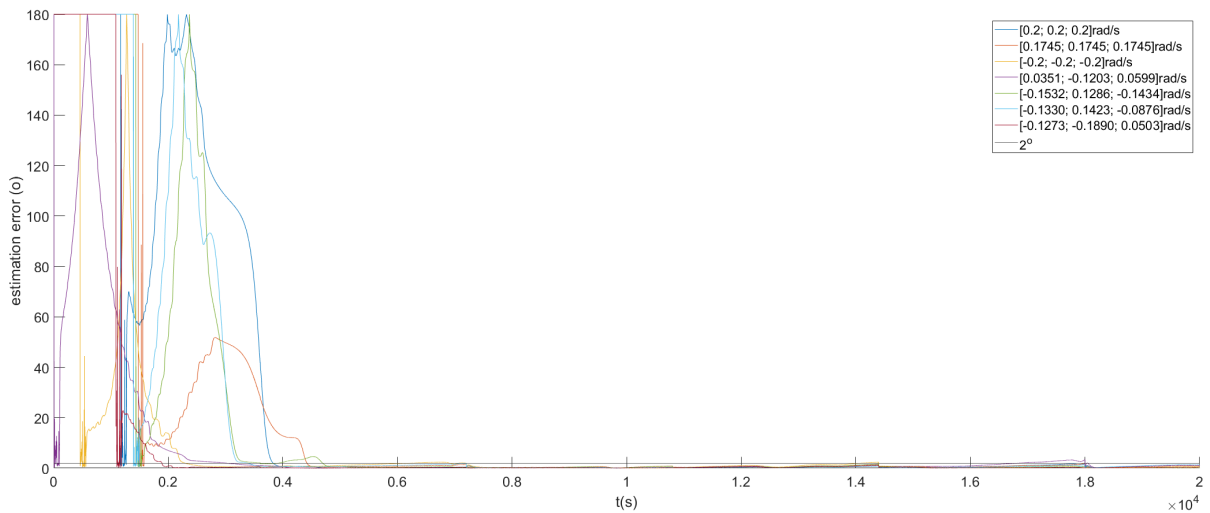
Figure 5.2: Estimation error for different initial angular rates
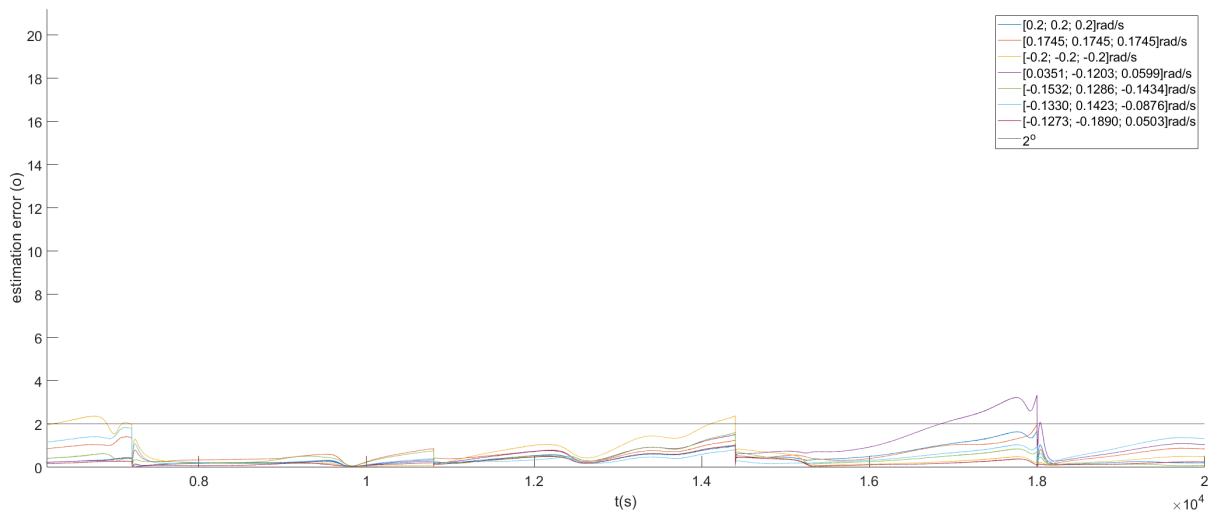
Figure 5.3: Estimation error for different initial angular rates: Detail view

It was therefore decided that in order to better study the estimation performance of different architectures, it would be necessary to analyze their performance for different initial body rates.

5.3 Failure of Sensors and Actuators

In this section the performance of ORCASat's ADCS solution is analyzed in case of failure of the different components.

5.3.1 Sun Sensor Failure

Two measurement vectors are necessary to execute the TRIAD algorithm, therefore, a sun sensor failure before the initialization of the EKF would prevent the TRIAD algorithm to obtain an initial attitude estimation. Nevertheless, multiple sensor measurements are not necessary to obtain an estimation of attitude and body rates with stochastic methods. Hence, a simulation was performed for the simulation base scenario where the sun sensor fails after initialization of the EKF. In this scenario, the update step of the EKF only takes into account magnetometer measurements.

68
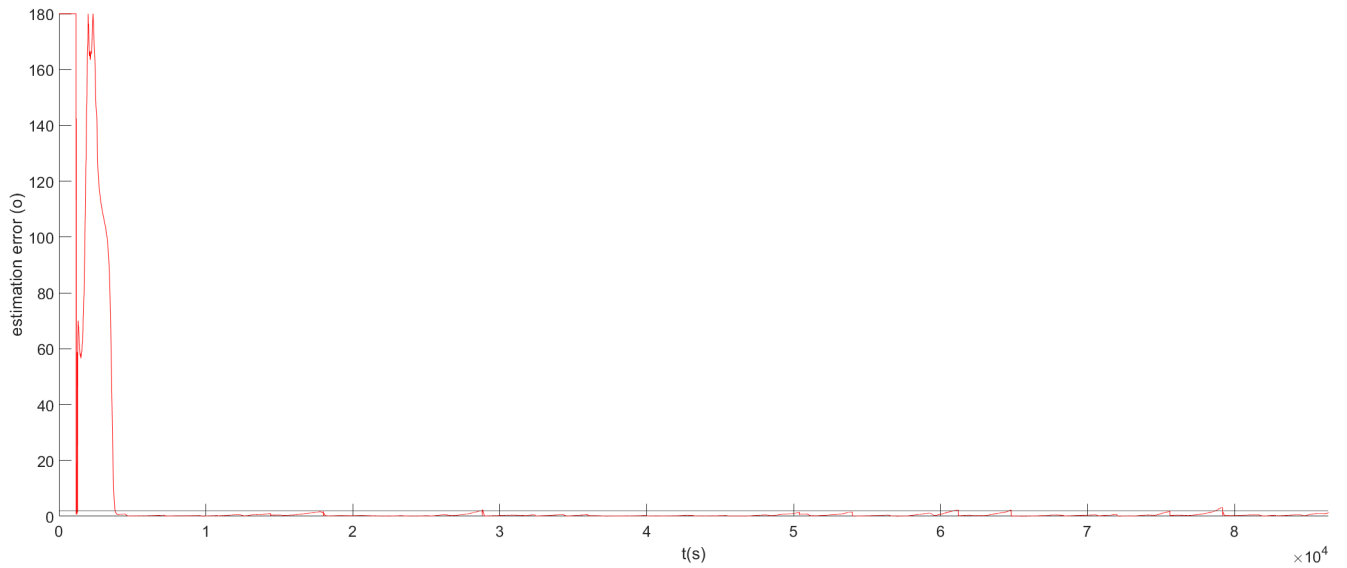
Figure 5.4: Estimation error in the event of sun sensor failure
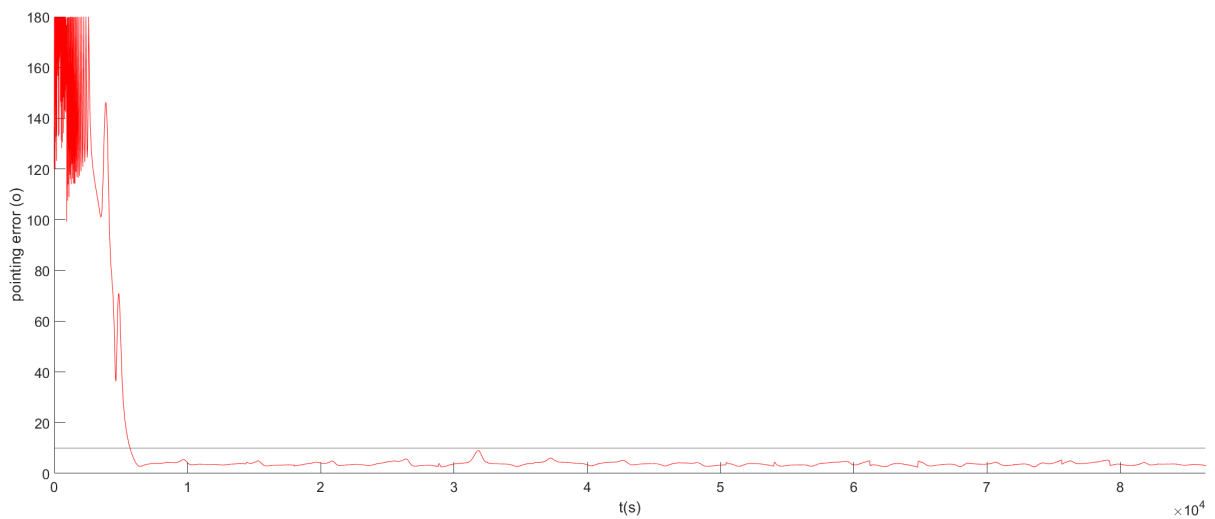
Figure 5.5: Pointing error in the event of sun sensor failure

As it can be seen in figures 5.4 and 5.5, the failure of the sun sensor does not seem to affect significantly the performance of the ADCS, as the 10° pointing error is globally satisfied and the 2° estimation error is mostly satisfied. The redundancy provided by the magnetometers seems to be enough to mostly achieve the mission requirements in case of sun sensor failure.

5.3.2 Magnetometer Failure

The measurement of the magnetic field is necessary not only to achieve attitude estimation but also as an input for both detumbling and LQR attitude controllers. After attitude knowledge has been ac-

quired the OBC computes an estimate of the magnetic field in the body frame (without need of magnetic measurement) that could potentially substitute the real measurement in the LQR controller in case of magnetometer failure. Nevertheless, the lack of a good attitude estimation before the nominal phase would prevent the spacecraft to detumble as previous to attitude acquisition, the OBC is not capable of performing this computation accurately.

The magnetometer failure in the nominal phase was simulated. In this case, after the attitude has been considered acquired, the magnetometer measurement becomes unavailable, that is, the update step of the EKF only takes into account the sun sensor measurement and the LQR starts using the OBC estimated magnetic field in the body reference as input.
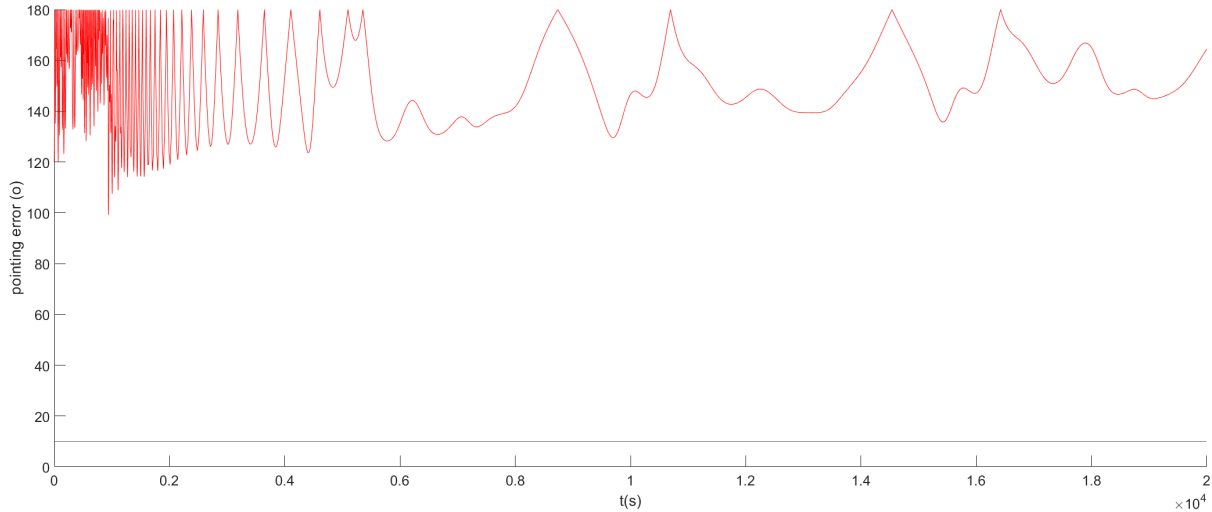
Figure 5.6: Pointing error in the event of magnetometer failure

As shown in figure 5.6, even during nominal phase a sun sensor failure could be fatal to the mission. This is mainly due to the long duration of eclipse phases during which the sun vector measurement is not available and the EKF is not capable of maintaining an accurate estimation relying only on the predict step.

5.3.3 Momentum Wheel Failure

The momentum wheel, with spin axis aligned with the $\hat{b}_2$ axis stabilizes the spacecraft by providing gyroscopic stiffness. Contrary to a magnetorquer failure, which would compromise the mission success, a momentum wheel failure may not affect significantly the mission requirements.
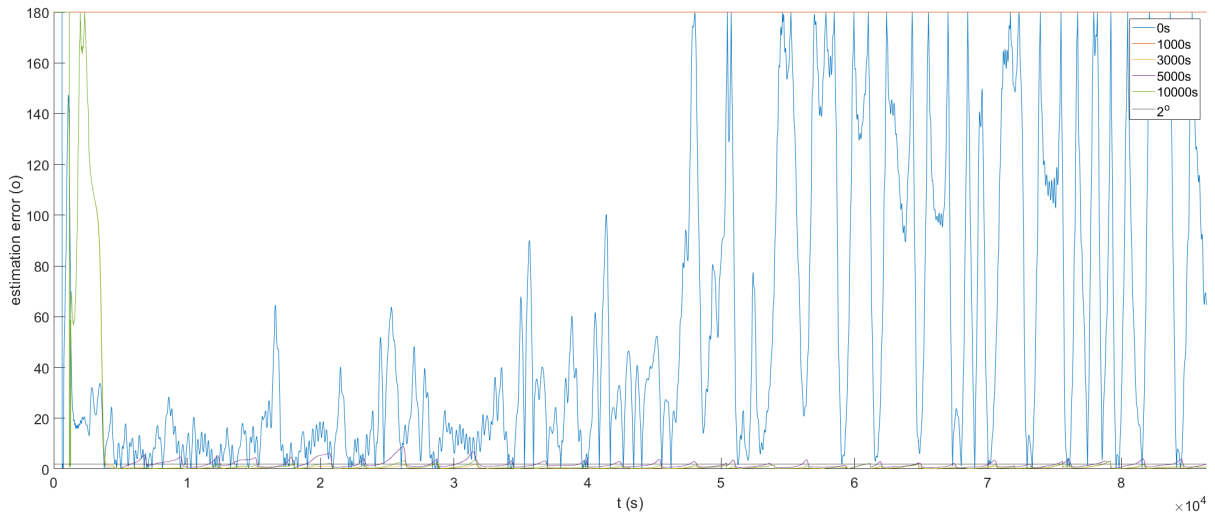
Figure 5.7: Estimation error in the event of momentum wheel failure in different mission phases
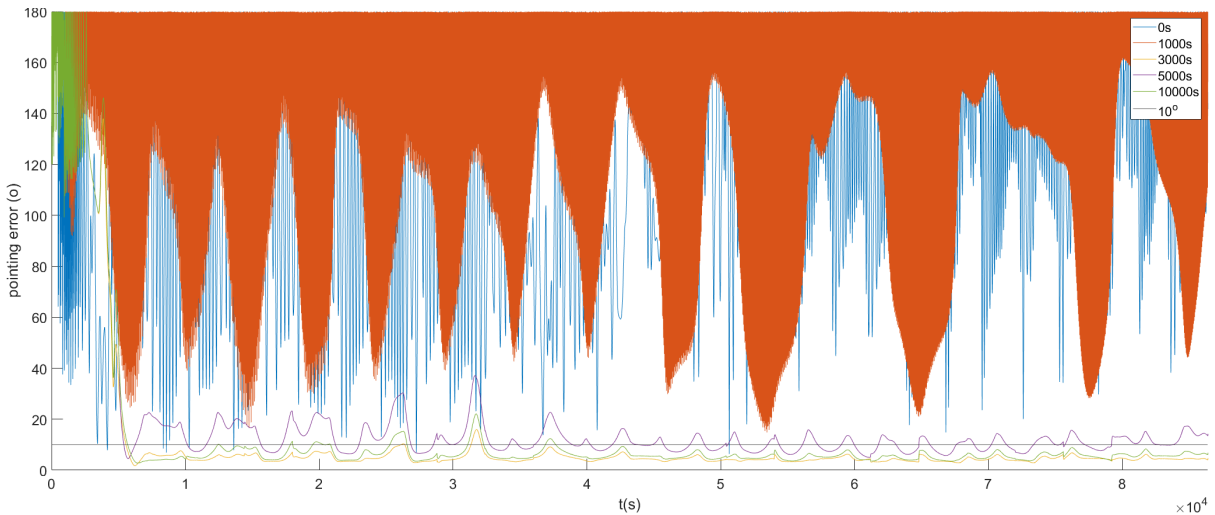
Figure 5.8: Pointing error in the event of momentum wheel failure in different mission phases

Figures 5.7 and 5.8 show that whether a momentum wheel failure is fatal to the mission or not depends on the instant in which it occurs. For errors occurring at 3000s and 10000s, pointing and estimation error requirements were mostly satisfied and the ADCS performance was not significantly affected, however, in all other cases, the mission has been severely compromised. It is not possible to establish a correlation between the mission phase/time of failure and the performance of the ADCS.

5.3.4 GPS failure

The OBC is equipped with a orbit and attitude propagator that is reset every hour by a GPS position and velocity measurement. This GPS measurement is also used to initialize the propagator. A GPS failure before the OBC propagator initialization phase is completed compromises the entire mission,

71

however, since the periodically resets only reduce the accumulation of errors in the OBC propagator, it was tested whether in the event of a failure of the GPS post this phase the mission requirements would still be satisfied.
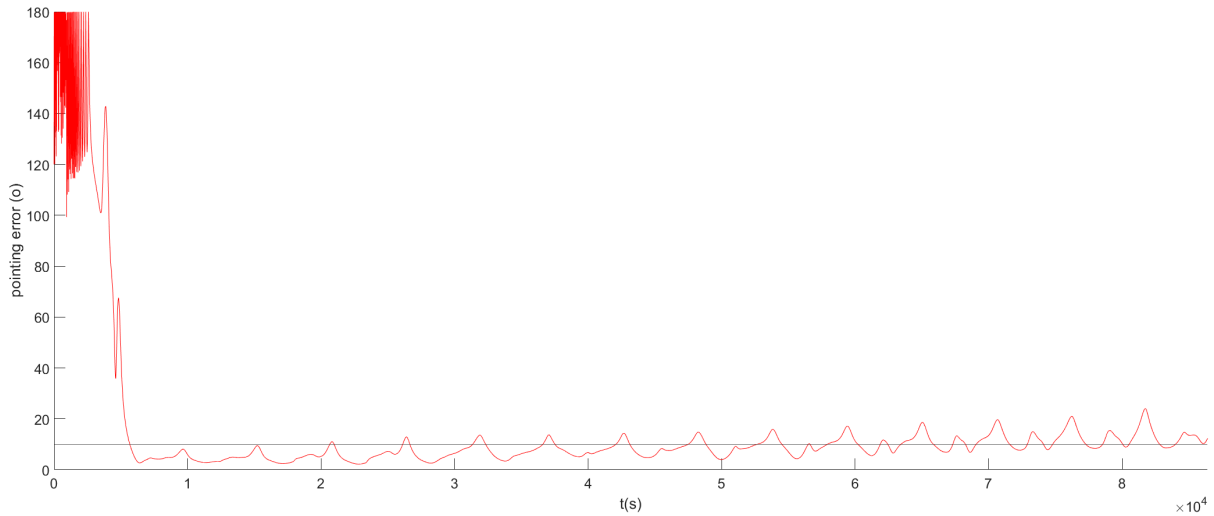
Figure 5.9: Pointing error in the event of GPS failure

Figure 5.9 shows that in case of GPS failure, despite pointing requirements being maintained in the first 3.5 orbits (19040s), on the long run, the accumulation of errors in the OBC propagator is enough to prevent the mission requirements from being satisfied.

5.4 Alternative Architectures

In this section, alternatives to the current ADCS solution for the ORCASat are studied. In subsection 5.4.1 alternatives to the sun sensor are tested whereas in subsection 5.4.2 a smaller, less powerful momentum wheel is tested as an alternative to CubeSpace's Cubewheel.

5.4.1 Sensor Alternatives

In sections 5.3.2 and 5.3.1 the cases of magnetometer and sun sensor failure have been studied. In these sections it has been shown that not only the mission requirements are mostly satisfied in case of sun sensor failure, but also, this sensor does not provide redundancy in case of magnetometer failure. This result lead to the study of two possible alternative architectures: one where the sun sensor is removed and the EKF algorithm is not initiated by the TRIAD algorithm, other, where the Cubesense sun sensor (aligned with the $-\hat{\mathbf{b}}_3$ axis) is replaced by the Cubesense nadir sensor (aligned with the $+\hat{\mathbf{b}}_3$ axis) as this sensor has the same mass and volume as the sun sensor version [33].

Since, as seen in section 5.2 the initial body rates affect the estimation error, each architecture was tested for 5 different ramdomly generated initial angular rates (the same 5 for each architecture). Table 5.3 summarizes the results obtained in terms of average steady state estimation and pointing error and

compares the different architectures in terms of mass. More detailed results can be found in appendix C.

Table 5.3: Different architectures comparison

Architecture	Mass difference	Mean estimation error	Mean pointing error
Sun sensor + Magnetometers	$0g$	0.54^o	3.8^o
Magnetometers	$-30g$	0.54^o	3.9^o
Earth sensor + Magnetometers	$0g$	0.80^o	4.1^o

Finally, for the solution equipped with a nadir sensor the redundancy capabilities of the solution in case of failure of the magnetometer in nominal phase where studied. A simulation similar to the one described in section 5.3.2 was conducted for this purpose. As seen in figures 5.10 and 5.11, even after magnetometer failure in the nominal phase of the mission, when equipped with a earth sensor instead of a sun sensor, the spacecraft is capable of achieving the mission requirements.
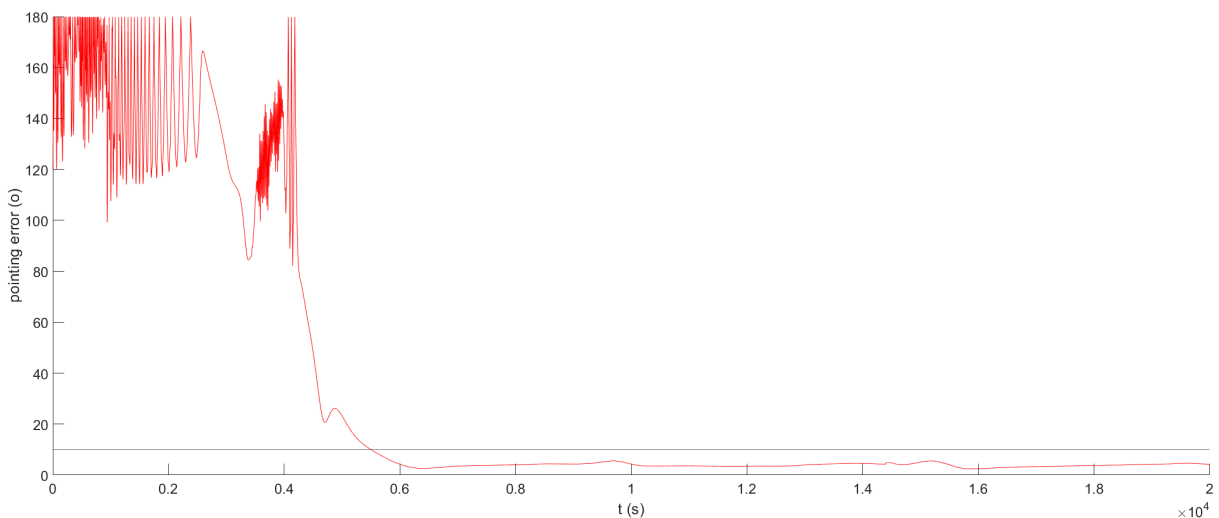
Figure 5.10: Pointing error in the event of magnetometer failure in nominal mission phase
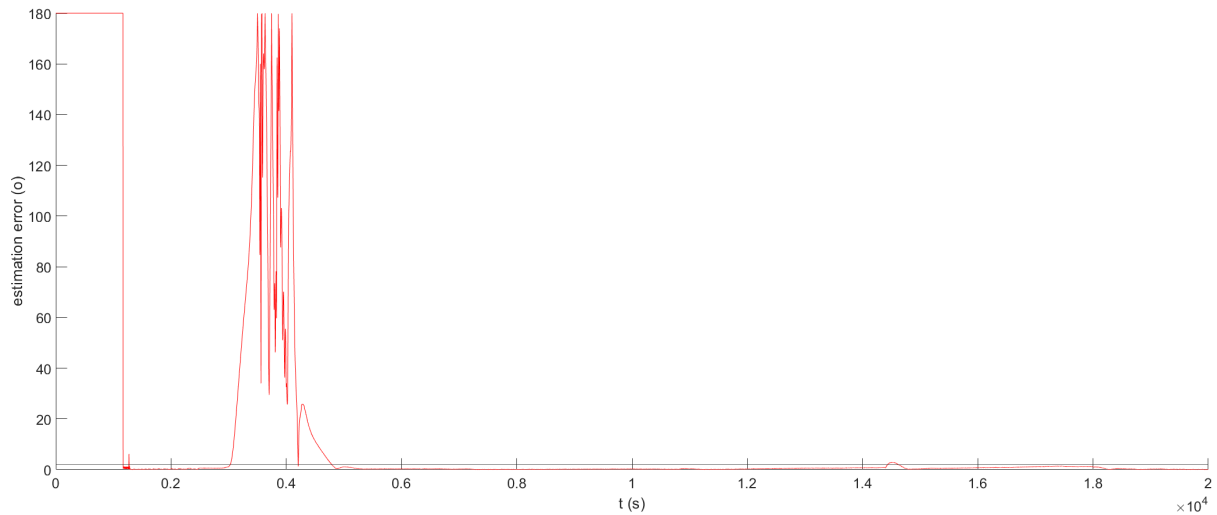
Figure 5.11: Estimation error in the event of magnetometer failure in nominal mission phase

Since the present sun sensor does not provide redundancy in case of magnetometer failure and its performance is not significantly better than the architecture with only magnetometers, this second option would be preferable due to the reduced mass and volume.

On the other hand, the nadir sensor could be a preferable option as the redundancy provide by this sensor reduces the risk of mission failure.

5.4.2   Cubewheel Alternative

In this subsection the Cubewheel momentum wheel is compared with a possible alternative flywheel. The RW210 (Version 1) flywheel by Hyperion Technologies [59] is studied as a possible lower mass, mass and power alternative. Details regarding this flywheel as well as more detailed results can be found in appendix C.

Table 5.4 compares the two solutions in terms of mass, power consumption, volume, momentum storage, as well as in terms of average pointing and estimation error.

Table 5.4: Different flywheels comparison [59, 86]

Flywheel	Mass	Volume	Momentum storage	Mean power consumption	Mean estimation error	Mean pointing error
Cubewheel	$60g$	$28mm \times 28mm \times 26.2mm$	$1.77mNms$	$0.36W$	0.45^o	3.76^o
RW210	$21g$	$25mm \times 25mm \times 15mm$	$1.5mNms$	$0.47W$	0.57^o	5.1^o

It can be seen that the average power consumption is larger in the RW210 flywheel architecture than the Cubewheel option, in the first case. This occurs mostly due to the fact that the nominal power consumption of the RW210 is higher, however, the power consumption of the magnetometers, mainly during detumbling, is also impacted by the gyroscopic stiffness achieved.

74
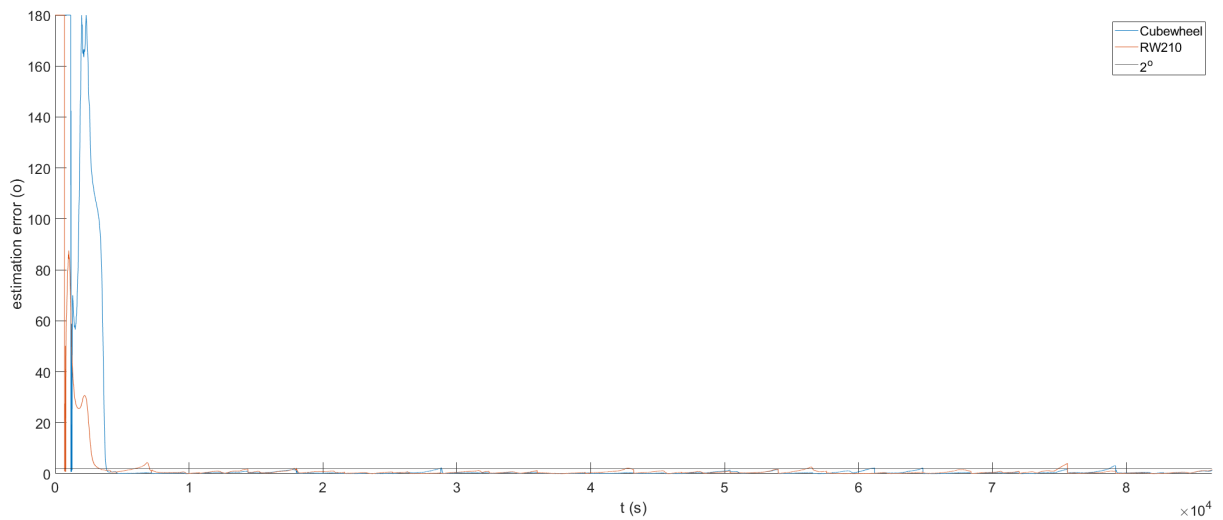
Figure 5.12: Pointing error for different flywheels
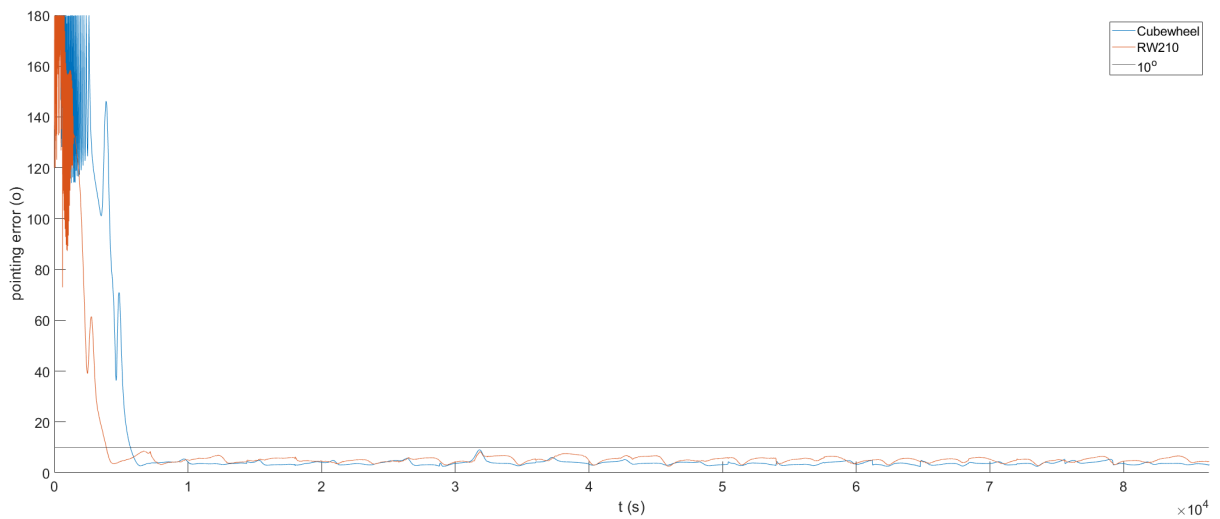
Figure 5.13: Estimation error for different flywheels

Nevertheless, as seen in figures 5.12 and 5.13 the smaller flywheel is enough to mostly maintain pointing and estimation requirements with substantial mass and volume savings. The smaller flywheel also allows for a faster detumble as the lower momentum storage and associated lower gyroscopic stiffness facilitates the detumbling of the spacecraft. More detailed graphics can be found in appendix C.

Chapter 6

Conclusions

The present research had two main goals: the development of a conceptual design framework tool capable of simulating several different ADCS architectures and using this tool, analyzing ORCASats current ADCS solution and compare it with possible alternative architectures.

Regarding the first objective, a simulator created in the past by [46] and [20] with the objective to simulate the specific ORCASat architecture was used as the base for this tool. The work developed on this thesis completed the simulator allowing it to simulate alternative architectures. This thesis contributed to the simulator with the following models:

- Third body perturbations;

- Deployable gravity gradient booms;

- Deployable aerodynamic panels;

- Hysteresis rods and permanent magnets;

- Earth sensor;

- Star tracker;

- AEKF for star track measurements;

- QUEST and Q-method algorithm;

- Reaction wheel clusters of up to 3 orthogonal wheels and associated motor control;

- Multiple (4) cluster configurations of CMGs, associated motor control and steering laws;

- A CMG feedback controller;

- Power analysis for spacecraft with body mounted and/or deployable solar panels.

Regarding the second objectives, an initial study on how the simulation initial conditions affect the results of the simulation was performed so as to better chose the simulation base environment. On a second instance, the performance of the ADCS in event of sensor/actuator failure was studied. It

76

has been found that a sun sensor failure does not strongly impact the mission requirements whereas a magnetometer failure would be fatal.

Based on this result, alternative solutions to the current architecture where studied. It has been shown that the presence of the sun sensor does not significantly impact both pointing and estimation accuracy. Moreover, it has been shown that, in spite of not being as accurate, the Cubesense nadir sensor provides redundancy in case of failure of the magnetometer in nominal mission phase, while having the same mass and volume of the Cubesense sun sensor.

Finally a lower mass, lower volume flywheel (RW210 by Hyperion Technologies) was tested as an alternative to Cubewheel. It was shown that even though the pointing and estimation accuracy are not strongly impacted by this alteration, the total average power consumption increases.

6.1   Future Work

The current developed tool is already capable of modeling with detail multiple models, however, the current star tracker model could use some improvement in order to account for the internal processes of the sensor. Moreover, the estimator and controller block could be equipped with extra alternative algorithms.

Finally, it would be interesting to adapt and complete the current design tool with a Hardware-In-the-Loop (HIL) test bed for the ADCS hardware. This step was initially a objective of this thesis, however since the available ORCASat's ADCS solution is going to be on board of the spacecraft, the impossibility of working with it limited this process.

Bibliography

[1] C. S. Agency.

[2] H. Heidt, J. Puig-Suari, A. Moore, S. Nakasuka, and R. Twiggs. Cubesat: A new generation of picosatellite for education and industry low-cost space experimentation. *SSC00-V-5 Experimentation*.

[3] H. C. Polat, J. Virgili-Llop, and M. Romano. Survey, statistical analysis and classifica-tion of launched cubesat missions with emphasis on the attitude control method. *JoSS*, 5(3):513–530, 2016. URL `www.jossonline.com`.

[4] E. Kulu. Nanosats database. `https://www.nanosats.eu/`.

[5] ORCASat.

[6] H. Robotics. Microsat cmg attitude control array.

[7] R. Miyagusuku, K. R. Arias, and E. R. Villota. Hybrid magnetic attitude control system under CubeSat standards. *IEEE Aerospace Conference Proceedings*, 2012.

[8] E. E. O. P. (eoPortal). `https://directory.eoportal.org/web/eoportal/satellite-missions/s/swampsat`, 2020. Accessed Apr 2021.

[9] V. Nagabhushan. *Development of control moment gyroscopes for attitude control of small satellites*. PhD thesis, University of Florida, 2009.

[10] F. L. Markley and J. L. Crassidis. *Fundamentals of spacecraft attitude determination and control*. Springer, 2014.

[11] B. Wie. *Space vehicle dynamics and control*. Aiaa, 1998.

[12] H. Schaub. Attitude dynamics fundamentals. *Encyclopedia of Aerospace Engineering*, 2010.

[13] D. Rondão. Modeling and simulation of the ecosat-iii attitude determination and control system. Master's thesis, Instituto Superior Técnico, 2016.

[14] F. A. Leve, B. J. Hamilton, and M. A. Peck. *Spacecraft momentum control systems*, volume 1010. Springer, 2015.

[15] I. A. Courie, Y. I. Jenie, and R. E. Poetro. Simulation of satellite attitude control using Single Gimbal Control Moment Gyro (SGCMG) system. *Journal of Physics: Conference Series*, 1130(1), 2018. ISSN 17426596. doi: 10.1088/1742-6596/1130/1/012003.

[16] A. N. Pechev. Feedback-based steering law for control moment gyros. *Journal of Guidance, Control, and Dynamics*, 30(3):848–855, 2007. ISSN 15333884. doi: 10.2514/1.27351.

[17] M. B. Salleh and N. M. Suhadis. Three-axis attitude control performance of a small satellite using control moment gyroscope. *Applied Mechanics and Materials*, 629:286–290, 2014. ISSN 16627482. doi: 10.4028/www.scientific.net/AMM.629.286.

[18] A. Gaude and V. Lappas. Design and structural analysis of a control moment gyroscope (CMG) actuator for cubesats. *Aerospace*, 7(5), 2020. ISSN 22264310. doi: 10.3390/AEROSPACE7050055.

[19] P. C. Hughes. *Spacecraft attitude dynamics*. Courier Corporation, 2012.

[20] B. Sabino. Attitude determination and control system of the orcasat. Master's thesis, Instituto Superior Técnico, 2020.

[21] D. Oltrogge and K. Leveque. An evaluation of cubesat orbital decay. In *Small Satellite Conference*, 2011.

[22] H. Schaub and J. L. Junkins. *Analytical mechanics of space systems*. Aiaa, 2003.

[23] D. T. Gerhardt and S. E. Palo. Passive Magnetic Attitude Control for CubeSat Spacecraft. *Small Satellite Conference*, page 10, 2010. URL `http://ons.usu.edu/cgi/viewcontent.cgi?article=1230&context=smallsat`.

[24] S. Chikazumi. Physics of ferromagnetism (second edit), 1997.

[25] F. Santoni and M. Zelli. Passive magnetic attitude stabilization of the UNISAT-4 microsatellite. *Acta Astronautica*, 65(5-6):792–803, 2009. ISSN 00945765. doi: 10.1016/j.actaastro.2009.03.012.

[26] M. L. Gargasz and N. A. Titus. Spacecraft attitude control using aerodynamic torques. *Advances in the Astronautical Sciences*, 127 PART 2:1179–1197, 2007. ISSN 00653438.

[27] J. Armstrong, C. Casey, G. Creamer, and G. Dutchover. Pointing control for low altitude triple cubesat space darts. In *Small Satellite Conference*, 2009.

[28] S. Arnold, J. Armstrong, C. Person, and M. Tietz. Qbx-the cubesat experiment. In *Small Satellite Conference*, 2012.

[29] U. Viterbi. Ready for launch: Students deliver usc's third cubesat satellite. `https://viterbischool.usc.edu/news/2019/03/ready-for-launch-students-deliver-uscs-third-cubesat-satellite/`, 2019. Accessed Apr 2021.

[30] ESA.

[31] P. Space, .

[32] NASA. `https://www.nasa.gov/smallsat-institute/sst-soa-2020/guidance-navigation-and-control`, 2021. Accessed Apr 2021.

[33] C. Space, .

[34] J. Tuthill. *Naval Postgraduate Thesis Design and Simulation of a Nano-Satellite Attitude Determination System*. PhD thesis, Naval Postgraduate School, 2009.

[35] B. O. Sunde. Sensor modelling and attitude determination for micro-satellite. Master's thesis, Norwegian University of Science and . . . , 2005.

[36] H. Schaub, S. R. Vadali, and J. L. Junkins. Feedback control law for variable speed control moment gyros. *Advances in the Astronautical Sciences*, 99(1):581–600, 1998. ISSN 00653438. doi: 10.1007/bf03546239.

[37] S. Song, H. Kim, and Y.-K. Chang. Design and implementation of 3u cubesat platform architecture. *International Journal of Aerospace Engineering*, 2018, 2018.

[38] V. Lappas. Practical results on the development of a control moment gyro based attitude control system for agile small satellites. In *Small Satellite Conference*, 2002.

[39] E. Bender. An Analysis of Stabilizing 3U CubeSats Using Gravity Gradient Techniques and a Low Power Reaction Wheel. (June):1–24, 2011.

[40] J. Peraire and J. Widnall. 3D Rigid Body Dynamics: The Inertia Tensor. *16.07 Dynamics - Massachusetts Institute of Technology*, page 13, 2008.

[41] A. Cambón Periscal. Study of feasibility of attitude control system for a 3u cubesat based on gravity-boom. B.S. thesis, Universitat Politècnica de Catalunya, 2020.

[42] N. J. Kasdin and D. A. Paley. *Engineering Dynamics*. Princeton University Press, 2011.

[43] J. Zorita. Dynamics of small satellites with gravity gradient attitude control. Master's thesis, KTH, School of Electrical Engineering (EES), Space and Plasma Physics, 2011.

[44] T. Flatley and D. A. Henretty. A magnetic Hysteresis Model. Small Satellite Conference, 2010.

[45] M. L. Psiaki. Aerodynamics and Active Magnetic Torquing. *Journal of Guidance, Control and Dynamics*, 27(3), 2004.

[46] Z. Pavanello. Simulation of a commercial off-the-shelf adcs with design of a pitch sun tracking attitude mode for the orcasat. Master's thesis, Università degli Studi di Padova, Instituto Superior Técnico, 2020.

[47] G. Giorgi. *Attitude Determination*, pages 781–809. Springer International Publishing, "2017".

[48] M. D. Shuster and S. D. Oh. Three-axis attitude determination from vector observations. *Journal of Guidance, Control, and Dynamics*, 4(1):70–77, 1981. ISSN 07315090. doi: 10.2514/3.19717.

[49] M. Ovchinnikov and D. Ivanov. Approach to study satellite attitude determination algorithms. *Acta Astronautica*, 98(1):133–137, 2014. ISSN 00945765. doi: 10.1016/j.actaastro.2014.01.024. URL `http://dx.doi.org/10.1016/j.actaastro.2014.01.024`.

[50] F. L. Markley. Multiplicative vs. additive filtering for spacecraft attitude determination. *Dynamics and Control of Systems and Structures in Space*, (467-474):48, 2004.

[51] K. Ogata. *Ingenieria de control moderna*. Pearson Educación, 2003.

[52] R. M. A.-M. Hummadi. Simulation of optimal speed control for a dc motor using linear quadratic regulator (lqr). *Journal of Engineering*, 18(3), 2012.

[53] D. S. Elliott, M. Peck, and I. A. Nesnas. Control momentum gyroscope steering law for box-90 array with performance guarantees. *AIAA Scitech 2020 Forum*, (January):1–28, 2020. doi: 10.2514/6.2020-1101.

[54] V. Lappas, P. Oosthuizen, P. Madle, P. Cowie, L, G. Yuksel, and D. Fertin. Design, analysis and in-orbit performance of the bilsat-1 microsatellite twin control moment gyroscope experimental cluster. In *55th International Astronautical Congress of the International Astronautical Federation, the International Academy of Astronautics, and the International Institute of Space Law*, pages A–4, 2004.

[55] N. S. Bedrossian, J. Paradise, E. V. Bergmann, and D. Rowell. Steering law design for redundant single-gimbal control moment gyroscopes. *Journal of Guidance, Control, and Dynamics*, 13(6): 1083–1089, Oct. 1990. doi:10.2514/3.20582.

[56] B. Wie, D. Bailey, and C. Heiberg. Singularity robust steering logic for redundant single-gimbal control moment gyros. *Journal of Guidance, Control, and Dynamics*, 24(5):865–872, 2001.

[57] B. Sabino. Attitude Determination and Control System of the Micro/Nano Satellite. Master's thesis, Instituto Superior Técnico, 2018.

[58] H. Okubo and S. Kuwamoto. Agile attitude control and vibration suppression of flexible spacecraft using control moment gyros. *IFAC Proceedings Volumes*, 46(19):417–422, 2013.

[59] Satsearch. Rw210 series reaction wheel. `https://satsearch.co/products/hyperion-technologies-rw210-series-reaction-wheel`. Accessed Oct 2021.

[60] N. S. Systems. Sun sensors. `https://www.newspacesystems.com/portfolio/sun-sensors/`, 2020. Accessed Aug 2021.

[61] *MAI Sun Sensor*. Maryland Aerospace, 2145 Priest Bridge Dr, Suite 15 Crofton, MD. 21114.

[62] S. MEMS. Products. `https://www.solar-mems.com/space-equipment/`, 2017. Accessed Aug 2021.

[63] C. Shop. Maus cubesat sunsensor. `https://www.cubesatshop.com/product/maus-cubesat-sunsensor/`, . Accessed Aug 2021.

[64] Sputnix. Sun sensor. `https://sputnix.ru/en/equipment/cubesat-devices/sun-sensor-flight-proof-1`. Accessed Aug 2021.

[65] Copernical. Bison64 sunsensors. `https://www.copernical.com/organisations/view-organisations-registry/itemlist/tag/SCOTS`. Accessed Aug 2021.

[66] GOMSpace. Fine sun sensor for high precision adcs control. `https://gomspace.com/shop/subsystems/attitude-orbit-control-systems/nanosense-fss-(1).aspx`, . Accessed Aug 2021.

[67] B. Space. Flight components. `https://www.bradford-space.com/flight-components`, . Accessed Aug 2021.

[68] A. Space. Sun sensors. `https://adcolespace.com/product-category/sun-sensors/`, . Accessed Aug 2021.

[69] N. S. Systems. Magnetometer. `https://www.newspacesystems.com/portfolio/magnetometer/`, 2020. Accessed Aug 2021.

[70] GOMSpace. Compact low noise magnetometer for high performance attitude determination systems. `https://gomspace.com/shop/subsystems/attitude-orbit-control-systems/nanosense-m315.aspx`, . Accessed Oct 2021.

[71] Honeywell. 3-axis magnetometer. `https://aerospace.honeywell.com/us/en/learn/products/sensors/3-axis-magnetometer`, 2021. Accessed Oct 2021.

[72] H. Technologies. High precision magnetometer. `https://hyperiontechnologies.nl/products/mm200/`, . Accessed Oct 2021.

[73] SatSearch. Satellite star trackers – the cutting edge celestial navigation products available on the global space marketplace. `https://blog.satsearch.co/2019-11-26-satellite-star-trackers-the-cutting-edge-celestial-navigation-products-available-on-the-global-space-marketplace`, 2019. Accessed Oct 2021.

[74] C. Shop. arcsec sagitta star tracker. `https://www.cubesatshop.com/product/kul-star-tracker/`, 2019. Accessed Oct 2021.

[75] A. Space. Star trackers/space cameras. `https://adcolespace.com/product-category/star-trackers-space-cameras/`, . Accessed Oct 2021.

[76] Cubespace. Cube ir. `https://www.cubespace.co.za/products/adcs-components/cube-ir/#cube-ir-specifications`. Accessed Oct 2021.

[77] C. Shop. Attitude sensors. `https://www.cubesatshop.com/product-category/attitude-sensors/`, 2019. Accessed Oct 2021.

[78] Meisei. Earth sensor for satellite. `https://www.meisei.co.jp/english/products/space/satellite-components/p1380`. Accessed Oct 2021.

[79] C. Shop. Attitude actuators. `https://www.cubesatshop.com/product-category/attitude-actuators/`, . Accessed Oct 2021.

[80] GOMSpace. 3-axis magnetorquer for 6u or larger nanosatellites. `https://gomspace.com/shop/subsystems/attitude-orbit-control-systems/nanotorque-gst-600.aspx`, . Accessed Oct 2021.

[81] I. Space. imtq magnetorquer board. `https://www.isispace.nl/product/isis-magnetorquer-board/`, . Accessed Oct 2021.

[82] Newspace. Magnetorquer rod. `https://www.newspacesystems.com/portfolio/magnetorquer-rod/`. Accessed Oct 2021.

[83] H. Technologies. Products. `https://hyperiontechnologies.nl/products/`, . Accessed Oct 2021.

[84] N. Avionics. Cubesat magnetorquer satbus mtq. `https://nanoavionics.com/cubesat-components/cubesat-magnetorquer-satbus-mtq/`, . Accessed Oct 2021.

[85] GomSpace. Reaction wheel for nanosatellites. `https://gomspace.com/shop/subsystems/attitude-orbit-control-systems/nanotorque-gsw-600.aspx`. Accessed Oct 2021.

[86] CubeSpace. Cubewheel. `https://www.cubespace.co.za/products/adcs-components/cubewheel/`. Accessed Oct 2021.

[87] N. Avionics. Cubesat reaction wheels control system satbus 4rw0. `https://nanoavionics.com/cubesat-components/cubesat-reaction-wheels-control-system-satbus-4rw/`, . Accessed Oct 2021.

[88] S. Flagg, T. Bleier, C. Dunson, J. Doering, L. DeMartini, P. Clarke, L. Franklin, J. Seelbach, J. Flagg, M. Klenk, V. Safradin, C. A. Suite, J. Cutler, A. Lorenz, and E. Tapio. Using Nanosats as a Proof of Concept for Space Science Missions: QuakeSat as an Operational Example. *18th Annual AIAA/USU Conference on Small Satellites*, 2004.

[89] B. S. Gregory. *Attitude control system design for ion, the illinois observing nanosatellite*. PhD thesis, University of Illinois at Urbana-Champaign, 2004.

[90] ION.

[91] F. Hennepe, B. Zandbergen, and R. Hamann. Simulation of the attitude behaviour and available power profile of the delfi-c3 spacecraft with application of the opsim platform. In *1st CEAS European Air and Space Conference*, 2007.

[92] E. Kahr, O. Montenbruck, K. O'Keefe, S. Skone, J. Urbanek, L. Bradbury, and P. Fenton. Gps tracking on a nanosatellite the canx-2 flight experience. In *8th international ESA conference on guidance, navigation & control systems. Karlovy Vary, Czech Republic*, pages 5–10, 2011.

[93] J. Reijneveld and D. Choukroun. Attitude control system of the delfi-n3xt satellite. *Progress in Flight Dynamics, Guidance, Navigation, Control, Fault Detection, and Avionics*, 6:189–208, 2013.

[94] N. E. Cornejo, R. Amini, and G. Gaydadjiev. Model-based fault detection for the delfi-n3xt attitude determination system. In *2010 IEEE Aerospace Conference*, pages 1–8, 2010. doi: 10.1109/ AERO.2010.5446801.

[95] M. Tassano, P. Monzon, and J. Pechiar. Attitude determination and control system of the uruguayan cubesat, antelsat. In *2013 16th International Conference on Advanced Robotics (ICAR)*, pages 1–6, 2013. doi: 10.1109/ICAR.2013.6766523.

[96] M. Tassano, P. Monzon, J. Ramos, G. De Martino, and J. Pechiar. An inexpensive attitude determination system for the uruguayan cubesat, antelsat. In *2014 IEEE International Instrumentation and Measurement Technology Conference (I2MTC) Proceedings*, pages 723–727, 2014. doi: 10.1109/I2MTC.2014.6860837.

[97] A. Mehrparvar. Attitude estimation for a gravity gradient momentum biased nanosatellite. *Digital-Commons@CalPoly*, 2013.

[98] R. J. Sellers. A gravity gradient, momentum-biased attitude control system for a cubesat. *Digital-Commons@CalPoly*, 2013.

[99] J. P. Mason, M. Baumgart, B. Rogler, C. Downs, M. Williams, T. N. Woods, S. Palo, P. C. Chamberlin, S. Solomon, A. Jones, et al. Minxss-1 cubesat on-orbit pointing and power performance: the first flight of the blue canyon technologies xact 3-axis attitude determination and control system. *arXiv preprint arXiv:1706.06967*, 2017.

[100] N. Jovanovic. Aalto-2 satellite attitude control system. Master's thesis, Aalto University. School of Electrical Engineering, 2014. URL `http://urn.fi/URN:NBN:fi:aalto-201409012592`.

[101] A. Kestilä, T. Tikka, P. Peitso, J. Rantanen, A. Näsilä, K. Nordling, H. Saari, R. Vainio, P. Janhunen, J. Praks, et al. Aalto-1 nanosatellite–technical description and mission objectives. *Geoscientific Instrumentation, Methods and Data Systems*, 2(1):121–130, 2013.

[102] T. Tikka, O. Khurshid, N. Jovanovic, H. Leppinen, A. Kestilä, and J. Praks. Aalto-1 nanosatellite attitude determination and control system end-to-end testing. In *Proceedings of the 6th European CubeSat Symposium*, 10 2014.

[103] C. Underwood, A. Viquerat, B. Taylor, C. Massimiani, R. Duke, S. Fellowes, M. Schenk, B. Stewart, C. Bridges, D. Masutti, et al. The inflatesail cubesat mission–the first european demonstration of drag-sail de-orbiting. *AAS Advances in the Astronautical Sciences Series*, 163, 2018.

[104] F. Hinckley. Simulation of the polarcube attitude control and determination subsystem, 2016.

[105] S. Jarmak, J. Brisset, J. Colwell, A. Dove, D. Maukonen, S. A. Rawashdeh, J. Blum, and L. Roe. Cubesat particle aggregation collision experiment (q-pace): Design of a 3u cubesat mission to investigate planetesimal formation. *Acta Astronautica*, 155:131–142, 2019. ISSN 0094-5765. doi: https://doi.org/10.1016/j.actaastro.2018.11.029.

[106] A. Wailand. *Development of a Computer Simulation Tool to Study the Attitude Determination and Control of CubeSats*. PhD thesis, 2020.

[107] M. H. Bhat, P. A. Bhat, D. R. Gulur, and R. Nanda. Operation of onboard data handling system in different switching modes for rvsat-1. In *2018 4th International Conference for Convergence in Technology (I2CT)*, pages 1–4, 2018.

[108] K. M. Hegde, A. C.R., A. K., and P. Kashyap. Design and development of rvsat-1, a student nano-satellite with biological payload. In *2019 IEEE Aerospace Conference*, pages 1–14, 2019.

[109] V. Lappas, N. Adeli, L. Visagie, J. Fernandez, T. Theodorou, W. Steyn, and M. Perren. Cubesail: A low cost cubesat based solar sail demonstration mission. *Advances in Space Research*, 48(11): 1890–1901, 2011. ISSN 0273-1177. doi: https://doi.org/10.1016/j.asr.2011.05.033.

[110] Y. Duann, L. C. Chang, C.-K. Chao, Y.-C. Chiu, R. Tsai-Lin, T.-Y. Tai, W.-H. Luo, C.-T. Liao, H.-T. Liu, C.-J. Chung, et al. Ideassat: A 3u cubesat mission for ionospheric science. *Advances in Space Research*, 66(1):116–134, 2020.

[111] U. Lee, T. Reynolds, B. Barzgaran, M. H. d. Badyn, J. Chrisope, A. Adler, K. Kaycee, and M. Mesbahi. Development of attitude determination and control subsystem for 3u cubesat with electric propulsion. In *AIAA SPACE and Astronautics Forum and Exposition*, page 5320, 2017.

[112] T. Kukowski. *Magnetic Attitude Control Development and Simulation for a 3U Cube Satellite*. PhD thesis, University of Minnesota, 2020.

[113] J.-H. Huang, T.-Y. Lin, C.-M. Liu, and J.-C. Juang. Design and evaluation of the attitude control system of the phoenix cubesat. In *2013 CACS International Automatic Control Conference (CACS)*, pages 47–51. IEEE, 2013.

[114] N. Shterev. Design and testing of the star trackers for the seam nanosatellite. Master's thesis, Luleå University of Technology, 2015.

[115] Y. Prevereaud, F. Sourgen, D. Mimoun, A. Gaboriaud, J. Verant, and J. Moschetta. Predicting the atmospheric re-entry of space debris through the qb50 entrysat mission. In *6th European Conference on Space Debris, Darmstadt, Germany*, pages 22–25, 2013.

[116] J. R. Cordova Alarcon, N. Örger, S. Kim, L. Soon, and M. Cho. Aoba velox-iv attitude and orbit control system design for a leo mission applicable to a future lunar mission. In *67th International Astronautical Congress (IAC), Guadalajara, Mexico*, 09 2016.

[117] J. W. Conklin, S. Nydam, T. Ritz, N. Barnwell, P. Serra, J. Hanson, A. N. Nguyen, C. Priscal, J. Stupl, B. Jaroux, et al. Preliminary results from the chomptt laser time-transfer mission. In *Small Satellite Conference*, 2019.

[118] M. K. Quadrino. *Testing the Attitude Determination and Control of a CubeSat with Hardware-in-the-Loop*. PhD thesis, Massachusetts Institute of Technology, 2014.

[119] J. P. Park, S. Y. Park, Y. B. Song, G. N. Kim, K. Lee, H. J. Oh, J. C. Yim, E. J. Lee, S. H. Hwang, S. W. Kim, et al. Cubesat development for canyval-x mission. In *14th International Conference on Space Operations, 2016*. American Institute of Aeronautics and Astronautics Inc, AIAA, 2016.

[120] J. Kolmas, P. Banazadeh, A. W. Koenig, B. Macintosh, and S. D'Amico. System design of a miniaturized distributed occulter/telescope for direct imaging of star vicinity. In *2016 IEEE Aerospace Conference*, pages 1–11. IEEE, 2016.

[121] K. Vega, D. Auslander, and D. Pankow. Design and modeling of an active attitude control system for cubesat class satellites. In *AIAA Modeling and Simulation Technologies Conference*, page 5812, 2009.

[122] J. P. Monteiro, R. M. Rocha, A. Silva, R. Afonso, and N. Ramos. Integration and verification approach of istsat-1 cubesat. *Aerospace*, 6(12):131, 2019.

[123] M. Chessab Mahdi. Attitude determination and control system design of kufasat. *International Journal of Current Engineering and Technology*, 4:2910–2920, 08 2014.

[124] J. M. Morrison, H. Jeffrey, H. Gorter, P. Anderson, C. Clark, A. Holmes, G. C. Feldman, and F. S. Patt. Seahawk: an advanced cubesat mission for sustained ocean colour monitoring. In *Sensors, Systems, and Next-Generation Satellites XX*, volume 10000, page 100001C. International Society for Optics and Photonics, 2016.

[125] M. Choi, J. Jang, S. Yu, O. Kim, H. Shim, C. Kee, et al. Single-axis hardware in the loop experiment verification of adcs for low earth orbit cube-satellite. *Journal of Positioning, Navigation, and Timing*, 6(4):195–203, 2017.

[126] W. H. Steyn and M.-A. Kearney. An attitude control system for za-aerosat subject to significant aerodynamic disturbances. *IFAC Proceedings Volumes*, 47(3):7929–7934, 2014.

[127] J. Guo and C. Han. Where is the limit: The analysis of cubesat adcs performance. In *4S Symposium 2016*, pages 1–15. European Space Agency and the Centre National d'Etudes Spatiales, 2016.

[128] L. Maciulis and V. Buzas. Lituanicasat-2: Design of the 3u in-orbit technology demonstration cubesat. *IEEE Aerospace and Electronic Systems Magazine*, 32(6):34–45, 2017.

[129] S. Rossi, A. Ivanov, G. Faure, M. Starein, R. Zufferey, and G. Burri. Cubeth adcs design, implementation and validation tests. In *66th International Astronautical Congress, IAC, Jaruselam, Israel*, 10 2015.

[130] J. S. Umansky-Castro, J. M. B. Mesquita, A. Kumar, M. Anderson, Y. T. Tan, J. J. Wen, V. H. Adams, M. A. Peck, A. Filo, D. Carabellese, et al. Design of the alpha cubesat: Technology demonstration of a chipsat-equipped retroreflective light sail. In *AIAA Scitech 2021 Forum*, page 1254, 2021.

[131] C. Kilic and A. R. Aslan. Mission analysis of a 2u cubesat, beeaglesat. In *2015 7th International Conference on Recent Advances in Space Technologies (RAST)*, pages 835–838. IEEE, 2015.

[132] S. Corpino and F. Stesina. Verification of a cubesat via hardware-in-the-loop simulation. *IEEE Transactions on Aerospace and Electronic Systems*, 50(4):2807–2818, 2014.

[133] A.-H. Jallad, P. Marpu, Z. Abdul Aziz, A. Al Marar, and M. Awad. Meznsat—a 3u cubesat for monitoring greenhouse gases using short wave infra-red spectrometry: Mission concept and analysis. *Aerospace*, 6(11):118, 2019.

[134] S. Deng, T. Meng, H. Wang, C. Du, and Z. Jin. Flexible attitude control design and on-orbit performance of the zdps-2 satellite. *Acta Astronautica*, 130:147–161, 2017.

[135] Y. Murata, Y. Sato, M. Sakal, T. Kuwahara, S. Fujita, Y. Kawasoe, R. Shinohara, and T. Izumiyama. Ground evaluation of the attitude control system of 3u-cubesat ihi-sat. In *2020 IEEE/SICE International Symposium on System Integration, SII 2020*, pages 771–776. Institute of Electrical and Electronics Engineers Inc., 2020.

[136] B. S. Cotten. *Design, analysis, implementation and testing of the thermal control, and attitude determination and control systems for the CanX-7 nanosatellite mission*. PhD thesis, University of Toronto, 2014.

[137] S.-A. Song, Y. Yoo, C.-G. Han, S. Koo, J. Suk, and S. Kim. System design of solar sail deployment and its effect on attitude dynamics for cube satellite cnusail-1. In *APISAT2014, 2014 Asia-Pacific International Symposium on Aerospace Technolog*, 09 2014.

[138] D. Gerhardt. Passive magnetic attitude control for cubesat spacecraft. In *Small Satellite Conference*, 2010.

[139] A. Romero Calvo, J. Biggs, and F. Topputo. Attitude control for the lumio cubesat in deep space. In *70th International Astronautical Congress (IAC 2019)*, pages 1–13, 2019.

[140] G. Minelli, C. Kitts, K. Ronzano, C. Beasley, R. Rasay, I. Mas, P. Williams, P. Mahacek, J. Shepard, J. Acain, et al. Extended life flight results from the genesat-1 biological microsatellite mission. In *Small Satellite Conference*, 2008.

[141] H. Ashida, K. Fujihashi, S. Inagawa, Y. Miura, K. Omagari, N. Miyashita, S. Matunaga, T. Toizumi, J. Kataoka, and N. Kawai. Design of tokyo tech nano-satellite cute-1.7+apd ii and its operation. *Acta Astronautica*, 66(9):1412–1424, 2010. ISSN 0094-5765. doi: https://doi.org/10.1016/j.actaastro.2009.10.035.

[142] R. Burton, S. Rock, J. Springmann, and J. Cutler. Online attitude determination of a passively magnetically stabilized spacecraft. *Acta Astronautica*, 133:269–281, 2017.

[143] G. Park, S. Seagraves, and H. McClamroch. A dynamic model of a passive magnetic attitude control system for the rax nanosatellite. In *AIAA Guidance, Navigation, and Control Conference*, page 8154, 2010.

[144] J. C. Springmann, A. J. Sloboda, A. T. Klesh, M. W. Bennett, and J. W. Cutler. The attitude determination system of the rax satellite. *Acta Astronautica*, 75:120–135, 2012.

[145] S. L. Crowley. A cubesat orbital test platform for an electrothermal plasma micro-thruster. *Digital-Commons@CalPoly*, 2019.

[146] T. Scholz, P. Rambaud, and C. Asma. Design of an aerodynamic stability and de-orbiting system for cubesats. In *2013 6th International Conference on Recent Advances in Space Technologies (RAST)*.

[147] H. Kayal, O. Balagurin, K. Djebko, G. Fellinger, F. Puppe, D. Seipel, S. Serdar, A. Schneider, T. Schwarz, and H. Wojtkowiak. Next level autonomous nanosatellite operations. In *2018 SpaceOps Conference*, page 2690, 2018.

[148] Faulhaber. Dc-gearmotors series 2619 ... sr. `https://www.faulhaber.com/en/products/series/2619sr/`. Accessed Oct 2021.

Appendix A

Cubesat's on board ADCS and COTS options

Table A.1: COTS CubeSat Sun sensors

Name	Temperature Range (℃)	FOV (°)	Sampling Rate (Hz)	Resolution (°)	Mass (g)	Volume (mmxmmxmm)	Input Voltage (V)	Power (mW)	Cost ($)	Company
NCSS-SA05 [60]	[-25;+50]	114	>10	<0.5	<5	33 x 11 x 6			3300	NewSpace
NFSS-411 [60]	[-25;+50]	140	5	<0.1	<35	34 x 32 x 20		37.5	12000	NewSpace
MAI KE [61]					3.5	27.94 x 17.14 x 2.03			5940	Maryland Aerospace
nanoSSOC-D60 [62]	[-30;+85]	120	50	0.5	6.2	43 x 14 x 5.9	3.3		4414	Solar MEMS
Nano-SSOC-A60 [62]	[-30;+85]	120		0.5	3.7	27.4 × 14 × 5.9	3.3		2697	Solar MEMS
SSOC-D60 2-Axis [62]	[-45;+85]	120		0.3	35.5	50 × 30 × 12	5		14958	Solar MEMS
SSOC-A60 2-Axis [62]	[-45;+85]	120		<0.3	25	30 × 30 × 12	5	36	8500	Solar MEMS
MAUS [63]		128		2					8827	Lens RD
SXC-SD-01 [64]	[-40;+85]	120	10	<0.5	10	28 x 23 x 11		15	3359	Sputnix Orbicraft-Pro
BiSon64 [65]	[-40;+85]	136		0.5	21.7					
NanoSense FSS [66]		120	100	0.5	3	22 x 11 x 5.5	3.3			GOMSPACE
Mini-FSS [67]	[-50;+80]	172		1.5	50	50 x 46 x 17				Bradford Space
AdcoleSpace SS [68]					3.5	27.94 x 17.14 x 2.03				Adcole Space

Table A.2: COTS CubeSat magnetometers

Name	Sample Rate (Hz)	Accuracy (nT)	Range (μT)	Noise (nT rms/Hz)	Mass (g)	Volume (mmxmmxmm)	Input Voltage (V)	Power (mW)	Company
NMRM- Bn25o485 [69]	18	±60	8	16	85	99 x 43 x 17	5	750	NewSpace
NMRM-001 -485 [69]	18	±60	8	8	67	96 x 45 x 20	5	550	NewSpace
NanoSense M315 [70]	140	±800	15	15	8	20 x 20 x 8	3.2 to 5	8.25	GomSpace
Honeywell HMC 5983 [71]	160-220	±1100	-	20	18	3 x 3 x 0.9	1.8 to 2.5	0.25	Honeywell
MM200 [72]	<500	±800	-	1.18	12	33 x 20 x 11.3	0.5 to 10		Hyperion

Table A.3: COTS CubeSat star trackers

Name	FOV(°)	Update rate (Hz)	Accuracy	Max tracking rate (°/s)	Power (W)	Mass (g)	Volume (mmxmmxmm)	Input voltage (V)	Cost (€)	Company
NST-3 [73]		10	5"/70"			165	50 x 50 x 50	5	30000	TY-Space
Sagitta [74]		10	10"		1	250	50 x 95 x 45	5	45000	ArcSec
CubeStar [73]	58 x 47	1	0.0154°	0.3	0.142	55	50 x 35 x 55	3.3	11593	CubeSpace
Adcole Space ST [75]		4	5.7"	>2.0	1.5	282	55 x 65 x 70	5		Adcole Space
Standard NST [73]	10 x 12		6.0"		1.5	350	100 x 55 x 50			Blue Canyon Technologies
Star-T3 [73]	20 x 20	5	<2.0"	0.3	1	350	60 x 60 x 100	5 to 12		Space Inventor
ST200 [73]		5	30"	>0.3	0.6	42	29 x 29 x 38.1	3.65		Hyperion Technologies

Table A.4: COTS CubeSat earth sensors

Name	FOV(°)	Accuracy(°)	Mass (g)	Volume (mmxmmxmm)	Input voltage (V)	Power (mW)	Cost ($)	Company
CubeIR [76]	120 x 90	<1.5	50	26 x 26 x 30	3.3	230	8,500	CubeSpace
MAI-SES [77]	60 x 60	0.25	33	43.3 x 31.8 x 31.8	3.3	132	14,9	MAI
Meisei Earth Sensor [78]	33 x 33	1.5	250	40 x 40 x 55	5	<1000	55,224	Meisei

Table A.5: COTS CubeSat magnetorquers

Name	Residual Moment (Am^2)	Magnetic Moment (Am^2)	Saturation (Am^2)	Mass (g)	Volume (mmxmmxmm)	Input voltage (V)	Power (mW)	Cost ($)	Company
NCTR-M002 [79]	<0.001	>0.2		<30	70 x 9 x 9	5	200	1200	NewSpace
NCTR-M012 [79]	<0.005	1.19		<50	94 x 15 x 13	5	<800		NewSpace
EXA MT01 [79]	<0.0045	<0.39	>0.85	7.5	50 x 4.3 x 3.2	1.25-7.5	250 to 1750	1194	EXA
NanoTorque GST-600 [80]	0.001	0.340		156	90.5 x 96.9 x 17.2				GomSpace
ISIS iMTQ [81]	0.01	0.2		196	95.9 x 90.1 x 17	5			ISIS
Cubetorquer [80]	0.00048		1.5	28					CubeSpace
NCTR-M016 [82]	<0.005	1.60		<53	107 x 15 x 13	5	<1200		NewSpace
MTQ200.20 [83]		0.2	1.0	39.6	10.7 x 10.7 x 80		90		Hyperion Technologies
MTQ200.10S [83]		0.1	0.25	44.8	19 x19 x 25		225		Hyperion Technologies
Satbus MTQ [84]		0.3		205		5			NanoAvionics

Table A.6: COTS CubeSat CMG

Name	Max Speed (rpm)	Torque (mNm)	Momentum (mNm-s)	Mass (g)	Volume (mmxmmxmm)	Power (W)	Company
Microsat CMG [6]	12000	112	56	600	48 x 48 x 91	1.5	HoneyBee Robotics

Table A.7: COTS CubeSat flywheels

Name	Max Speed (rpm)	Max Torque (mNm)	Accuracy (rpm)	Momentum Storage (mNms)	Mass (g)	Volume (mmxmmxmm)	Input voltage (V)	Max Power (mW)	Price (€)	Company
NanoTorque GSW-600 [85]	±6000	1.5	0.5	19	940	95.0 x 95.0 x 61.6	5	300		GomSpace
CubeWheel small [86]	±8000	0.23	±5	1.77	60	28 x 28 x 26.2	6.5 to 16	650	3978	CubeSpace
CubeWheel small+[86]	±6000	2.3	±5	3.6	90	33.4 x 46 x 31.5	6.5 to 16	2300	5036	CubeSpace
CubeWheel medium [86]	±6000	1.0	±2	10.82	150	46 x 46 x 31.5	6.5 to 16	2300	5797	CubeSpace
CubeWheel Large [86]	±6000	2.3	±2	30.61	225	57 x 57 x 31.5	6.5 to 16	4500	6643	CubeSpace
MAI-400 [79]	±10000	0.635		11.076	110	33 x 33 x 38.4	5		6010	MAI
RW210 Version 1 [59]	±10000	0.1	±0.5	1.5	21	25 x 25 x 15		<800		Hyperion
RW210 Version 2 [59]	±15000	0.1	±0.5	3	32	25 x 25 x 15		<800		Hyperion
RW210 Version 3 [59]	±15000	0.1	±0.5	6	48	25 x 25 x 15		<800		Hyperion
RW single [87]	±6500	3.2	1	20	137	44 x 44 x 24	5	3250		NanoAvionics

Name	Norad ID	Size	State	FS	CS	MM	G	ES	ST	RW	MW	CMG	MT	PM	HR	GGB	A	Source
ORCASat	——	2U	D	1	0	1	1	0	0	0	1	0	3	0	0	0	0	[5]
QuakeSat	27845	3U	I	0	12	0	0	0	0	0	0	0	0	4	2	0	0	[88]
ION	——	2U	LF	0	0	1	0	0	0	0	0	0	3	0	0	0	0	[89, 90]
Delfi-C3	32789	2U	O	2	0	0	0	0	0	0	0	0	0	1	4	0	0	[91]
CanX-2	32790	3U	I	0	6	1	0	0	0	0	1	0	3	0	0	0	0	[92]
Delfi-n3xt	39428	3U	O	0	8	2	3	0	0	3	0	0	3	0	0	0	0	[93, 94]
Antelsat	40034	2U	I	0	6	1	3	0	0	0	0	0	3	0	0	0	0	[95, 96]
Exocube	40380	3U	O	0	y	y	y	0	0	0	1	0	10	0	0	2	0	[97, 98]
MinXSS	41474	3U	R	1	0	1	1	0	1	3	0	0	3	0	0	0	0	[99]
Aalto-2	42729	2U	R	1	0	1	1	0	0	0	0	0	3	0	0	0	0	[100]
Aalto-1	42775	3U	O	6	0	1	1	0	1	3	0	0	3	0	0	0	0	[101, 102]
InflateSail	42770	3U	R	1	6	1	1	1	0	0	1	0	3	0	0	0	0	[103]
PolarCube	47310	3U	O	0	0	2	2	0	1	3	0	0	y	0	0	0	0	[104]
Q-Pace	99756	3U	O	0	0	0	0	0	0	0	0	0	0	1	2	0	0	[105]
LORIS	——	2U	D	0	18	1	1	0	0	3	0	0	3	0	0	0	0	[106]
RVSat-1	——	2U	D	0	y	1	0	0	0	0	0	0	3	0	0	0	0	[107, 108]
CubeSail	——	3U	C	1	0	1	1	1	0	0	0	0	3	0	0	0	0	[109]
IDEASSat	47458	3U	O	1	0	1	1	0	1	3	0	0	3	0	0	0	0	[110]
HuskySat 1	45119	3U	O	1	0	1	1	0	0	3	0	0	3	0	0	0	0	[111]
SOCRATES	39768	3U	O	0	0	y	y	0	0	0	0	0	y	0	0	0	0	[112]
Phoenix	42706	2U	R	1	6	1	1	0	0	0	1	0	3	0	0	0	0	[113]
SEAM	——	3U	LF	0	9	2	0	0	1	0	0	0	6	0	0	0	0	[114]
EntrySat	44429	2U	O	0	y	1	1	0	0	0	0	0	y	0	0	0	0	[115]
AobaVelox-IV	43940	2U	O	2	6	0	1	0	0	3	0	0	0	0	0	0	0	[116]
CHOMPTT	43855	3U	O	0	y	1	1	0	0	3	0	0	3	0	0	0	0	[117]
MicroMAS-1	——	3U	R	0	6	1	1	y	0	3	0	0	y	0	0	0	0	[118]
CANYVAL-X jerry	43136	1U	I	y	y	1	1	0	0	0	0	0	3	0	0	0	0	[119]
CANYVAL-X tom	43136	2U	I	0	1	1	1	0	0	3	0	0	3	0	0	0	0	[119]
mDOT	——	6U	D	0	2	0	0	0	2	4	0	0	3	0	0	0	0	[120]
CINEMA	——	3U	I	1	y	1	0	0	0	0	0	0	2	0	0	0	0	[121]
Istsat-1	——	1U	D	0	y	y	y	0	0	0	0	0	y	0	0	0	0	[122]
Kufasat	——	1U	D	0	6	1	3	0	0	0	0	0	3	0	0	0	0	[123]
Sea Hawk-1	43820	3U	O	2	y	y	y	0	0	3	0	0	3	0	0	0	0	[124]
Snuglite	43784	2U	O	0	y	1	1	0	0	0	0	0	3	0	0	0	0	[125]
KAUSAT-5	43135	3U	I	1	0	0	0	0	0	0	0	4	3	0	0	0	0	[37]
ZA-AeroSat	42713	3U	R	1	6	1	1	1	0	0	1	0	3	0	0	0	0	[126]
CubeSTAR	——	2U	C	y	5	1	2	0	0	0	0	0	3	0	0	0	0	[127]
LituanicaSAT-2	42768	3U	O	4	0	2	2	0	0	0	0	0	3	0	0	0	0	[128]
CubETH	——	1U	D	0	y	y	y	0	0	0	0	0	y	0	0	0	0	[129]
Alpha	——	1U	D	0	0	1	1	0	0	0	0	0	3	0	0	0	0	[130]
BeEagleSat	42736	2U	R	1	0	1	1	1	0	0	1	0	3	0	0	0	0	[131]
e-star-ii	41459	1U	O	0	y	1	1	0	0	0	0	0	3	0	0	0	0	[132]
MeZnSat	46489	3U	O	1	10	1	0	1	1	3	0	0	3	0	0	0	0	[133]
ZDPS-2-A	40901			1	5	1	1	1	0	4	1	0	1	0	0	0	0	[134]
IHI-Sat	——	3U	D	0	6	1	1	0	0	1	0	0	3	0	0	0	0	[135]
CanX-7	41788		O	0	0	1	0	0	0	0	0	0	3	0	0	0	0	[136]
CNUSail-1	43133	3U	I	1	0	1	1	0	0	3	0	0	1	0	0	0	0	[137]
CSSWE	38761	3U	O	0	0	1	0	0	0	0	0	0	0	1	4	0	0	[138]
LUMIO	——	12U	D	2	0	1	1	0	2	3	0	0	0	0	0	0	0	[139]
GeneSat-1	29655	3U	R	0	0	0	y	0	0	0	0	0	0	y	y	0	0	[140]
Firefly	39404	3U	R	0	0	0	0	0	0	0	0	0	0	0	0	y	0	[3]
Cute-1.7+APDII	32785	2U	O	0	y	y	y	0	0	0	0	0	y	0	0	0	0	[141]
RAX-1	37223	3U	I	0	0	0	0	0	0	0	0	0	0	y	y	0	0	[142, 143]
RAX-2	37853	3U	I	0	0	0	0	0	0	0	0	0	0	y	y	0	0	[144]
Exocube-2	47319	3U	I	0	y	y	y	0	0	0	1	0	y	0	0	y	0	[145]
QARMAN	45263	3U	R	0	0	0	0	0	0	0	0	0	0	0	0	0	y	[146]
SONATE	44400	3U	UK	0	12	2	2	0	2	3	0	0	6	0	0	0	0	[147]
SWAMPSAT 1	39402	1U	I	0	6	1	1	0	0	0	0	4	1	0	0	0	0	[8]
SWAMPSAT 2	45115	3U	O	0	0	0	0	0	0	0	0	4	0	0	0	0	0	[9]
QBX	——	3U	R	0	0	1	0	1	0	3	0	0	3	0	0	0	Y	[26, 28]

Appendix B

Momentum exchange devices

B.1 BLDC motor control

Table B.1: BLDC reaction wheel motor parameters

Parameter	Value	Unit
Excentricity white noise power	1×10^{-16}	Nm
K_i	3.93×10^{-3}	Nm/A
K_e	3.93×10^{-3}	Vs/rad
R	1.68	Ω
Voltage Saturation	3	V
L	9	μH
Current Saturation	0.88	A
Speed Saturation	754	rad/s
Inertia	1.9397×10^{-6}	kgm^2
Viscous friction coefficient	1.11×10^{-7}	Nms/rad
Coulomb friction coefficient	1.1×10^{-16}	Nm

All the values where based on the DC-Gearmotors Series 2619 S motor [148]. A rough estimation of a realistic inertia value was obtained based on the motor inertia without load and typical inertia values of Cubesat flywheels, namely, Hyperion's RW210 Version 1 [59].

B.2   CMG performance analysis parameters

Table B.2: BLDC gimbal motor parameters

Parameter	Value	Unit
Excentricity white noise power	1×10^{-16}	Nm
K_i	3.93×10^{-3}	Nm/A
K_e	3.93×10^{-3}	Vs/rad
R	1.68	Ω
Voltage Saturation	3	V
L	9	μH
Current Saturation	0.88	A
Speed Saturation	1	rad/s
Inertia	1.9397×10^{-6}	kgm^2
Viscous friction coefficient	1.11×10^{-7}	Nms/rad
Coulomb friction coefficient	1.1×10^{-16}	Nm

All the values where based on the CMG gimbal motor designed in [9]. Inertia values were roughly estimated based on the inertia of the spinning disk and the motor.

Table B.3: CMG flywheel parameters

Parameter	Value	Unit
Eccentricity white noise power	1×10^{-16}	Nm
K_i	6.57×10^{-4}	Nm/A
K_e	6.57×1010^{-4}	Vs/rad
R	19.4	Ω
Maximum momentum storage	0.0015	Nms
Maximum Torque	0.1	Nm
Maximum Speed	10000	rpm
Maximum Voltage	3.5	V
Moment of Inertia	1.43297×10^{-6}	kgm^2
Viscous friction coefficient	4.35×10^{-8}	Nms/rad
Coulomb friction coefficient	4.78×10^{-4}	Nm
Retroactive constant	869.3	Ω/s

The flywheel was modelled after the commercially available Hyperion's RW210 Version 1 flywheel [59] and followed the momentum wheel model developed in [46].

Table B.4: Steering law parameters

Parameter	Value
m_{cr}	4.6×10^{-10}
k_0	2×10^{-11}
k_{max}	3×10^{-10}
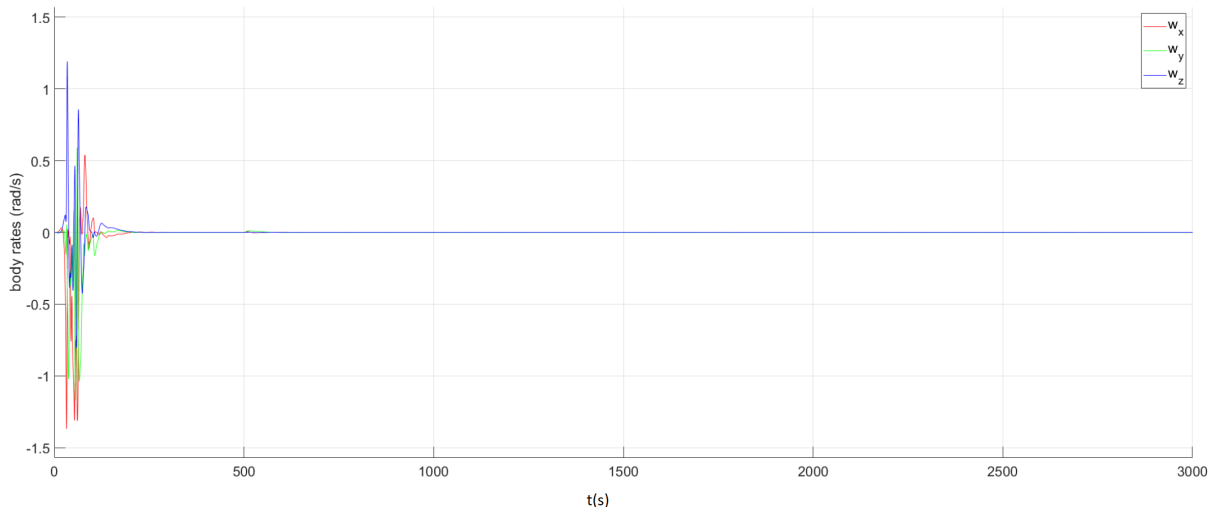
Figure B.1: Body rates
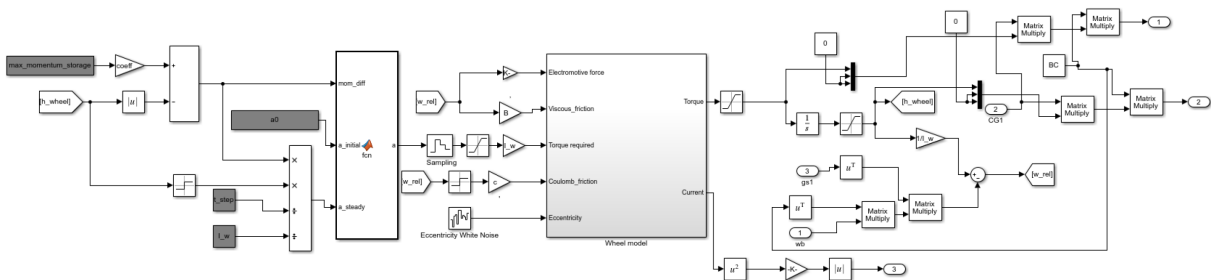
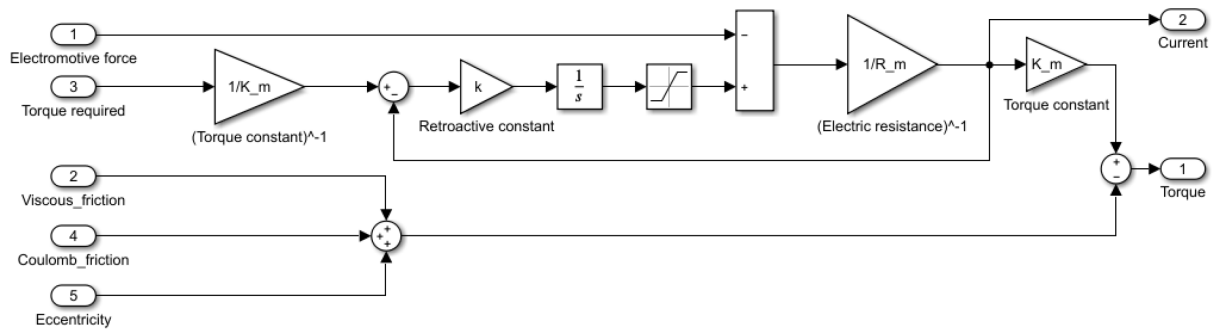Figure B.2: CMG flywheel model with motor driver and motor driver controller developed in [46]

Figure B.3: CMG flywheel motor model developed in [46]

Appendix C

Simulation results

C.1 Performance of ORCASat's ADCS with different conditions
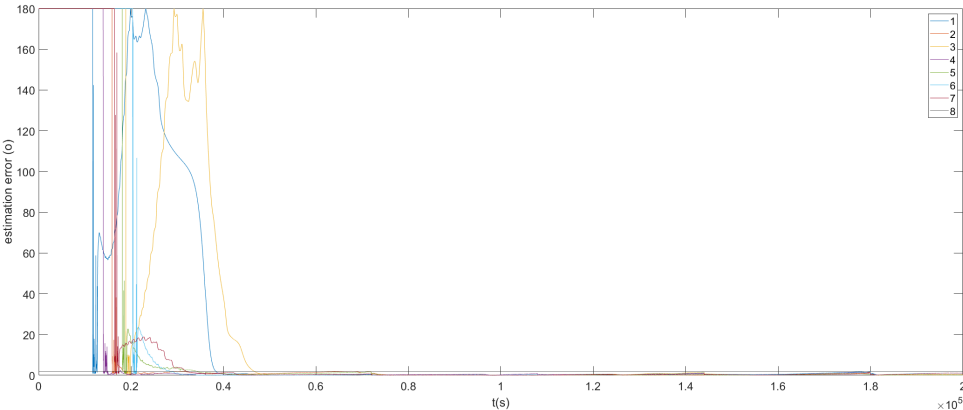
Figure C.1: Pointing error for different q_0
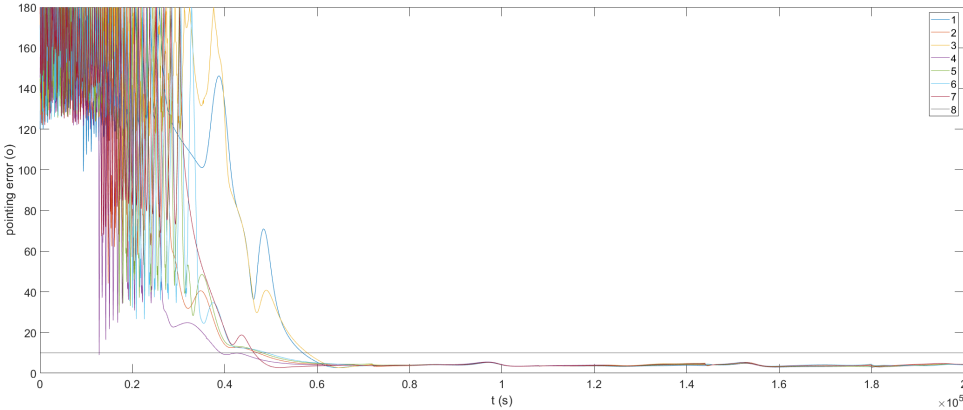
Figure C.2: Estimation error for different q_0
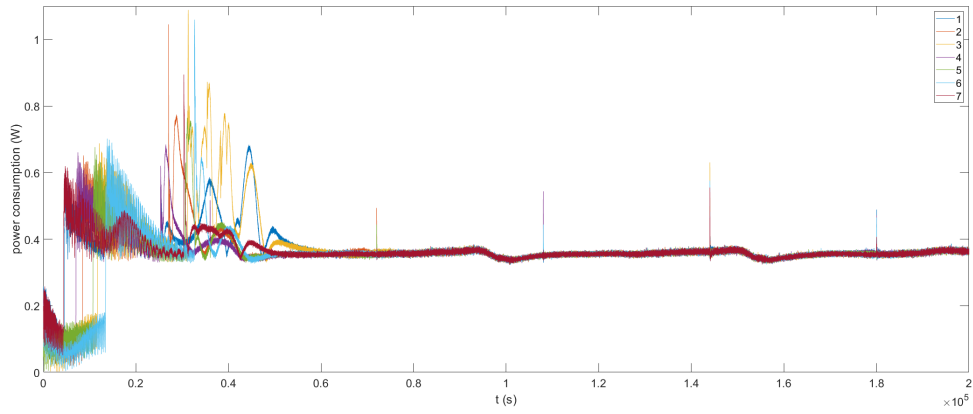
Figure C.3: Power consumption for different q_0
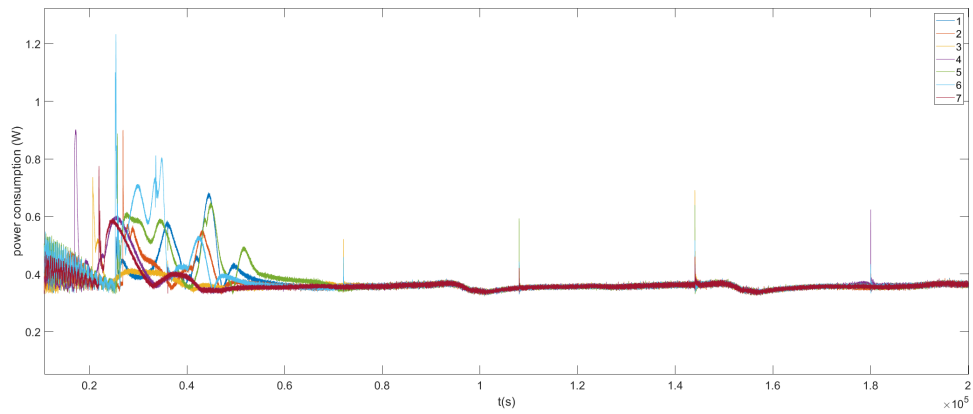
Figure C.4: Power consumption for different initial body rates

C.2 Performance of different architectures: sensors
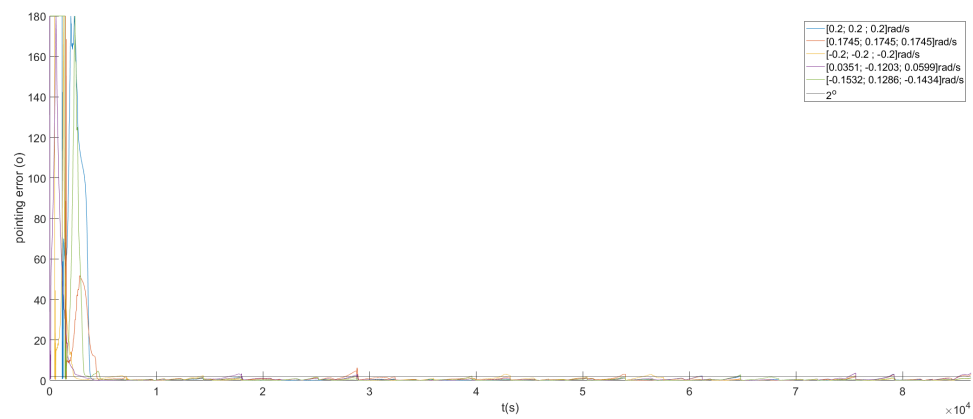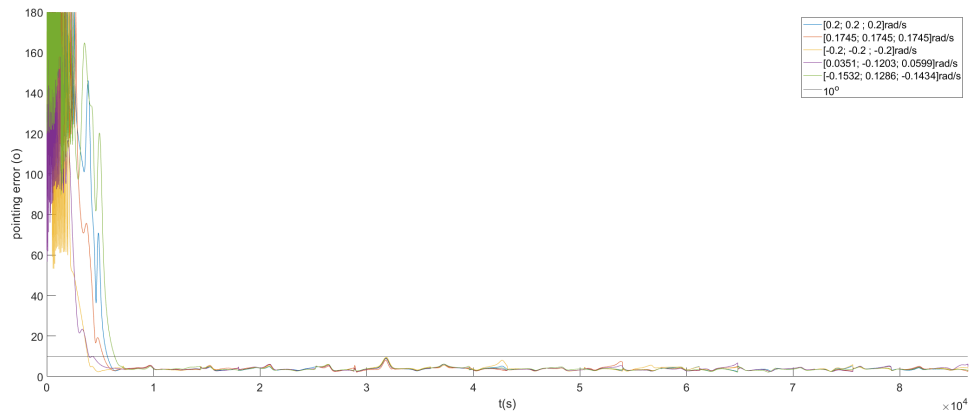

Figure C.5: Estimation error for different initial body rates: ORCASat architecture

Figure C.6: Pointing error for different initial body rates: ORCASat architecture
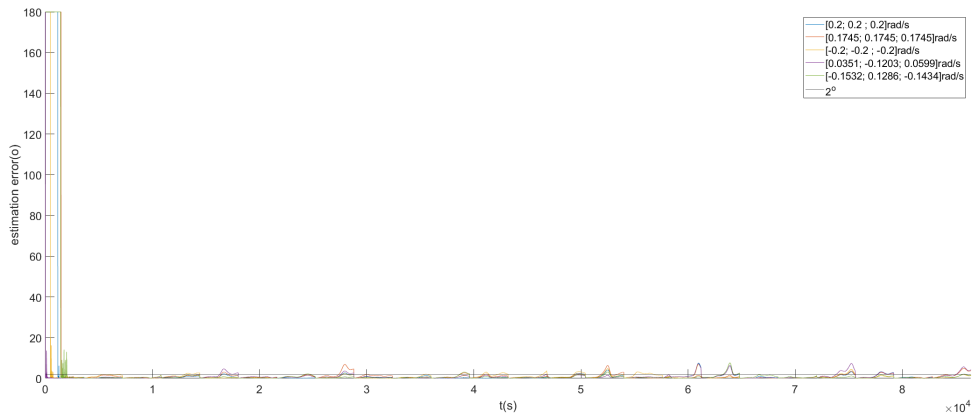
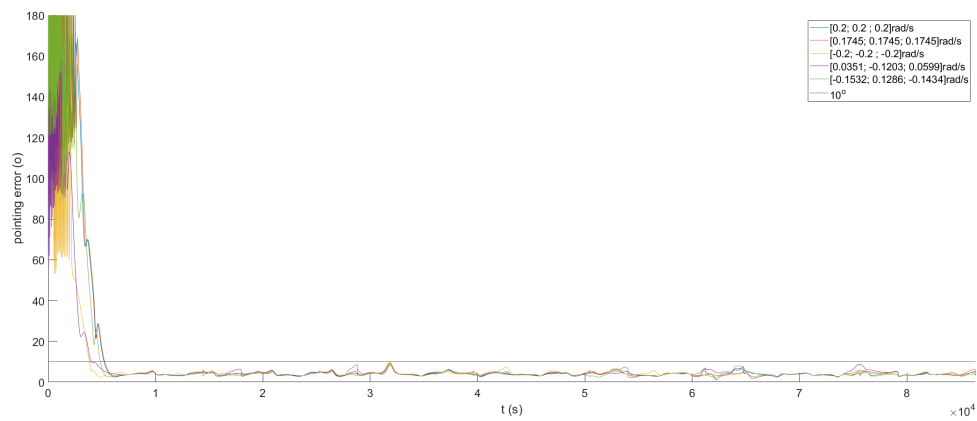Figure C.7: Estimation error for different initial body rates: Earth Sensor+magnetometer architecture

Figure C.8: Pointing error for different initial body rates: Earth Sensor+magnetometer architecture
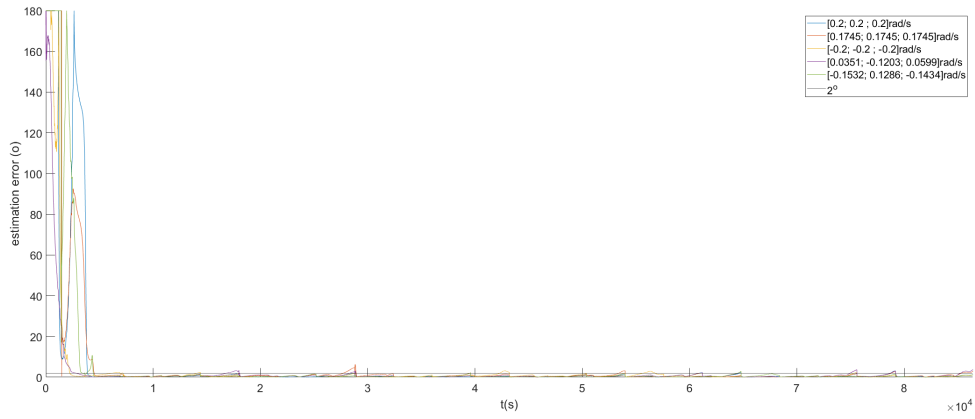
Figure C.9: Estimation error for different initial body rates: just magnetometer architecture
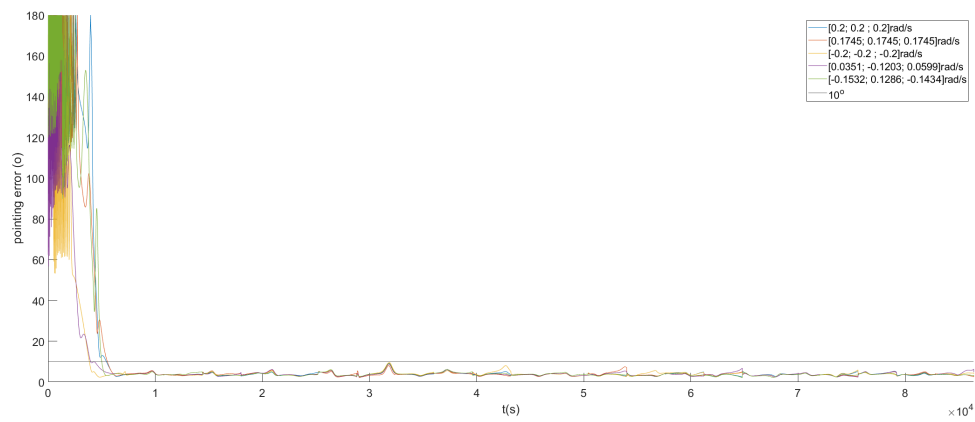

Figure C.10: Pointing error for different initial body rates: just magnetometer architecture
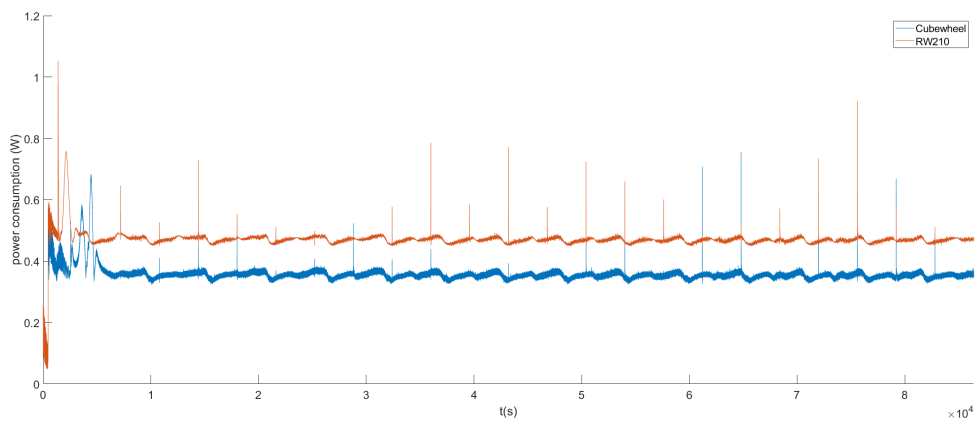
C.3   Performance of different flywheels

Figure C.11: Power consumption different momentum wheels